Geometry-based Beam Orientation Optimization for Intensity Modulated Radiation Therapy

BY

Peter Potrebko

A Thesis/Practicum submitted to the Faculty of Graduate Studies of The University of Manitoba in partial fulfillment of the requirement of the degree

DOCTOR OF PHILOSOPHY

Geometry-based Beam Orientation Optimization for Intensity Modulated Radiation Therapy

by

Peter Potrebko

A Thesis submitted to the Faculty of Graduate Studies of

The University of Manitoba

in partial fulfilment of the requirements of the degree of

DOCTOR OF PHILOSOPHY

Department of Physics and Astronomy

University of Manitoba

Winnipeg

Abstract

The selection of optimal beam orientations is a fundamental problem for intensity-modulated radiation therapy (IMRT). The treatment planner manually selects beam orientations based on experience and intuition, which can involve a time-consuming trial-and-error approach, or employs equiangular-spaced beams which are usually not optimal. The clinical use of dose-based beam orientation optimization (BOO) algorithms has been precluded by long optimization times (several hours) arising from the calculation of dose distributions for a large number of possible solutions. The objective of this thesis, separated into four fundamental investigations, is to develop and demonstrate several fast, geometry-based (instead of dose-based) BOO methods for IMRT which produce improved dose distributions in a clinically realistic time frame. First, an exhaustive treatment planning study of coplanar equiangular beam space is performed on a cohort of prostate IMRT patients to investigate the variation of the dose distribution with beam orientation. Second, a strong correlation between the beam intersection volume (BIV) and the subsequent IMRT dose distribution is theoretically derived and then observed on the prostate patient cohort. Third, a simulated annealing BOO algorithm generalizes the BIV concept to include the optimization of multiple BIV components within a critical structure. The optimized beam orientations produce improved IMRT dose distributions compared to standard plans using 5, 7, and 9 equiangular-spaced beams for a variety of treatment sites. In the gastric case, the V 20 Gy of the right kidney is reduced by 41.1%, 32.1%, and 29.5%. In the prostate case, rectal sparing is improved over all standard plans. In the Stage-IV oropharyngeal case, the

contralateral parotid V 30 Gy and mean dose are substantially reduced by: 11.2%, 11.2%, 10.8% and 7.8 Gy, 7.9 Gy, 8.0 Gy. Finally, the anatomic-BOO (A-BOO) algorithm for IMRT is developed which vectorially analyzes patient anatomy and produces optimal beam orientations based on (1) tangential orientation bisecting the target and adjacent critical structures to produce precipitous dose gradients between them and (2) geometric target conformity. Optimal beam orientations identified by the A-BOO and BIV algorithms produce similar substantial improvements in critical structure sparing. In conclusion, this thesis demonstrates the usefulness of fast, geometry-based BOO for IMRT.

Acknowledgements

I would like to take this opportunity to express my gratitude to the many people who have supported and encouraged me during this journey. I would like to thank my supervisor and mentor, Dr. Boyd McCurdy. Boyd is an outstanding scientific researcher, medical physicist, and teacher. From the beginning of my Ph.D., he has provided me with extremely valuable insight and it has been a pleasure to work with him. I look forward to our continued collaboration and expanding this department's research to become the leader in Canada. I would like to thank my advisory committee for their advice throughout my Ph.D. The members include Dr. John Lewis, Dr. Gerald Gwinner, and Dr. Gabriel Thomas. I am grateful to Dr. Stephen Pistorius for establishing an excellent graduate program in Medical Physics at the University of Manitoba. I thank Stephen for his commitment to ensure that this graduate program is of the highest quality. I would like to thank Dr. James Butler, Dr. Adel El-Gubtan, and Dr. Zoann Nugent for their assistance during manuscript preparation. I would also like to thank my friends and colleagues Niranjan Venugopal, Jorge Alpuche, Eric Van Uytven, Krista Chytyk, Jenna King, Dr. Jeff Bews, Dr. Anita Berndt, Dr. Daniel Rickey, Dr. Muoi Tran, James Beck, Kyle Malkoske, Charles Schroeder, Keith Nakonechny, Tara Bailey and Tammy Bridgelall. I would like to gratefully acknowledge financial support during my Ph.D. provided by the Natural Sciences and Engineering Research Council, CancerCare Manitoba, the University of Manitoba, and the Manitoba Health Research Council. Finally, I would like to express my deepest gratitude to my wonderful family for always uplifting my spirit with their incredible encouragement.

To My Father

Table of Contents

List of Tables

List of Figures

List of Abbreviations

3D-CRT	Three-dimensional Conformal Radiation Therapy
A-BOO	Anatomic Beam Orientation Optimization
BAO	Beam Angle Optimization
BEV	Beam's-Eye-View
BEVD	Beam's-Eye-View Dosimetrics
BIV	Beam Intersection Volume
BOO	Beam Orientation Optimization
CI	Conformity Index
CT	Computed Tomography
CTV	Clinical Target Volume
DAO	Direct Aperture Optimization
DMPO	Direct Machine Parameter Optimization
DNA	Deoxyribonucleic Acid
DRR	Digitally Reconstructed Radiograph
DVH	Dose-Volume Histogram
EBR	External-beam Radiotherapy
EUD	Equivalent Uniform Dose
FBP	Filtered Back-projection
GA	Genetic Algorithm
GTV	Gross Tumour Volume
ICRU	International Commission on Radiation Units and Measurements

IMAT	Intensity-modulated Arc Therapy
IMRT	Intensity-modulated Radiation Therapy
MC	Monte Carlo
MLC	Multi-leaf Collimator
MRI	Magnetic Resonance Imaging
MSKCC	Memorial Sloan-Kettering Cancer Center
OAR	Organ-at-Risk
OF	Objective Function
PTA	Planning Target Area
PTV	Planning Target Volume
ROI	Region-of-Interest
RTOG	Radiation Therapy Oncology Group
SA	Simulated Annealing
SC	Superposition/Convolution
TERMA	Total Energy Released per unit Mass
TLP	Table Lookup

List of Copyrighted Material

The material in Chapter 2 has been published in *Radiotherapy and Oncology* 85 (2007), 299-305 and is copyrighted by the publisher *Elsevier*.

The material in Chapter 3 has been published in *Medical Physics* 34 (2007), 3951-3961 and is copyrighted by the publisher the *American Association of Physicists in Medicine*.

The material in Chapter 4 has been submitted for peer review to *Medical Physics* and if accepted for publication will be copyrighted by the publisher the *American Association of Physicists in Medicine*.

The material in Chapter 5 has been accepted for publication (currently in press) in *Medical Physics* and is copyrighted by the publisher the *American Association of Physicists in Medicine*.

CHAPTER ONE: INTRODUCTION

1.1 Background

An estimated 159,900 new cases of cancer and 72,700 deaths from cancer will occur in Canada in 2007 [1]. Approximately 50% of these cancer patients will receive radiation therapy as a component of their treatment. The majority of radiation therapy treatments are performed using high energy photon beams generated by a medical linear accelerator (Figure 1.1) and are referred to as external-beam radiotherapy (EBR).

Figure 1.1: A medical linear accelerator used to produce high energy photon beams for the treatment of cancer.

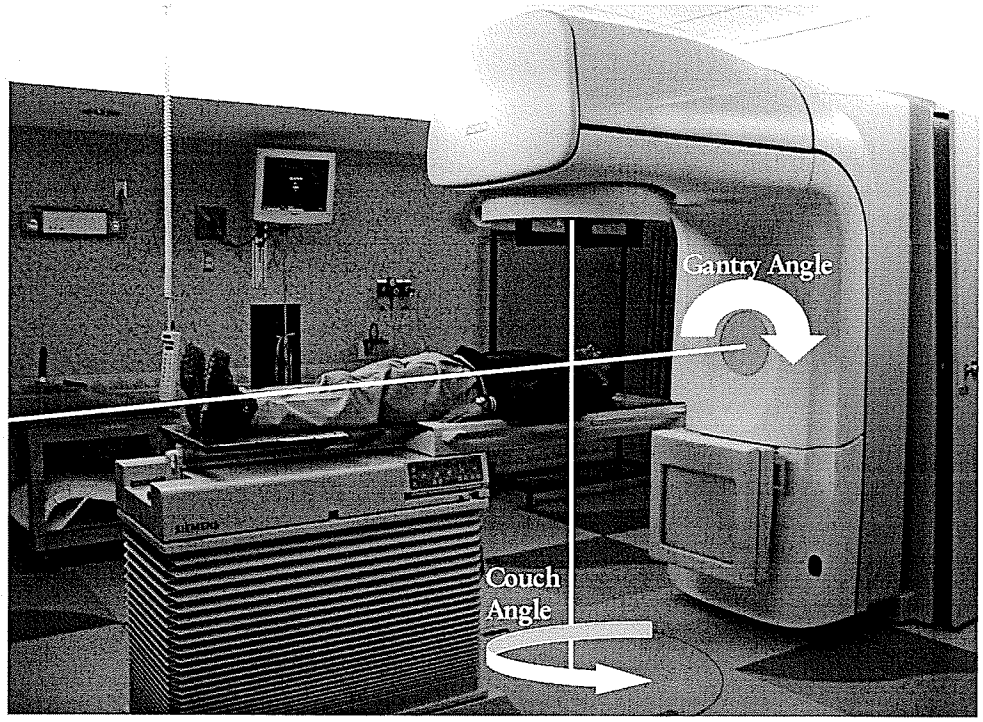

The linear accelerator uses high-frequency electromagnetic waves to accelerate electrons to high energies through a linear waveguide [2]. The high-energy electron beam strikes a target to produce bremsstrahlung X-rays [3]. The X-ray beam traverses a flattening filter to produce a uniform intensity profile across the beam. A device such as a multi-leaf collimator (MLC) is used to collimate the X-ray beam before it exits the machine. The MLC (Figure 1.2) consists of a large number of opposing metallic leaves that can be controlled independently of each other to generate a complexly shaped field. The thickness of the leaves along the beam direction is sufficient to nearly completely block the beam (typically transmission of less than 3%, but the actual value depends on the manufacturer).

Figure 1.2: A multi-leaf collimator (MLC) used to generate a treatment aperture.

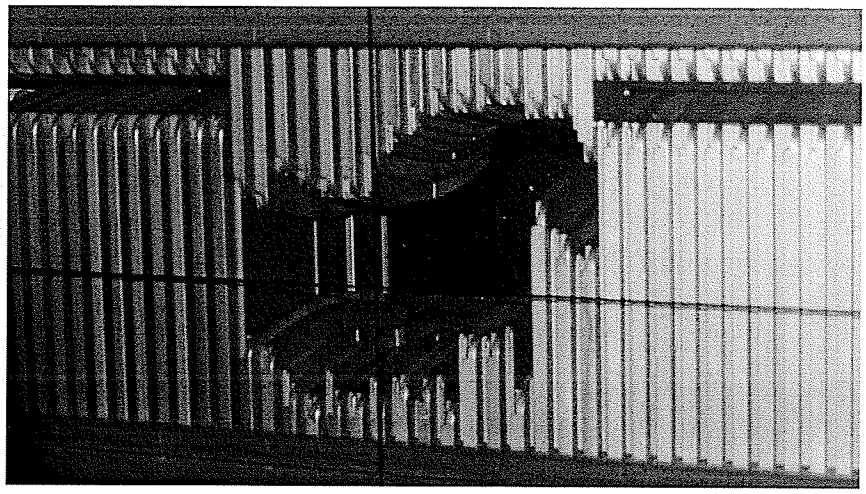

As the beam of X-rays traverses through the patient, it is attenuated according to the following equation:

$$N = N_0 e^{-\mu d} \tag{1.1}$$

where N_0 is the number of photons in the beam striking the patient of thickness d, and μ is the linear attenuation coefficient. The quantity μ is actually the sum of the individual attenuation coefficients for three photon interaction processes with matter pertinent to radiation therapy. These include: the photoelectric effect, Compton scattering, and pair production [3]. Other photon interaction processes such as coherent scattering and photonuclear interactions are not as important at radiotherapy energies. For example, for an atomic number approximately equal to that of tissue, Z = 7, the photoelectric effect is the dominant interaction below about 30 keV. Above 30 keV, the Compton effect becomes dominant and remains so until approximately 24 MeV, at which point pair production becomes the dominant interaction. The majority of EBR treatments are performed using polyenergetic megavoltage X-ray beams of 4-25 MV with maximum spectral energies of 4-25 MeV. Lower energy X-ray beams are selected for relatively superficial targets (μ = 0.034 cm^{-1} at 4 MeV in water) while deeper targets require more 'penetrating' beams of higher energy (μ = 0.018 cm^{-1} at 25 MeV in water). At EBR treatment energies, the Compton effect is the dominant photon interaction mechanism. In Compton scattering, a photon interacts with a loosely bound orbital electron and part of the incident photon's energy is transferred as kinetic energy to the electron while the remaining energy is carried away by a 'scattered' photon. The ejected Compton electron, being surrounded by it's Coulomb electric force field, interacts with electrons or with the nucleus of atoms along it's trajectory and gradually transfers it's kinetic energy to the

surrounding tissue. A measure of the energy absorbed per unit mass of tissue is defined as the dose, and the unit associated with dose is the Gray (1 Gy = 1 J/kg).

Typically, a radiation therapy treatment plan is designed before delivering a curative patient treatment. In this process, a human operator simulates the incidence of radiation beams on a computer model of the patient (usually computed tomography data) using a commercial treatment planning computer. The evaluation of the quality of a treatment plan requires the computation of the dose distribution within the patient. The development of a treatment plan is usually an iterative process, requiring operator intervention and subsequent recalculation of dose for plan evaluation.

The calculation of dose is non-trivial because, in general, the transport of radiation is governed by the Boltzmann transport equation:

$$\vec{\Omega} \bullet \vec{\nabla}\Psi(\vec{r},E,\vec{\Omega}) + \mu_t(\vec{r},E)\Psi = \int_{E'}\int_{4\pi} \mu(\vec{r},E' \rightarrow E;\omega_0)\Psi(\vec{r},E',\vec{\Omega'})d\Omega' dE' + Q_A(\vec{r},E,\vec{\Omega}) \qquad (1.2)$$

where $\Psi(\vec{r},E,\vec{\Omega})$ is the angular flux density [particles/(cm^2 · MeV · sr · s)] at spatial point $\vec{r}$, energy E, at direction vector $\vec{\Omega}$, Q_A is the energy and directional-dependent photon source [cm^{-3} · MeV^{-1} · sr^{-1} · s^{-1}] (e.g., from the accelerator target), μ_t is the total linear attenuation coefficient, $\mu(\vec{r},E' \rightarrow E;\omega_0)$ is the double-differential transfer coefficient [cm^{-1} · MeV^{-1} · sr^{-1}], corresponding to the probability per cm traveled that a photon with energy E' and direction $\vec{\Omega'}$ will interact with medium at $\vec{r}$ to produce

secondary photons with energy E, traveling in a new direction $\vec{\Omega}$ such that $\vec{\Omega} \bullet \vec{\Omega'} = \omega_0$, with ω_0 = cosine of scatter angle.

Although deterministic approaches of numerically solving the Boltzmann transport equation are possible [4, 5], the Monte Carlo (MC) stochastic method is generally accepted as the 'gold standard' for radiotherapy calculations involving complex geometries [6, 7]. However, routine use of MC dose calculations in clinical practice has been hindered by long simulation times. Alternatively, the 'convolution/superposition' dose calculation method [8, 9], most commonly used and implemented in commercial treatment planning systems (including Pinnacle^3, Philips Radiation Oncology Systems, Milpitas, CA, USA), achieves a reasonable compromise between the speed of computation and accuracy in dose. In this approach, the dose at any point (x, y, z) within the patient, $D(x, y, z)$, from energy released at a point (x', y', z') is the convolution between TERMA (Total Energy Released per unit MAss) $T(x, y, z)$ and the dose kernel $K(x, y, z)$:

$$D(x,y,z) = \iiint T(x',y',z')K(x-x',y-y',z-z')dx'dy'dz' \tag{1.3}$$

where $K(x-x', y-y', z-z')$ is the convolution kernel representing the relative energy deposited per unit volume about the site of primary photon interactions. The TERMA is given by:

$$T(x,y,z) = \frac{\mu}{\rho}\Psi(E,x,y,z) \tag{1.4}$$

where μ/ρ is the mass attenuation coefficient and $\Psi(E,x,y,z)$ is the primary energy fluence distribution in the patient. For example, the primary energy fluence of a monoenergetic photon beam with energy E is given by:

$$\Psi(E,x,y,z) = \Phi_0 E e^{-\mu d} \tag{1.5}$$

where Φ_0 is the fluence at the surface of the patient, μ is the linear attenuation coefficient, and d is the depth from the surface. For a polyenergetic photon beam, the dose kernel and photon spectrum (used to compute the TERMA) are pre-calculated via MC simulation [9-11]. The 'convolution' method assumes a spatially invariant kernel. Unfortunately, the presence of tissue inhomogeneities in the patient invalidates this assumption. However, the calculation may be modified to account for variations in tissue density. At present, the density-scaling method is used to distort the kernel by finding the average density along the straight-line path between the interaction site and dose deposition sites [8]. The use of a spatially variant kernel is termed 'superposition'. The majority of the dose is contributed by primary electrons (primary kernel) and first-scattered photons (first-scatter kernel). For the first-scattered photons, the density-scaling method is a good approximation because the photons travel in straight lines and the mass attenuation coefficient scales linearly with material density, if the atomic number remains unchanged. However, the density-scaling method is less accurate for the primary electrons which are multiply-scattered. In computing dose for lung cancer treatments, an overestimation in dose of up to 8% just beyond the tissue-to-lung interface can result because the 'convolution/superposition' method does not consider the multiple scattering of electrons when distorting the primary kernel to account for tissue inhomogeneities [8]. Errors are also observed for other types of tissue interfaces such as bone, but the electron

ranges are very short in dense materials resulting in an incorrect local dose over a much smaller volume [12]. The simple density-scaling method can be applied to the total kernel, but with less accuracy than the first-scatter kernel case, because other types of interactions, such as multiply-scattered photons, produce dose components which are not affected only by the first-scatter path of photons and electrons. Multiply-scattered photons, on average, interact throughout the entire volume of the absorbing medium. Therefore, a more specific density-scaling method for higher order scattering events was proposed by Mackie *et al.* [13]. In this method, the primary and first-scatter kernels are scaled using the average density between the interaction site and dose deposition sites, while the higher order kernels are scaled using the average density of the whole absorber. In general, the 'convolution/superposition' method can compute dose distributions with an accuracy of 2% in homogenous media [14] and 5% in heterogeneous media [15] making it the preferred choice for fast (compared to MC) yet reasonably accurate dose calculations in radiotherapy.

1.1.1 Biologic Basis of Radiation Therapy

The basic principle of radiation therapy is the destruction of all cancer cells without killing so many normal cells as to cause medical complications, especially long-term complications or late reactions [16]. Damage to deoxyribonucleic acid (DNA) in the nucleus of a cell is the primary mechanism by which ionizing radiation kills cells. A photon interaction can produce free radicals as a result of local ionizations in water which, in turn, interact with DNA to inhibit damage repair mechanisms. Absorption of

the photon energy destabilizes a molecule, resulting in molecular bond breaks or release of energetic electrons and scattered photons, which may interact with other cellular molecules, leading to a chain reaction that produces a variety of chemically unstable free radicals (hydroxyl, hydrated electrons, hydrogen atoms, and hydrogen peroxide). The most common lethal damage (resulting in cell death) due to ionizing radiation is the production of DNA double-strand breaks. Other general forms of non-lethal DNA damage include base damage, and single-strand breaks. Cells repair a significant proportion of radiation-induced, non-lethal DNA damage. Long-term biologic consequences are the result of those injuries which are irreparable (lethal) or misrepaired. Radiation therapy treatments are *fractionated* by delivering a daily dose of 1.5-3 Gy for 5 days per week over the course of 2-8 weeks. Dividing a dose into a number of fractions helps spare normal tissues because of repair of non-lethal damage between dose fractions and also repopulation of cells. Fractionation also increases damage to the tumour because it allows hypoxic portions of the tumour to be oxygenated (reoxygenation), decreasing their capability to repair radiation damage (the presence of oxygen inhibits DNA repair), and reassortment of cells into radiosensitive phases of the cell cycle [17].

1.1.2 Three Dimensional Conformal Radiation Therapy

Three-dimensional conformal radiation therapy (3D-CRT) refers to a process in which image-based 3D treatment planning is performed with the goal of conforming the spatial distribution of the prescription dose to the target volume(s) and simultaneously minimizing the dose to surrounding normal tissues. Volumetric imaging technologies

such as X-ray computed tomography (CT) and magnetic resonance imaging (MRI) provide a fully 3D model of the patient anatomy that allows for the identification of the "gross" tumour volume (GTV) and it's relationship with critical normal structures. The International Commission on Radiation Units and Measurements (ICRU) defines the GTV as the "gross demonstrable extent and location of the malignant growth" [18]. The GTV may include primary tumour, involved lymph nodes, and metastatic disease which can be visually demonstrated by any imaging modality. In addition to the demonstrable disease, the patient is likely to have microscopic subclinical disease that is known to be present but cannot be visualized. Therefore, a sufficient margin must be added to the GTV to include the microscopic disease. The GTV plus this margin is defined as the "clinical" target volume (CTV) and is determined by the Radiation Oncologist (physician specialist). In order to account for patient movement, organ motion, organ shape and size variation, and uncertainties in beam placement, margins are added to the CTV to define the final "planning" target volume (PTV) which must be irradiated to the prescription dose to ensure that the CTV is actually irradiated to the desired dose. In addition to ensuring adequate dose to the PTV, the treatment plan must also account for the presence of uninvolved tissue. The ICRU defines an organ-at-risk (OAR) to be an organ that, if given an excess radiation dose, would compromise the success of the treatment (i.e., result in significant medical complications). Through clinical trials and experience, tolerance doses to normal organs have been determined [19].

Planning of conventional 3D-CRT involves a time consuming trial-and-error procedure performed by a human operator. Treatment planning computers assist the

dosimetrist (human operator) by calculating the 3D patient dose distribution for given treatment parameters (beam orientations, beam energy, beam weights) however, the optimization of the planned treatment is performed manually. Once the GTV and OARs have been physically delineated on the CT data, the number and orientation of beams must be selected. The beam's-eye-view (BEV) projection [20] is used to help determine beam directions and define beam apertures. In a BEV image, the projections of the target and normal structures are displayed on the screen as if being viewed from the source of radiation along the central axis of the beam. The BEV is used as a planning tool to manually limit the volume of OARs exposed in the beam aperture and thus minimize dose to OARs. Digitally reconstructed radiographs (DRRs), radiographs computed by projecting ray lines through a volumetric CT data set [21], can also be superimposed on the BEV image to provide a planar reference image of the patient (Figure 1.3).

Figure 1.3: A beam's-eye-view (BEV) image superimposed on a digitally reconstructed radiograph (DRR) of a head-and-neck cancer patient. Anatomical structures (spinal cord in blue, glottic larynx in orange, parotid gland in purple, mandible in forest green, neck lymph nodes in light green, and tumour in red) inside the beam aperture (defined by the MLC leaves in the image) can be visualized.

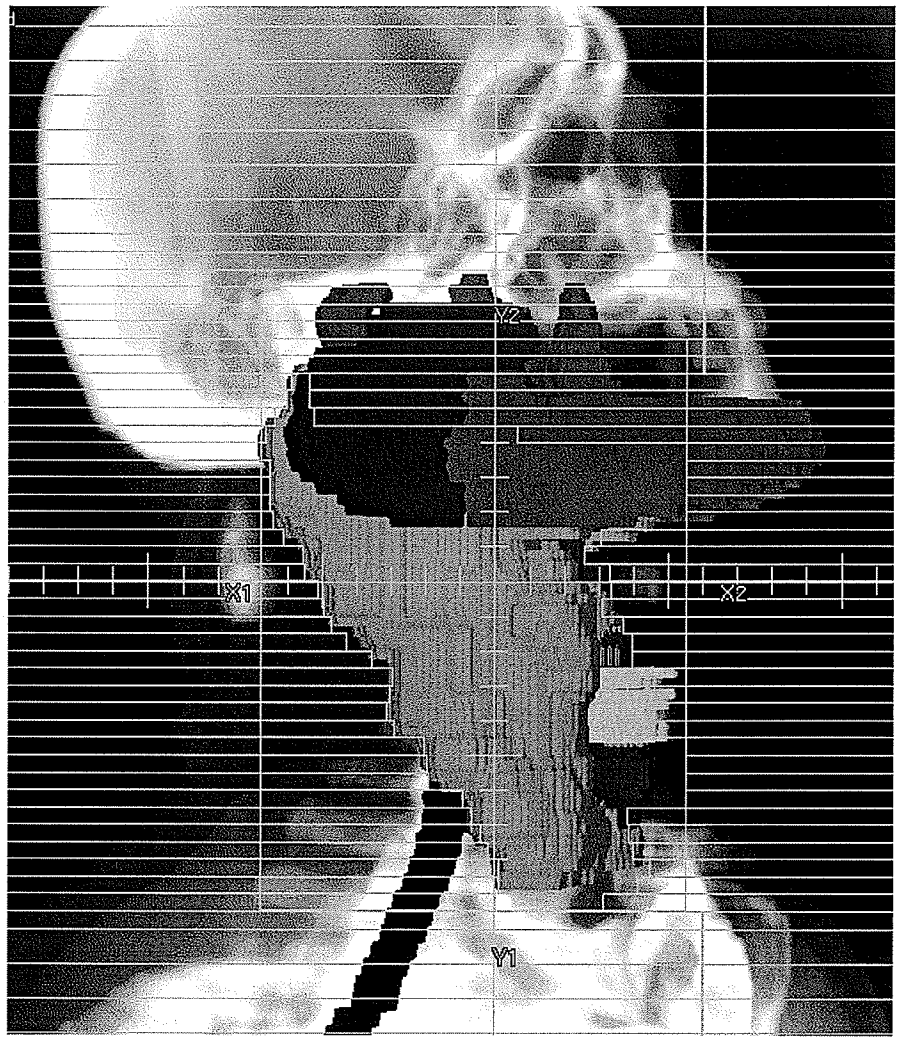

Once all beam orientations and beam energies have been selected, the 3D dose distribution is computed and spatially superimposed on the CT slices. The treatment plan is evaluated based on the quality of the dose distribution in covering the PTV with the prescription dose and limiting dose to OARs. The large amount of dosimetric data that must be analyzed can be summarized using a dose-volume histogram (DVH), a tool for evaluating treatment plans. Two types of DVHs, differential and cumulative, may be used in 3D-CRT planning [22]. In a differential DVH, the volume under consideration is divided into a 3D grid of volume elements (voxels), the size of which is small enough that the dose can be assumed to be constant within one voxel. The volume's dose distribution is then divided into dose bins and the voxels grouped according to dose bin. A differential DVH is a plot of the number of voxels in each bin versus the bin dose range. A cumulative DVH is a plot in which each bin represents the volume that receives a dose equal to or greater than an indicated dose. The value at any dose bin in a cumulative DVH is computed by summing the number of voxels of the corresponding differential DVH dose bin and all bins of higher dose. Typically, the cumulative DVHs are evaluated for the target and OARs to determine whether the plan satisfies the dose-volume prescription to the target (e.g. at least 95% of the PTV must receive the prescription dose) and whether the plan does not exceed the dose-volume or maximum dose tolerance of particular OARs. If certain planning objectives are not met (i.e. violation of the dose-volume tolerance of an OAR), the plan may be manually adjusted (i.e. number of beams, beam orientations, beam weighting) iteratively.

Conventional 3D-CRT is delivered one field at a time with a set of fixed radiation beams which are shaped by the MLC to conform to the PTV according to the BEV projection. The radiation beams normally have uniform intensities across the field, or have very simple intensity modulation (1-dimensional) by fluence-modifying devices such as wedges. However, there is a limit to the conformity of the dose distribution that is possible with conventional 3D-CRT. The use of uniform intensities and manual beam weight adjustment does not always result in the desired dose distribution in complex cases, such as tumours that surround OARs or are surrounded by many OARs and irregularly shaped (i.e. concave) tumours. Tumours like those in the head-and-neck, prostate, and lung have been difficult to treat using dose escalation with 3D-CRT without compromising OAR tolerances [23-25].

1.1.3 Intensity Modulated Radiation Therapy

Introduced into clinical practice in the early 1990s [26, 27], intensity-modulated radiation therapy (IMRT) represents a new form of radiation therapy in which a computer-aided optimization process is used to determine customized, non-uniform fluence distributions to satisfy the dosimetric objectives [28]. The fluence modulation at delivery is accomplished by individualized control of each collimation leaf of the MLC. The optimization process typically decomposes a broad beam into small 'beamlets' (typically 1 x 1 cm^2) and assigns a different intensity to each beamlet. The ability to modulate the intensity of individual beamlets within each beam represents a large number of degrees of freedom to produce a complex intensity distribution. This allows IMRT to

achieve higher target dose conformity and provides the potential for increased sparing of OARs to an extent not possible with 3D-CRT [29-32]. In contrast to 'forward planning' used in 3D-CRT and involving optimization by a human, IMRT employs an 'inverse planning' process in which the desired dosimetric and clinical objectives are stated mathematically in the form of an *objective function (OF)* which quantifies the quality of a treatment plan. A typical OF is defined as a weighted square of differences between calculated and desired doses for all voxels in every tissue of interest. This type of OF is called the "variance" or "quadratic" OF [28]. Therefore, a typical dose-based or dose-volume-based OF is the sum of the variance terms representing dose within each anatomic structure weighted with appropriate importance factors to differentiate different OARs, different OF parameters (i.e. minimum dose objectives, maximum dose objectives, multiple dose-volume objectives) and the target(s). For example, suppose the Radiation Oncologist prescribes the following clinical objectives for a prostate cancer patient: a dose of 79.2 Gy to the PTV, no more than 15% of the rectum (OAR) to receive a dose of 75 Gy, and the maximum dose in the rectum to not exceed 80 Gy. First, to ensure the target receives a uniform dose of 79.2 Gy, a uniform PTV prescription dose objective (D_{presc} = 79.2 Gy), a minimum PTV dose objective (at least 95% of D_{presc}, D_{min} = 75.2 Gy, to prevent underdosing), and maximum PTV dose objective (no more than 107% of D_{presc}, D_{max} = 84.7 Gy, to prevent overdosing), can define the OF for the PTV:

$$OF_{PTV} = \frac{1}{N_{PTV}} \left[\begin{array}{l} \sum_{i=1}^{N_{PTV}} (D_i - D_{presc})^2 \\ + W_{PTV_{\min}} \sum_{i=1}^{N_{PTV}} (D_i - D_{\min})^2 \Theta(D_{\min} - D_i) \\ + W_{PTV_{\max}} \sum_{i=1}^{N_{PTV}} (D_i - D_{\max})^2 \Theta(D_i - D_{\max}) \end{array} \right] \tag{1.6}$$

where N_{PTV} is the number of voxels in the PTV, D_i is the calculated dose to voxel i, and $W_{PTV_{\min}}, W_{PTV_{\max}}$ are the importance factors for the PTV minimum and maximum dose objectives. $\Theta(x)$ is the Heaviside function where:

$$\Theta(x) = \begin{cases} 1 & x \geq 0 \\ 0 & x < 0 \end{cases} \tag{1.7}$$

The first, second, and third terms of the OF_{PTV} penalize any PTV voxels if $D_i \neq D_{presc}$, $D_i < D_{\min}$, and $D_i > D_{\max}$, respectively. Similarly, by specifying a rectal maximum dose objective (D_{max} = 80 Gy) and a rectal dose-volume objective (at least 85% of rectal volume less than D_{dv} = 75 Gy) we can define the rectal OF as:

$$OF_{\mathrm{Rectum}} = \frac{1}{N_{\mathrm{Rectum}}} \left[\begin{array}{l} W_{\mathrm{Rectum}_{\max}} \sum_{i=1}^{N_{\mathrm{Rectum}}} (D_i - D_{\max})^2 \Theta(D_i - D_{\max}) \\ + W_{\mathrm{Rectum}_{dv}} \sum_{i=1}^{N_{dv}} (D_i - D_{dv})^2 \Theta(D_i - D_{dv}) \end{array} \right] \tag{1.8}$$

where N_{Rectum} is the number of voxels in the rectum, N_{dv} is the number of rectal voxels (at least 85% of the total number of rectal voxels) whose dose must be below the dose-volume objective dose D_{dv}, and $W_{\mathrm{Rectum}_{\max}}, W_{\mathrm{Rectum}_{dv}}$ are the importance factors for the rectal maximum dose and dose-volume objectives. Thus, the total OF which must be optimized for this example is given by:

$$OF = OF_{PTV} + OF_{\mathrm{Rectum}} \tag{1.9}$$

The specific terms in the OF for a particular patient are defined by the human operator, in an attempt to drive the optimization to satisfy the clinical objectives of the Radiation Oncologist.

In general, there exist two types of IMRT optimization algorithms for minimizing the OF: deterministic and stochastic. The most common deterministic approach is the gradient-based method [27, 33-36]. This technique iteratively adjusts the beamlet intensities, calculates a gradient vector of the OF (as the direction of minimization), and takes steps along the direction of the gradient vector. For example, in the 'steepest descent' method, the intensity for one beamlet is adjusted according to the following:

$$I_j^{k+1} = I_j^k + s\frac{\partial OF}{\partial I_j}^k \tag{1.10}$$

where I_j is the intensity for the jth beamlet, k is the iteration number, $\frac{\partial OF}{\partial I_j}^k$ is the derivative of the OF with respect to the intensity for the jth beamlet, and s is the size of the step. The advantage of gradient methods is that they are generally fast and efficient. However, gradient methods require that the OF be convex (contains one global minimum with no alternative local minima) otherwise the search could potentially be trapped in a local minimum. If multiple local minima are known to exist, a stochastic optimization technique may need to be considered. Simulated annealing (SA) is a commonly used stochastic method in radiotherapy optimization which mimics the behavior of a system of interacting particles that are progressively cooled and allowed to maintain thermal equilibrium while reaching the ground state [37-41]. At each iteration, a small change, either positive or negative and of varying magnitude, is made in a beamlet intensity. If the OF decreases, then the change is accepted. If the OF increases, the change is not automatically rejected, but accepted with a probability of:

$$P = e^{-\frac{\Delta OF}{kT}} \tag{1.11}$$

where ΔOF is the increase of the OF, k is Boltzmann's constant, and T is the system 'temperature'. By accepting changes that actually worsen the dose distribution, SA has the potential to avoid becoming trapped in local minima. The ability to escape local minima may be important when dose-volume-based OFs are employed, which have been demonstrated to contain multiple local minima [42, 43]. As the number of iterations increases, the 'temperature' is gradually reduced and thus the probability of accepting solutions with higher OF is also reduced. However, SA typically requires many more iterations to find an acceptable solution, resulting in longer convergence times than gradient-based methods.

Conventional MLC-based IMRT planning is performed in two sequential steps: minimization of the OF to produce a set of optimal beamlet intensities ("intensity maps") for each beam orientation, followed by MLC leaf sequencing (or 'conversion' to a deliverable set of MLC positions). In the second step, an ideal intensity map is decomposed into a set of MLC-formed apertures by using a leaf sequencing algorithm, which specifies the leaf positions as a function of the X-ray beam delivery time (monitor units). The type of leaf sequencing algorithm used depends on the IMRT delivery technique. In general, MLC-based delivery can be divided into dynamic (or sliding-window) [27, 44-48] and static ('step-and-shoot' or segmental) modes [33-41]. In dynamic delivery, the MLC leaves move continuously while the X-ray beam is on. In contrast, during static delivery, the MLC leaf movements ('step') and X-ray beam delivery ('shoot') are executed sequentially. In static delivery, a series of different MLC shapes ("segments") are delivered at each beam orientation (Figure 1.4) such that the

total dose to the patient is the accumulation of contributions for a series of segment fields (typically, the number of segments is between 20 and 150 for an entire treatment delivery).

Figure 1.4: (a) An example of an IMRT intensity map for a head-and-neck cancer patient. (b) All MLC segments for this intensity map.

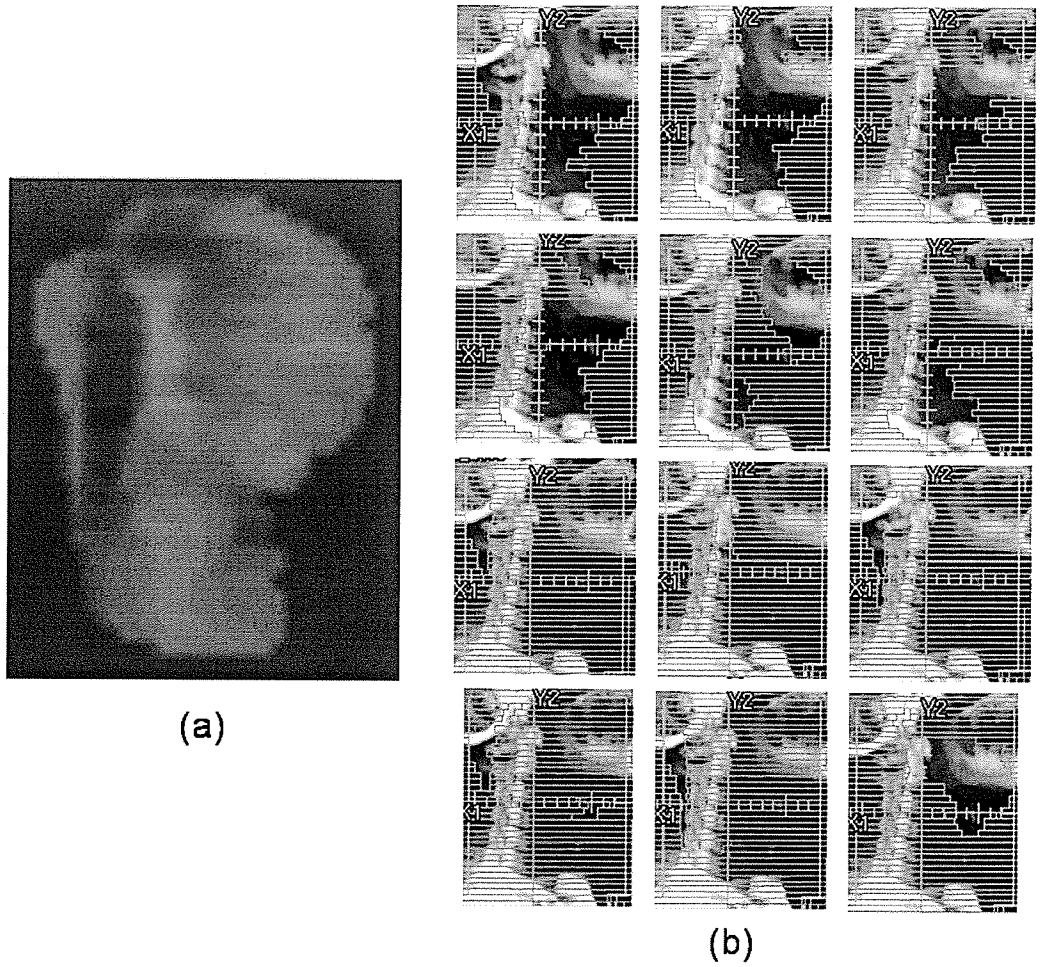

However, a disadvantage of static MLC delivery lies with the conversion of the optimized intensity maps to deliverable MLC segments by the leaf sequencing algorithm. This process may result in degradation of the optimal plan, since the intensity map delivered by the segments is not exactly the same as the optimized intensity map. This can be the result of a limited number of discrete intensity levels used to approximate the continuous optimal intensity map, but also due to the fact that the physical characteristics of the MLC are not taken into account during optimization. Therefore, the optimal dose distribution requested by the inverse planning step may not be actually deliverable.

Direct aperture optimization (DAO) is a method for planning static IMRT which eliminates the conversion step and, therefore, the differences between the optimized and deliverable dose distributions [49-51]. In DAO, segments are optimized directly without using the beamlet concept. That is, the MLC leaf positions for each segment and the segment weights are the variables for the optimization. The user only needs to specify the maximum number of segments per beam orientation and the MLC characteristics are directly incorporated into the optimization.

1.1.4 Beam Orientation Optimization

A fundamental problem in radiation therapy treatment planning is the selection of a suitable number of beams and their 3D orientation. The individual patient anatomy such as the location and shape of the PTV, and the OARs influence the choice of a beam configuration. A typical patient treatment will involve multiple beams of radiation from

different orientations. This technique results in a lower dose to normal tissues surrounding the tumour (and a higher dose to the tumour) since the beams intersect at the tumour. As with 3D-CRT, the incident beam orientations used in IMRT are still determined using a manual trial-and-error search and are usually not optimal [52]. Therefore, it would be advantageous to incorporate an automated beam orientation optimization (BOO) algorithm into the radiation therapy planning process.

A radiation beam orientation can be specified by two distinct angles: the 'head' (gantry) of the linear accelerator can rotate 360° in a plane defining a gantry angle, and the patient couch can also rotate 360° (in a plane perpendicular to the gantry motion plane) to define a couch angle (see Figure 1.1). The gantry and couch angles, in combination, can provide a large number of beam orientations. However, the selection of a set of optimal beam orientations to satisfy the primary objective of radiation therapy, to maximize dose in the tumour and minimize dose in surrounding normal tissue, is not a trivial problem. To appreciate the magnitude of the problem, suppose we perform an exhaustive search and only consider the 360° gantry angle space in 5° angular steps (with no couch rotation, i.e. coplanar), nearly 14 million combinations would need to be tested for five beams, nearly 1.5 billion combinations for seven beams and so on. Despite the enormous beam orientation search space, a BOO algorithm must have the capability of searching through this space in a clinically reasonable timeframe.

The recent past has produced several search techniques to automate the beam orientation selection process by using OFs based on dose criteria [52-89]. A drawback of

these optimization algorithms is that they require the calculation of dose distributions to evaluate a large number of possible solutions, a computationally intensive process resulting in clinically infeasible optimization times (several hours). This problem is especially complicated in IMRT where the beam intensity maps are coupled with the beam configurations, requiring beam intensity map optimization for every sampled beam configuration. Clearly, the search space is greatly enlarged when the beam orientations of the fields are included in the IMRT optimization. In addition, the calculation is further complicated by the highly non-convex dependence of the dosimetric OF on beam orientations which precludes any deterministic approach to its minimization [42]. In order to avoid becoming trapped in local minima, a stochastic or iterative global search method is thus needed for BOO (as opposed to faster, gradient-based methods). Consequently, these approaches have produced prohibitively long optimization times, thus hampering the clinical application of dosimetric BOO algorithms.

Pugachev *et al.* have recently proposed several approaches to BOO for IMRT [52, 67-70]. In the earliest proposal, a non-iterative, filtered back-projection (FBP) method using simple exponential attenuation to calculate dose for parallel beams, was used to solve the inverse problem in IMRT while the beam orientations were optimized using a simulated annealing method [70]. However, the algorithm was not generalized for 3D patient geometry, and only coplanar (gantry angle) optimizations for simple 2D phantoms were performed. Even with such simplifications, the time required for BOO was still 20 min. In later work, simulated annealing was also used for BOO while optimization of the beam intensity maps was achieved through iterative-least-square minimization of a

quadratic dose-based OF [52]. A typical prostate IMRT BOO required over 100 h for coplanar beams and over 200 h for noncoplanar beams. Analogous to the BEV in 3D-CRT, a beam's-eye-view dosimetrics (BEVD) method was proposed for IMRT with a computerized ranking of incident beam orientations [67, 68]. In BEVD, a score function evaluated quantitatively the "goodness" of each beamlet in a beam. The value of the score function was determined by the maximum dose deliverable to the PTV without exceeding the tolerance doses of the critical structures. The overall score of the beam orientation was the sum of the individual scores of all beamlets. This provided a measure of the goodness of a particular beam orientation; consideration of all orientations with the highest overall scores then allowed an informed selection of appropriate beams. However, this method was not able to take into account the true dose distribution resulting from the superposition of multiple fields. The effects of overlapping fields were taken into account by performing a simulated annealing search which was weighted towards the promising angles indicated by BEVD [69]. In this approach, BOO was performed in two steps. First, the quality of each possible beam orientation was evaluated using BEVD. A simulated annealing algorithm was then employed to search for the optimal set of beam orientations, taking into account the BEVD scores of different incident beam directions. During the calculation, sampling of gantry angles was weighted according to the BEVD score computed before the optimization. A beam direction with a higher BEVD score had a higher probability of being included in the trial configuration, and vice versa. The use of BEVD allowed a more efficient sampling of the search space since beams that had low BEVD scores (those that were not likely to produce an optimal dose distribution) were immediately rejected without going through the beam intensity

map optimization (iterative-least-square minimization of a quadratic dose-based OF). However, only coplanar beams were considered and, on average, the optimization still required more than 2 h.

Schreibmann *et al.* [76] developed a multiobjective BOO algorithm for IMRT employing a genetic algorithm to optimize the number of incident beams, their orientations, and the importance factors using a dosimetric variance-based OF while a gradient-based method optimized the intensity maps. For computational reasons, only coplanar optimizations were performed, however, this still required 2 h for a clinical prostate case. In later work, the authors used this algorithm to investigate coplanar beam orientation class solutions in prostate IMRT [77]. The framework of this IMRT BOO algorithm was subsequently used in conjunction with an angular ranking function based on the equivalent uniform dose (EUD), to model volumetric dose effects in sensitive structures [78]. The angular ranking function was calculated by optimizing beamlet intensities to deliver the maximum dose to the target volume without violating the EUD constraints of the sensitive structures. Based on the angular rank, a pool of candidate beam orientations were selected prior to entering the multiobjective genetic algorithm for IMRT plan optimization. However, the authors did not quantify any reduction in optimization time through the use of this *a priori* angular rank.

Gaede *et al.* reported a systematic approach to BOO for IMRT [48]. The algorithm began by searching for the best one-beam plan. This was accomplished by exhaustively searching the beam orientation space in 10° steps, optimizing the set of

beamlet intensities (gradient-based minimization of a least squares OF) for each beam orientation sampled, and choosing the beam orientation with corresponding optimal beamlet intensities. This beam orientation was then fixed, and the search for the second beam was performed. The beamlet intensities for each beam pair were then optimized and the set that minimized the OF was selected as the best two-beam plan. The algorithm proceeded to add beam orientations in this manner. An analysis of the beamlet intensities, based on predefined 'beam significance criteria,' was performed for every sampled beam orientation. The proposed 'beam significance criteria' required that one of the following must hold: 1) at least one beamlet of an incident beam must have a relative intensity of at least 0.15 (plans were normalized to 1.0 at the isocenter) or 2) at least two beamlets of an incident beam must have a relative intensity of at least 0.10. For example, if five beams were currently selected, and the search for the sixth beam caused the beamlet intensities of the third beam to fail the 'beam significance criteria', then the third beam was discarded and the iteration restarted with only the four selected beam orientations fixed. The algorithm would then search for the next best seventh beam excluding the beam previously eliminated. If the beamlet intensities of the most recent best beam selection failed the 'beam significance criteria' or if a beam orientation was eliminated from the plan and the beam orientation that replaced it did not improve the OF, the algorithm terminated. However, even though only coplanar beams were considered, a simple 2D (single 'slice') prostate-like phantom still required 22 minutes of optimization time.

Liu *et al.* employed a fast gradient algorithm to exhaustively search through all possible beam orientations and minimize a dose-volume-based OF for lung IMRT [65].

Histograms of the beam orientations preferred by the best 100 plans with the lowest OFs were generated and used to select beam orientations (which were most likely favored by these plans) to optimize a final IMRT plan. Nonetheless, for a typical lung case the total BOO time was 3 h for five beams and 10 h for seven beams on a system with eight CPUs.

Rowbottom *et al.* [72] developed a BOO algorithm for IMRT which was designed to avoid, if possible, beam orientations that pass through OARs with low radiation tolerance (i.e. contralateral parotid gland). A single-beam cost function was used to determine which beams pass through a particular OAR. The cost function determined the integral primary dose deposited in a given OAR for a particular gantry and couch angle pair. Any beams passing through the given OAR were removed from the subsequent multi-beam search space *a-priori.* A fast simulated annealing algorithm determined the 'optimal' beam arrangement while a gradient-decent technique optimized beam intensity maps using a clinically realistic OF incorporating dose-volume constraints for multiple structures. Despite only producing plans with a small number of IMRT fields (three and four), the BOO algorithm still required 3.5-4 h of optimization time.

Djajaputra *et al.* developed an IMRT BOO algorithm where successive sets of beam orientations were generated by using a 'fast' simulated annealing algorithm [58]. For each trial set of beam orientations, a gradient-based method optimized the beam intensity maps by minimizing a dose-volume-based OF. The beam intensity map optimization was accelerated by employing a fast, albeit approximate, dose calculation method that utilized a table lookup (TLP) dose kernel. In the TLP method, each dose

voxel was assigned only one beamlet from each beam, namely the beamlet whose ray-trace intersected the voxel. An initial dose to the voxel was calculated accurately using the superposition/convolution (SC) method for a uniform intensity map for all beams. The TLP kernel was then calculated using:

$$K_{ij} = \begin{cases} \dfrac{D_i}{W_j}, & \textit{if voxel } i \textit{ is on the path of beamlet } j \\ 0, & \textit{otherwise} \end{cases} \qquad (1.12)$$

where K_{ij} is the dose kernel, D_i is the dose to voxel i, and W_j is the weight (intensity) of beamlet j. In subsequent iterations, instead of computing an accurate dose using the SC method, dose was calculated by looking up the kernel. Therefore, both dose and kernel were approximate. Nevertheless, optimization times were still 1-2 h for simple prostate cases and 13-17 h for head-and-neck cases.

An alternative approach in reducing BOO times could be achieved by using different optimization criteria in the OF that are correlated with dosimetric quantities but do not involve calculating dose distributions. Only a few investigators have explored geometric (instead of dosimetric) BOO, however, these studies have been limited to 3D-CRT [90-93]. Meyer *et al.* [92] developed a cost function employing geometrical quantities, which consisted of PTV cost and OAR cost components, to automatically select beam orientations in 3D-CRT. The PTV cost was based on the exponential attenuation of the mean depth of the PTV. The OAR cost was a penalty term which depended on the amount of OAR irradiated in the beam. Each OAR cost component contained both a 'depth cost' and a 'volume cost' term. The OAR depth cost was based on the exponential attenuation of the mean depth of the OAR while the OAR volume cost

calculated the fractional volume of the OAR in the beam. In each clinical case presented, the optimized beam orientations resulted in better sparing of critical structures compared to plans with manual beam orientation selection. The time to perform a beam orientation search was only 2 min for coplanar and 12 min for non-coplanar beams. Haas *et al.* [91] first proposed the optimization of a geometric OF that aimed at geometrically conforming the 2D beam's intersection with the PTV surface while minimizing the intersection area between beams and OARs. A multi-objective genetic algorithm was employed to minimize the geometrical OF. However, the method was restricted to using only the most representative 2D CT slice, and many simplifications were used, such as assuming that the fields have no divergence. Schreibmann *et al.* [93] improved on the previous geometric method proposed by Haas *et al.* with the use of a true, 3D-volume computation which took into account beam divergence, concave shapes, as well as treatment settings such as individual beam shaping by blocks or multi-leaf collimators. The geometrical OF was optimized using an adaptive simulated annealing algorithm that used a re-annealing and adapted the cooling for each individual decision variable by analyzing its sensitivity to temperature changes. The method required only a few seconds to find an optimal set of beam orientations. However, in the brain case the authors presented, the geometric optimization produced a larger fraction of the brain (an organ-at-risk) containing higher dose values. This was because the solutions obtained by this geometrical model did not consider dose 'hot spots' caused by beam overlaps, an important consideration for limiting maximum doses to normal structures.

A geometry-based optimization has the potential to significantly reduce computation time and thereby make BOO clinically feasible. This thesis presents several fast, geometry-based optimization methods for beam orientation selection in IMRT which produce improved dose distributions, with the same or fewer beams as are used in current clinical practice. It is anticipated that the optimization methods presented in this thesis will become useful tools in the radiation therapy treatment planning process.

1.2 Thesis Proposal

This thesis is separated into four fundamental investigations. First, an exhaustive treatment planning study of coplanar equiangular-angular beam space was performed on a cohort of prostate IMRT patients to investigate the variation of the dose distribution with beam orientation. Second, a strong correlation between the beam intersection volume (BIV) and the subsequent IMRT dose distribution was theoretically derived and then observed on the prostate patient cohort. Third, a stochastic BOO algorithm generalized the BIV concept and produced improved IMRT dose distributions for a variety of clinical treatment sites. Finally, an algorithm for beam orientation selection in IMRT was developed which analyzed patient anatomy and produced optimal beam orientations based on geometric sparing of OARs and geometric target conformity. The investigations are briefly summarized in the next four subsections (abstracts of those works). The objective of this thesis is to develop and demonstrate several geometry-based BOO methods to produce optimized radiation therapy treatment plans in a clinically realistic time frame.

1.2.1 Optimal Starting Gantry Angles Using Equiangular-spaced Beams with Intensity Modulated Radiation Therapy for Prostate Cancer on RTOG 0126: A Clinical Study of 5 and 7 Fields

The purpose of this study was to investigate the effects of starting gantry angle and number of equiangular-spaced beams for prostate IMRT on the Radiation Therapy Oncology Group (RTOG) 0126 protocol. Static IMRT plans were generated for ten localized prostate cancer patients (prescribed to 79.2 Gy in 44 fractions) using five and seven equiangular-spaced beams. The starting gantry angles were incremented by 5° resulting in 15 (5 beams) and 11 (7 beams) plans per patient. Constant target coverage was ensured for all plans in order to isolate the variation in the rectal and bladder metrics as a function of starting gantry angle. It was observed that the variation with starting gantry angle in rectal metrics using 5 beams were statistically significant ($p < 0.001$) with dosimetric importance. The 5-beam rectal V 75 Gy (percentage volume receiving 75 Gy) and V 70 Gy demonstrated a class solution with a characteristic 'W' pattern and two optimal starting gantry angles near 20° and 50°. In contrast, statistically insignificant differences were observed for the bladder metrics using 5 beams and there was little dosimetric variation in the rectal and bladder metrics with 7 beams. Most importantly, nearly equivalent rectal V 75 Gy was achieved between 5 optimal equiangular-spaced beams starting at 20° (class solution) and 7 equiangular-spaced beams starting at 0° for most patients. Therefore, the use of an optimal starting gantry angle for 5 equiangular-spaced beams, as indicated by a class solution in this study, will facilitate rectal sparing and can produce plans that are equivalent to those employing 7 equiangular-spaced beams. This work is described in Chapter 2.

1.2.2 A Simple Geometric Algorithm to Predict Optimal Starting Gantry Angles Using Equiangular-spaced Beams for Intensity Modulated Radiation Therapy of Prostate Cancer

A fast, geometric BOO algorithm for clinical IMRT was implemented on ten localized prostate cancer patients on the RTOG 0126 protocol. The algorithm computed the beam intersection volume (BIV) within the rectum and bladder using 5 and 7 equiangular-spaced beams as a function of starting gantry angle for comparison to the V 75 Gy and V 70 Gy. A mathematical theory was presented to explain the correlation of BIV with dose and dose-volume metrics. The class solution 'W' pattern in the rectal V 75 Gy and V 70 Gy as a function of starting gantry angle using 5 equiangular-spaced beams (with two separate minima centered near 20° and 50°) was reproduced by the 5 BIV within the rectum. A strong correlation was found between the rectal 5 BIV and the rectal V 75 Gy and V 70 Gy as a function of starting gantry angle. The BOO algorithm predicted the location of the two dosimetric minima in rectal V 75 Gy and V 70 Gy (optimal starting gantry angles) to within 5°. It was demonstrated that the BIV geometric variations for 7 equiangular-spaced beams were too small to translate into a strong dosimetric effect in the rectal V 75 Gy and V 70 Gy. The relatively flat distribution with starting gantry angle of the bladder V 75 Gy and V 70 Gy was reproduced by the bladder 5 and 7 BIV for each patient. A geometric BOO method based on BIV has the advantage over dosimetric methods of simplicity and rapid computation time. This algorithm can be used as a standalone optimization method or act as a rapid calculation filter to reduce the search space for a dosimetric method. Given the clinically infeasible computation times of many dosimetric BOO algorithms, this robust geometric BIV algorithm has the

potential to facilitate beam angle selection for prostate IMRT in clinical practice. This work is described in Chapter 3.

1.2.3 A New Paradigm for Improving IMRT: Selection of Beam Orientations by Optimizing Beam Intersection Volume

A beam orientation optimization (BOO) algorithm based on optimizing beam intersection volume (BIV) components within an Organ-at-Risk (OAR) is proposed to improve conventional intensity-modulated radiation therapy (IMRT). A simulated annealing algorithm was employed to search for the optimal set of five beam orientations (5-opt) which simultaneously minimize the BIV components within an OAR. To account for target conformity, the variation of the geometric conformity index was also constrained during the optimization. The 5-opt plans were compared to standard 5, 7, and 9 equiangular-spaced beam plans (5-equi, 7-equi, 9-equi) for: (1) gastric (2) Radiation Therapy Oncology Group (RTOG) P-0126 prostate and (3) RTOG H-0022 oropharyngeal (Stage-III, IV) cancer patients. In the gastric case, the coplanar 5-opt plan reduced the right kidney V 20 Gy by 41.1%, 32.1%, and 29.5% compared to the 5-equi, 7-equi, and 9-equi plans. In the prostate case, the coplanar 5-opt plan improved rectal sparing over all standard plans with a reduction of the V 75 Gy, V 70 Gy, V 65 Gy, and V 60 Gy of 3.9%, 6.2%, 8.1%, and 10.6% compared to the 5-equi plan. In both oropharyngeal cases, the non-coplanar 5-opt plan substantially reduced the V 30 Gy and mean dose to the contralateral parotid compared to the 5-equi, 7-equi, and 9-equi plans: (Stage-III) 8.9%, 7.0%, 8.6% and 4.1 Gy, 2.5 Gy, 2.7 Gy (Stage-IV) 11.2%, 11.2%, 10.8% and 7.8 Gy, 7.9 Gy, 8.0 Gy. In conclusion, the method of optimizing BIV to produce substantial

improvements in OAR sparing over conventional IMRT has been demonstrated to be robust for application to a variety of IMRT treatment sites. This work is described in Chapter 4.

1.2.4 Improving Intensity Modulated Radiation Therapy Using the Anatomic Beam Orientation Optimization Algorithm

A novel, anatomic beam orientation optimization (A-BOO) algorithm is proposed to significantly improve conventional intensity-modulated radiation therapy (IMRT). The A-BOO algorithm vectorially analyses polygonal surface mesh data of contoured patient anatomy. Five optimal (5-opt) deliverable beam orientations are selected based on (1) tangential orientation bisecting the target and adjacent Organ's-at-Risk (OARs) to produce precipitous dose gradients between them and (2) parallel incidence with polygon features of the target volume to facilitate conformal coverage. The 5-opt plans were compared to standard 5, 7, and 9 equiangular-spaced beam plans (5-equi, 7-equi, 9-equi) for: (1) gastric (2) Radiation Therapy Oncology Group (RTOG) P-0126 prostate and (3) RTOG H-0022 oropharyngeal (Stage-III, IV) cancer patients. In the gastric case, the non-coplanar 5-opt plan reduced the right kidney V 20 Gy by 32.2%, 23.2%, and 20.6% compared to plans with 5, 7, and 9 equiangular-spaced beams. In the prostate case, the coplanar 5-opt plan produced similar rectal sparing as the 7-equi and 9-equi plans with a reduction of the V 75 Gy, V 70 Gy, V 65 Gy, and V 60 Gy of 2.4%, 5.3%, 7.0%, and 9.5% compared to the 5-equi plan. In the Stage-III and IV oropharyngeal cases, the non-coplanar 5-opt plan substantially reduced the V 30 Gy and mean dose to the contralateral

parotid compared to plans with 5, 7, and 9 equiangular-spaced beams: (Stage-III) 7.1%, 5.2%, 6.8% and 5.1 Gy, 3.5 Gy, 3.7 Gy (Stage-IV) 10.2%, 10.2%, 9.8% and 7.0 Gy, 7.1 Gy, 7.2 Gy. The geometry-based A-BOO algorithm has been demonstrated to be robust for application to a variety of IMRT treatment sites. Beam orientations producing significant improvements in OAR sparing over conventional IMRT can be automatically produced in minutes compared to hours with existing dose-based beam orientation optimization methods. This work is described in Chapter 5.

1.3 Bibliography

1. Canadian Cancer Statistics, National Cancer Institute of Canada, Toronto, Canada, April. 2007.
2. Khan, F.M., *The Physics of Radiation Therapy.* Lippincott Williams & Wilkins, Baltimore, 2nd Edition, 1994.
3. Attix, F.H., *Introduction to Radiological Physics and Radiation Dosimetry.* Wiley-Interscience, Toronto, 1986.
4. Gifford, K.A., J.L. Horton, et al., *Comparison of a finite-element multigroup discrete-ordinates code with Monte Carlo for radiotherapy calculations.* Phys Med Biol, 2006. **51**(9): p. 2253-65.
5. Williams, M.L., D. Ilas, et al., *Deterministic photon transport calculations in general geometry for external beam radiation therapy.* Med Phys, 2003. **30**(12): p. 3183-95.

6. Ma, C.M., E. Mok, et al., *Clinical implementation of a Monte Carlo treatment planning system.* Med Phys, 1999. **26**(10): p. 2133-43.

7. Sempau, J., S.J. Wilderman, et al., *DPM, a fast, accurate Monte Carlo code optimized for photon and electron radiotherapy treatment planning dose calculations.* Phys Med Biol, 2000. **45**(8): p. 2263-91.

8. Battista, J.J. and M.B. Sharpe, *True three-dimensional dose computations for megavoltage x-ray therapy: a role for the superposition principle.* Australas Phys Eng Sci Med, 1992. **15**(4): p. 159-78.

9. Papanikolaou, N., T.R. Mackie, et al., *Investigation of the convolution method for polyenergetic spectra.* Med Phys, 1993. **20**(5): p. 1327-36.

10. Liu, H.H., T.R. Mackie, et al., *A dual source photon beam model used in convolution/superposition dose calculations for clinical megavoltage x-ray beams.* Med Phys, 1997. **24**(12): p. 1960-74.

11. Sheikh-Bagheri, D. and D.W. Rogers, *Monte Carlo calculation of nine megavoltage photon beam spectra using the BEAM code.* Med Phys, 2002. **29**(3): p. 391-402.

12. Werner, B.L., I.J. Das, et al., *Dose perturbations at interfaces in photon beams: secondary electron transport.* Med Phys, 1990. **17**(2): p. 212-26.

13. Mackie, T.R., J.W. Scrimger, et al., *A convolution method of calculating dose for 15-MV x rays.* Med Phys, 1985. **12**(2): p. 188-96.

14. Lydon, J.M., *Photon dose calculations in homogeneous media for a treatment planning system using a collapsed cone superposition convolution algorithm.* Phys Med Biol, 1998. **43**(6): p. 1813-22.

15. Davidson, S.E., G.S. Ibbott, et al., *Accuracy of two heterogeneity dose calculation algorithms for IMRT in treatment plans designed using an anthropomorphic thorax phantom.* Med Phys, 2007. **34**(5): p. 1850-7.

16. Khan, F.M., *Treatment Planning in Radiation Oncology.* Lippincott Williams & Wilkins, Philadelphia, 2nd edition, 2007.

17. Hall, E.J., *Radiobiology for the Radiologist.* Lippincott Williams & Wilkins, Philadelphia, 5th edition, 2000.

18. International Commission on Radiation Units and Measurements. Prescribing, recording, and reporting photon beam therapy. ICRU Report 50, Bethesda, MD, 1993.

19. Emami, B., J. Lyman, et al., *Tolerance of normal tissue to therapeutic irradiation.* Int J Radiat Oncol Biol Phys, 1991. **21**(1): p. 109-22.

20. McShan, D.L., B.A. Fraass, et al., *Full integration of the beam's eye view concept into computerized treatment planning.* Int J Radiat Oncol Biol Phys, 1990. **18**(6): p. 1485-94.

21. Sherouse, G.W., K. Novins, et al., *Computation of digitally reconstructed radiographs for use in radiotherapy treatment design.* Int J Radiat Oncol Biol Phys, 1990. **18**(3): p. 651-8.

22. Drzymala, R.E., R. Mohan, et al., *Dose-volume histograms.* Int J Radiat Oncol Biol Phys, 1991. **21**(1): p. 71-8.

23. Ahamad, A., C.W. Stevens, et al., *Intensity-modulated radiation therapy: a novel approach to the management of malignant pleural mesothelioma.* Int J Radiat Oncol Biol Phys, 2003. **55**(3): p. 768-75.

24. Bragg, C.M., J. Conway, et al., *The role of intensity-modulated radiotherapy in the treatment of parotid tumors.* Int J Radiat Oncol Biol Phys, 2002. **52**(3): p. 729-38.

25. Nutting, C.M., D.J. Convery, et al., *Reduction of small and large bowel irradiation using an optimized intensity-modulated pelvic radiotherapy technique in patients with prostate cancer.* Int J Radiat Oncol Biol Phys, 2000. **48**(3): p. 649-56.

26. Bortfeld, T., A.L. Boyer, et al., *Realization and verification of three-dimensional conformal radiotherapy with modulated fields.* Int J Radiat Oncol Biol Phys, 1994. **30**(4): p. 899-908.

27. Bortfeld, T.R., D.L. Kahler, et al., *X-ray field compensation with multileaf collimators.* Int J Radiat Oncol Biol Phys, 1994. **28**(3): p. 723-30.

28. Perez, C.A., Brady, L.W., Halperin, E.C., Schmidt-Ullrich, R.K., *Principles and Practice of Radiation Oncology.* Lippincott Williams & Wilkins, Philadelphia, 4th Edition, 2004.

29. Chao, K.S., J.O. Deasy, et al., *A prospective study of salivary function sparing in patients with head-and-neck cancers receiving intensity-modulated or three-dimensional radiation therapy: initial results.* Int J Radiat Oncol Biol Phys, 2001. **49**(4): p. 907-16.

30. Kestin, L.L., M.B. Sharpe, et al., *Intensity modulation to improve dose uniformity with tangential breast radiotherapy: initial clinical experience.* Int J Radiat Oncol Biol Phys, 2000. **48**(5): p. 1559-68.

31. Xia, P., K.K. Fu, et al., *Comparison of treatment plans involving intensity-modulated radiotherapy for nasopharyngeal carcinoma.* Int J Radiat Oncol Biol Phys, 2000. **48**(2): p. 329-37.

32. Zelefsky, M.J., Z. Fuks, et al., *High dose radiation delivered by intensity modulated conformal radiotherapy improves the outcome of localized prostate cancer.* J Urol, 2001. **166**(3): p. 876-81.

33. Holmes, T. and T.R. Mackie, *A comparison of three inverse treatment planning algorithms.* Phys Med Biol, 1994. **39**(1): p. 91-106.

34. Spirou, S.V. and C.S. Chui, *A gradient inverse planning algorithm with dose-volume constraints.* Med Phys, 1998. **25**(3): p. 321-33.

35. Wu, Q. and R. Mohan, *Algorithms and functionality of an intensity modulated radiotherapy optimization system.* Med Phys, 2000. **27**(4): p. 701-11.

36. Xing, L. and G.T. Chen, *Iterative methods for inverse treatment planning.* Phys Med Biol, 1996. **41**(10): p. 2107-23.

37. Mageras, G.S. and R. Mohan, *Application of fast simulated annealing to optimization of conformal radiation treatments.* Med Phys, 1993. **20**(3): p. 639-47.

38. Morrill, S.M., K.S. Lam, et al., *Very fast simulated reannealing in radiation therapy treatment plan optimization.* Int J Radiat Oncol Biol Phys, 1995. **31**(1): p. 179-88.

39. Rosen, II, K.S. Lam, et al., *Comparison of simulated annealing algorithms for conformal therapy treatment planning.* Int J Radiat Oncol Biol Phys, 1995. **33**(5): p. 1091-9.

40. Webb, S., *Optimization by simulated annealing of three-dimensional, conformal treatment planning for radiation fields defined by a multileaf collimator: II. Inclusion of two-dimensional modulation of the x-ray intensity.* Phys Med Biol, 1992. **37**(8): p. 1689-704.

41. Cho, P.S., S. Lee, et al., *Optimization of intensity modulated beams with volume constraints using two methods: cost function minimization and projections onto convex sets.* Med Phys, 1998. **25**(4): p. 435-43.

42. Deasy, J.O., *Multiple local minima in radiotherapy optimization problems with dose-volume constraints.* Med Phys, 1997. **24**(7): p. 1157-61.

43. Wu, Q. and R. Mohan, *Multiple local minima in IMRT optimization based on dose-volume criteria.* Med Phys, 2002. **29**(7): p. 1514-27.

44. Spirou, S.V. and C.S. Chui, *Generation of arbitrary intensity profiles by dynamic jaws or multileaf collimators.* Med Phys, 1994. **21**(7): p. 1031-41.

45. Svensson, R., P. Kallman, et al., *An analytical solution for the dynamic control of multileaf collimators.* Phys Med Biol, 1994. **39**(1): p. 37-61.

46. Ma, L., A.L. Boyer, et al., *Synchronizing dynamic multileaf collimators for producing two-dimensional intensity-modulated fields with minimum beam delivery time.* Int J Radiat Oncol Biol Phys, 1999. **44**(5): p. 1147-54.

47. Stein, J., T. Bortfeld, et al., *Dynamic X-ray compensation for conformal radiotherapy by means of multi-leaf collimation.* Radiother Oncol, 1994. **32**(2): p. 163-73.

48. Chui, C.S., M.F. Chan, et al., *Delivery of intensity-modulated radiation therapy with a conventional multileaf collimator: comparison of dynamic and segmental methods.* Med Phys, 2001. **28**(12): p. 2441-9.

49. De Gersem, W., F. Claus, et al., *An anatomy-based beam segmentation tool for intensity-modulated radiation therapy and its application to head-and-neck cancer.* Int J Radiat Oncol Biol Phys, 2001. **51**(3): p. 849-59.

50. Shepard, D.M., M.A. Earl, et al., *Direct aperture optimization: a turnkey solution for step-and-shoot IMRT.* Med Phys, 2002. **29**(6): p. 1007-18.

51. Siebers, J.V., M. Lauterbach, et al., *Incorporating multi-leaf collimator leaf sequencing into iterative IMRT optimization.* Med Phys, 2002. **29**(6): p. 952-9.

52. Pugachev, A., J.G. Li, et al., *Role of beam orientation optimization in intensity-modulated radiation therapy.* Int J Radiat Oncol Biol Phys, 2001. **50**(2): p. 551-60.

53. Beaulieu, F., L. Beaulieu, et al., *Simultaneous optimization of beam orientations, wedge filters and field weights for inverse planning with anatomy-based MLC fields.* Med Phys, 2004. **31**(6): p. 1546-57.

54. Bedford, J.L. and S. Webb, *Elimination of importance factors for clinically accurate selection of beam orientations, beam weights and wedge angles in conformal radiation therapy.* Med Phys, 2003. **30**(7): p. 1788-804.

55. Bortfeld, T. and W. Schlegel, *Optimization of beam orientations in radiation therapy: some theoretical considerations.* Phys Med Biol, 1993. **38**(2): p. 291-304.

56. Das, S., T. Cullip, et al., *Beam orientation selection for intensity-modulated radiation therapy based on target equivalent uniform dose maximization.* Int J Radiat Oncol Biol Phys, 2003. **55**(1): p. 215-24.

57. de Pooter, J.A., A. Mendez Romero, et al., *Computer optimization of noncoplanar beam setups improves stereotactic treatment of liver tumors.* Int J Radiat Oncol Biol Phys, 2006. **66**(3): p. 913-22.

58. Djajaputra, D., Q. Wu, et al., *Algorithm and performance of a clinical IMRT beam-angle optimization system.* Phys Med Biol, 2003. **48**(19): p. 3191-212.

59. D'Souza, W.D., R.R. Meyer, et al., *Selection of beam orientations in intensity-modulated radiation therapy using single-beam indices and integer programming.* Phys Med Biol, 2004. **49**(15): p. 3465-81.

60. Gaede, S. and E. Wong, *An algorithm for systematic selection of beam directions for IMRT.* Med Phys, 2004. **31**(2): p. 376-88.

61. Hou, Q., J. Wang, et al., *Beam orientation optimization for IMRT by a hybrid method of the genetic algorithm and the simulated dynamics.* Med Phys, 2003. **30**(9): p. 2360-7.

62. Lee, E.K., T. Fox, et al., *Simultaneous beam geometry and intensity map optimization in intensity-modulated radiation therapy.* Int J Radiat Oncol Biol Phys, 2006. **64**(1): p. 301-20.

63. Li, Y., D. Yao, et al., *A particle swarm optimization algorithm for beam angle selection in intensity-modulated radiotherapy planning.* Phys Med Biol, 2005. **50**(15): p. 3491-514.

64. Li, Y., J. Yao, et al., *Automatic beam angle selection in IMRT planning using genetic algorithm.* Phys Med Biol, 2004. **49**(10): p. 1915-32.

65. Liu, H.H., M. Jauregui, et al., *Beam angle optimization and reduction for intensity-modulated radiation therapy of non-small-cell lung cancers.* Int J Radiat Oncol Biol Phys, 2006. **65**(2): p. 561-72.

66. Meedt, G., M. Alber, et al., *Non-coplanar beam direction optimization for intensity-modulated radiotherapy.* Phys Med Biol, 2003. **48**(18): p. 2999-3019.

67. Pugachev, A. and L. Xing, *Pseudo beam's-eye-view as applied to beam orientation selection in intensity-modulated radiation therapy.* Int J Radiat Oncol Biol Phys, 2001. **51**(5): p. 1361-70.

68. Pugachev, A. and L. Xing, *Computer-assisted selection of coplanar beam orientations in intensity-modulated radiation therapy.* Phys Med Biol, 2001. **46**(9): p. 2467-76.

69. Pugachev, A. and L. Xing, *Incorporating prior knowledge into beam orientation optimization in IMRT.* Int J Radiat Oncol Biol Phys, 2002. **54**(5): p. 1565-74.

70. Pugachev, A.B., A.L. Boyer, et al., *Beam orientation optimization in intensity-modulated radiation treatment planning.* Med Phys, 2000. **27**(6): p. 1238-45.

71. Rowbottom, C.G., V.S. Khoo, et al., *Simultaneous optimization of beam orientations and beam weights in conformal radiotherapy.* Med Phys, 2001. **28**(8): p. 1696-702.

72. Rowbottom, C.G., C.M. Nutting, et al., *Beam-orientation optimization of intensity-modulated radiotherapy: clinical application to parotid gland tumours.* Radiother Oncol, 2001. **59**(2): p. 169-77.

73. Rowbottom, C.G., M. Oldham, et al., *Constrained customization of non-coplanar beam orientations in radiotherapy of brain tumours.* Phys Med Biol, 1999. **44**(2): p. 383-99.

74. Rowbottom, C.G., S. Webb, et al., *Improvements in prostate radiotherapy from the customization of beam directions.* Med Phys, 1998. **25**(7 Pt 1): p. 1171-9.

75. Rowbottom, C.G., S. Webb, et al., *Beam-orientation customization using an artificial neural network.* Phys Med Biol, 1999. **44**(9): p. 2251-62.

76. Schreibmann, E., M. Lahanas, et al., *Multiobjective evolutionary optimization of the number of beams, their orientations and weights for intensity-modulated radiation therapy.* Phys Med Biol, 2004. **49**(5): p. 747-70.

77. Schreibmann, E. and L. Xing, *Feasibility study of beam orientation class-solutions for prostate IMRT.* Med Phys, 2004. **31**(10): p. 2863-70.

78. Schreibmann, E. and L. Xing, *Dose-volume based ranking of incident beam direction and its utility in facilitating IMRT beam placement.* Int J Radiat Oncol Biol Phys, 2005. **63**(2): p. 584-93.

79. Soderstrom, S. and A. Brahme, *Selection of suitable beam orientations in radiation therapy using entropy and Fourier transform measures.* Phys Med Biol, 1992. **37**(4): p. 911-924.

80. Soderstrom, S. and A. Brahme, *Which is the most suitable number of photon beam portals in coplanar radiation therapy?* Int J Radiat Oncol Biol Phys, 1995. **33**(1): p. 151-9.

81. Stein, J., R. Mohan, et al., *Number and orientations of beams in intensity-modulated radiation treatments.* Med Phys, 1997. **24**(2): p. 149-60.

82. Wang, C., J. Dai, et al., *Optimization of beam orientations and beam weights for conformal radiotherapy using mixed integer programming.* Phys Med Biol, 2003. **48**(24): p. 4065-76.

83. Wang, X., X. Zhang, et al., *Effectiveness of noncoplanar IMRT planning using a parallelized multiresolution beam angle optimization method for paranasal sinus carcinoma.* Int J Radiat Oncol Biol Phys, 2005. **63**(2): p. 594-601.

84. Wang, X., X. Zhang, et al., *Development of methods for beam angle optimization for IMRT using an accelerated exhaustive search strategy.* Int J Radiat Oncol Biol Phys, 2004. **60**(4): p. 1325-37.

85. Webb, S., *Optimizing the planning of intensity-modulated radiotherapy.* Phys Med Biol, 1994. **39**(12): p. 2229-46.

86. Woudstra, E. and B.J. Heijmen, *Automated beam angle and weight selection in radiotherapy treatment planning applied to pancreas tumors.* Int J Radiat Oncol Biol Phys, 2003. **56**(3): p. 878-88.

87. Woudstra, E., B.J. Heijmen, et al., *Automated selection of beam orientations and segmented intensity-modulated radiotherapy (IMRT) for treatment of oesophagus tumors.* Radiother Oncol, 2005. **77**(3): p. 254-61.

88. Wu, X. and Y. Zhu, *A mixed-encoding genetic algorithm with beam constraint for conformal radiotherapy treatment planning.* Med Phys, 2000. **27**(11): p. 2508-16.

89. Yang, R., J. Dai, et al., *Beam orientation optimization for intensity-modulated radiation therapy using mixed integer programming.* Phys Med Biol, 2006. **51**(15): p. 3653-66.

90. Ezzell, G.A., *Genetic and geometric optimization of three-dimensional radiation therapy treatment planning.* Med Phys, 1996. **23**(3): p. 293-305.

91. Haas, O.C., K.J. Burnham, et al., *Optimization of beam orientation in radiotherapy using planar geometry.* Phys Med Biol, 1998. **43**(8): p. 2179-93.

92. Meyer, J., S.M. Hummel, et al., *Automatic selection of non-coplanar beam directions for three-dimensional conformal radiotherapy.* Br J Radiol, 2005. **78**(928): p. 316-27.

93. Schreibmann, E., M. Lahanas, et al., *A geometry based optimization algorithm for conformal external beam radiotherapy.* Phys Med Biol, 2003. **48**(12): p. 1825-41.

CHAPTER TWO: OPTIMAL STARTING GANTRY ANGLES USING EQUIANGULAR-SPACED BEAMS WITH INTENSITY MODULATED RADIATION THERAPY FOR PROSTATE CANCER ON RTOG 0126: A CLINICAL STUDY OF 5 AND 7 FIELDS

This chapter is adapted from a manuscript entitled "Optimal Starting Gantry Angles Using Equiangular-spaced Beams with Intensity Modulated Radiation Therapy for Prostate Cancer on RTOG 0126: A Clinical Study of 5 and 7 Fields" by Peter Potrebko, Boyd McCurdy, James Butler, Adel El-Gubtan, and Zoann Nugent, published in *Radiotherapy and Oncology* 85 (2007), 299-305.

2.1 Introduction

Intensity-modulated radiation therapy (IMRT) for the treatment of prostate cancer has been shown to provide dosimetric improvements over three-dimensional conformal radiotherapy (3D-CRT) and, therefore, has gained widespread clinical acceptance [1-6]. It is common clinical practice to use coplanar equiangular-spaced beam arrangements for prostate IMRT in the supine [2] and prone [7] treatment positions. Zelefsky *et al.* at Memorial Sloan-Kettering Cancer Center (MSKCC) employs a small variation of an equiangular-spaced beam arrangement with a 5 field {posterior (0°), right posterior oblique (75°), right anterior oblique (135°), left anterior oblique (225°), left posterior oblique (285°)} prone treatment position technique [3-6, 8]. The MSKCC gantry angles have also been used in the supine treatment position [9]. However, the use of an equiangular-spaced beam arrangement necessitates choosing a starting gantry angle from

which the remaining equiangular-spaced gantry angles are defined. A direct posterior [3-6, 8] or anterior [2, 9] beam is commonly used as the starting gantry angle and the question arises of whether this choice affects the plan quality, and if so, is a posterior or anterior beam the best starting gantry angle?

The impetus for the use of coplanar equiangular-spaced beam arrangements for IMRT originated from several investigations employing various target geometries [7, 10, 11]. Bortfeld and Schlegel [10] demonstrated that, theoretically, the optimal beam configuration with more than three beams tends to be an even distribution over an angular range of 0° to 360° in gantry angle. The rationale for this was that a more even distribution results in a smaller burden on the normal tissue surrounding the target. These authors also demonstrated that as the number of beams increases, the dose distribution becomes less dependent on beam orientation. Söderström and Brahme [11] concluded that if a large number of beam angles ($\geq$5) are used, particularly when the tumor is deep seated, it is often sufficient to select equiangular-spaced beam angles to assure a good treatment outcome. Stein *et al.* [7] investigated the minimum number of equiangular-spaced coplanar beams required to obtain an optimal treatment plan at different dose levels (70, 76, and 81 Gy) in a prostate IMRT dose escalation study. These authors found that seven equiangular-spaced beams were sufficient for the 81 Gy prescription. However, with more than five equiangular-spaced beams, significant improvements in rectal sparing could only be achieved in the neighborhood of 60 Gy for all prescription dose levels.

Although coplanar equiangular-spaced (or nearly equiangular-spaced) beam arrangements are common for prostate IMRT, to date there has been no scientific investigation of the selection of these beam angles. Much work has been done on general optimization of the selection of beam angles in IMRT [12-19]. However, the computationally intensive nature of these optimization approaches has so far given rise to clinically infeasible computation times (0.5 to >10 hours) per patient. Therefore, none of these methods have the potential for immediate clinical impact and furthermore these algorithms are only available at a handful of academic institutions. There has been no exhaustive study conducted to investigate whether improvements in plan quality can be achieved by making an intelligent choice of starting gantry angle, as well as the number of beams, using the clinically common equiangular-spaced approach. In this chapter, the effect of starting gantry angle is investigated using 5 and 7 equiangular-spaced coplanar beam arrangements at all possible starting gantry angles in 5° increments.

2.2 Methods and Materials

2.2.1 IMRT Treatment Plans

Ten patients with localized prostate cancer treated in the supine position from October 2004 to January 2006 at CancerCare Manitoba according to the Radiation Therapy Oncology Group (RTOG) 0126 protocol were selected for this retrospective study. As specified by the protocol, the CTV included the prostate and proximal bilateral

seminal vesicles. The 10 patient cohort provided a broad range of PTV (166 ± 37 cc), rectal (77 ± 26 cc), and bladder (221 ± 73 cc) volumes.

In this study, the Arm 2 prescription (79.2 Gy in 44 fractions) of the protocol using IMRT with 5 and 7 equiangular-spaced beam arrangements was applied. The starting gantry angles of 0°, 72°, 144°, 216°, 288° (5 beams) and 0°, 51°, 102°, 153°, 204°, 255°, 306° (7 beams) were incremented by 5° until the starting beam reached the initial angular position of the second beam, resulting in 15 (5 beams) and 11 (7 beams) plans per patient; a total of 260 plans for the 10 patient cohort. All IMRT plans were generated in Pinnacle^3 version 7 (Philips Radiation Oncology Systems, Milpitas, CA, USA) using direct machine parameter optimization (DMPO) with 6 MV photon beams and static multileaf collimator (MLC) delivery. The 6 MV photon energy is used clinically to minimize photoneutron production in the head of the linear accelerator. The DMPO method in Pinnacle^3, based upon direct aperture optimization [20], includes the MLC positions and segment weights as parameters of the optimization [21].

The purpose of this investigation was to examine the variation in plan quality as a function of starting gantry angle given that the PTV coverage consistently satisfies the RTOG 0126 protocol requirements for all plans. Therefore, we ensured that the percentage volume of the PTV receiving the prescription dose (V 79.2 Gy) was at least 98 % for all plans, which represents 'no variation' in the protocol. In this way, the target coverage remained a constant for all plans and the variation in normal tissue dose metrics was isolated. It is useful to note that the same set of dose objectives, to be satisfied by the IMRT optimization, were used for all plans. These objectives ensured 98% PTV

coverage, satisfied all bladder dose-volume tolerances (as specified in the protocol), ensured femoral maximum dose below 54 Gy (not specified in the protocol), and a penile bulb mean dose of less than 52.5 Gy (optional in the protocol) for all plans. However, this recipe did not satisfy rectal dose-volume tolerances for all plans. It was found that the use of more aggressive rectal dose objectives (satisfying rectal dose-volume tolerances for all plans) would compromise PTV coverage for some plans, producing a 'minor variation' (95%-98% PTV coverage), or a 'major variation' (< 95% PTV coverage). This would then produce a situation of inconsistent PTV coverage across the 260 plans and it would therefore be meaningless to compare variations in plan quality with no consistent variable from plan to plan. Hence, dose objectives were used which would, as a priority, ensure consistent 98% PTV coverage as the control variable for all plans. This highlights the fundamental principle behind our study: given consistent target coverage, how does the dose to normal tissues vary with starting gantry angle of equiangular-spaced coplanar beams?

The variation in several bladder and rectum metrics as a function of starting gantry angle was investigated. These metrics are based on those of the RTOG 0126 protocol. For the rectum these metrics include: V 75 Gy < 15%, V 70 Gy < 25%, V 65 Gy < 35%, and V 60 Gy < 50%. For the bladder: V 80 Gy < 15%, V 75 Gy < 25%, V 70 Gy < 35%, and V 65 Gy < 50%.

2.2.2 Statistical Analysis

The coefficient of variation (C_{var}), defined as the ratio of the standard deviation to the mean, and the range of variation (R_{var}), defined as the difference between the maximum value and the minimum value, were used to quantify the magnitude of variation in the metrics with starting gantry angle. The similarity in the pattern of variation with starting gantry angle over the 10 patient cohort for each metric was assessed by performing a statistical normalization of the data called the Z-transform $[(x_i - \bar{x})/\sigma]$, where x_i is the data value, i.e. the dose metric at starting gantry angle index i, $\bar{x}$ is the mean, and σ is the standard deviation. To test the statistical significance for the differences of these metrics as a function of starting gantry angle, a two factor (patient and starting gantry angle) analysis of variance was used for the 10 patient cohort. To test the statistical significance of the differences between 5 and 7 equiangular-spaced beams, a paired *t*-test was used. A p value less than 0.05 was considered to be statistically significant (i.e. not due to chance alone) and all p values were from two-sided tests.

2.3 Results

2.3.1 Five Equiangular-spaced Beams

Figure 2.1 illustrates the PTV, bladder, and rectum dose-volume histograms (DVH), with 5 equiangular-spaced beams, for all 15 IMRT plans of a typical prostate patient. The PTV mean dose and PTV maximum dose averaged over starting gantry angle

for the 10 patient cohort were 80.7 $\pm$0.3 Gy and 81.8 $\pm$0.3 Gy, respectively. The variation in rectal V 75 Gy, V 70 Gy, V 65 Gy, and V 60 Gy as a function of starting gantry angle for all 10 patients was statistically significant ($p < 0.001$).

Figure 2.1: PTV, bladder, and rectum dose-volume histograms, with 5 equiangular-spaced beams, for all 15 IMRT plans (starting gantry angles) of a typical prostate patient (patient 9).

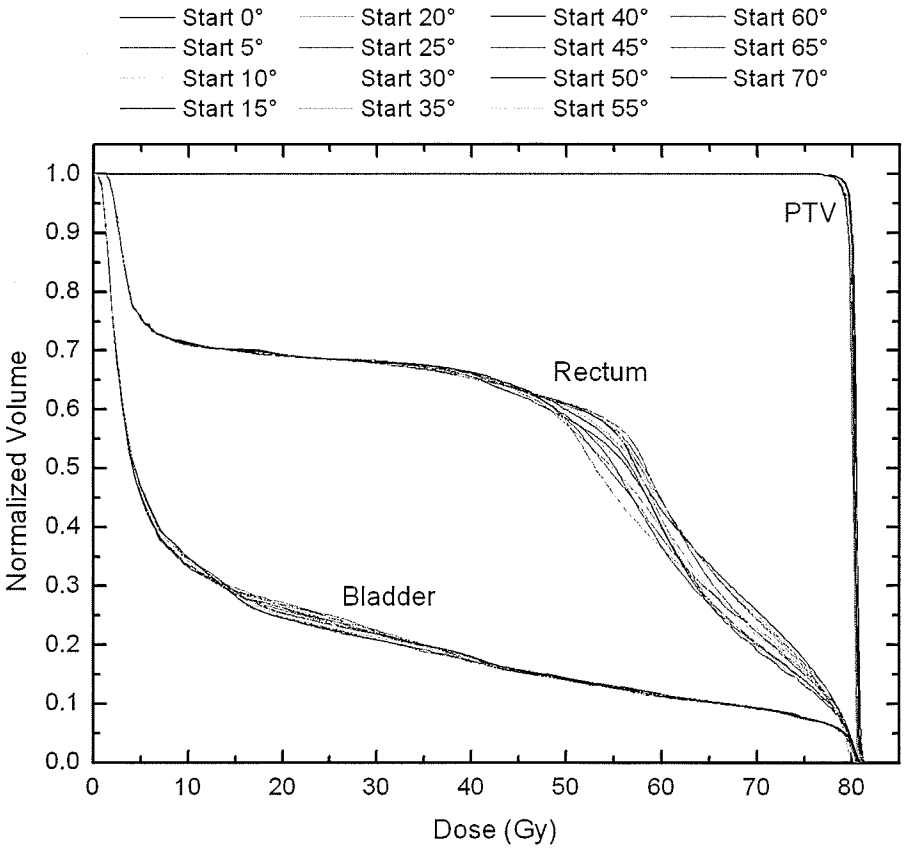

A characteristic 'W' pattern (with two separate minima centered near 20° and 50°) observed in the rectal V 75 Gy and V 70 Gy is illustrated in Figure 2.2. By calculating the average rectal V 75 Gy and performing a statistical normalization (Z-transform) with 95% confidence interval for the 10 patient cohort, the similarity in 'W' pattern indicated a class solution (Figure 2.3). A class solution was also found for the rectal V 70 Gy. As indicated in Table 2.1, the average range of variation (R_{var}) with starting gantry angle for the 10 patient cohort was 3.2 ± 0.8 % and 4.8 ± 1.1 % in the rectal V 75 Gy and V 70 Gy, respectively. The average differences in rectal V 75 Gy and V 70 Gy between a starting gantry angle of 0° and the class solution optimal starting gantry angle of 20° for the 10 patient cohort were 2.1 ± 0.9 % and 3.4 ± 1.6 %, respectively (Table 2.1). The rectal V 65 Gy also demonstrated a 'W' pattern, however, the central maxima (near 35°) was reduced compared to the higher dose metrics. In contrast, the rectal V 60 Gy demonstrated a different characteristic pattern ('V' shaped) with a minimum centered near 30°. However, these low dose rectal metric variations were not as useful as their high dose counterparts because it was much easier for the IMRT optimization to satisfy the low dose rectal objectives. On the other hand, the variation in bladder V 80 Gy, V 75 Gy, V 70 Gy, and V 65 Gy as a function of starting gantry angle for all 10 patients was not statistically significant ($p = 0.682$, $p = 0.782$, $p = 0.924$, $p = 0.953$, respectively).

Figure 2.2: Rectal V 75 Gy (top) and V 70 Gy (bottom) as a function of starting gantry angle using 5 equiangular-spaced beams. The variation with starting gantry angle in V 75 Gy and V 70 Gy was statistically significant ($p < 0.001$). A characteristic 'W' pattern with two minima, corresponding to optimal starting gantry angles for rectal sparing, was apparent for the 10 patient cohort.

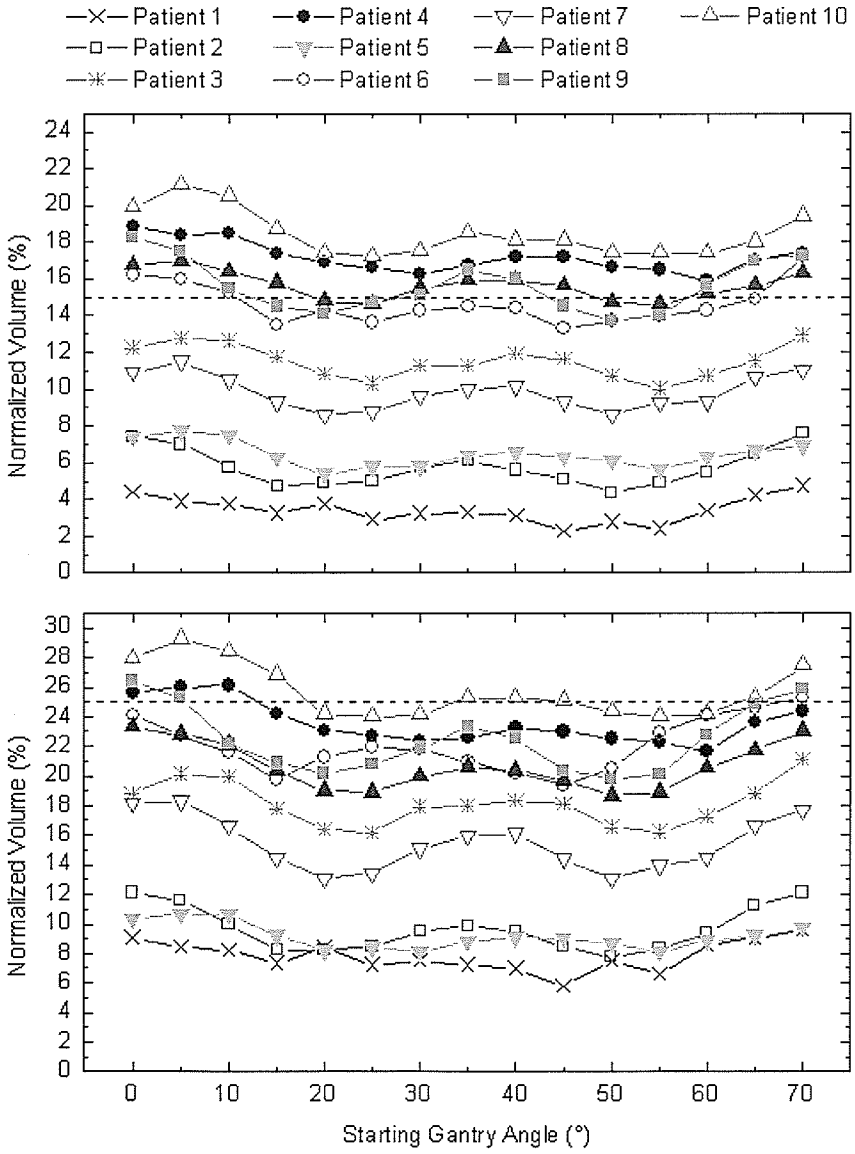

Figure 2.3: Statistically normalized (Z-transform) rectal V 75 Gy (top) with 95% confidence interval on the mean (bottom) for the 10 patient cohort. The strong 'W' pattern indicated a class solution.

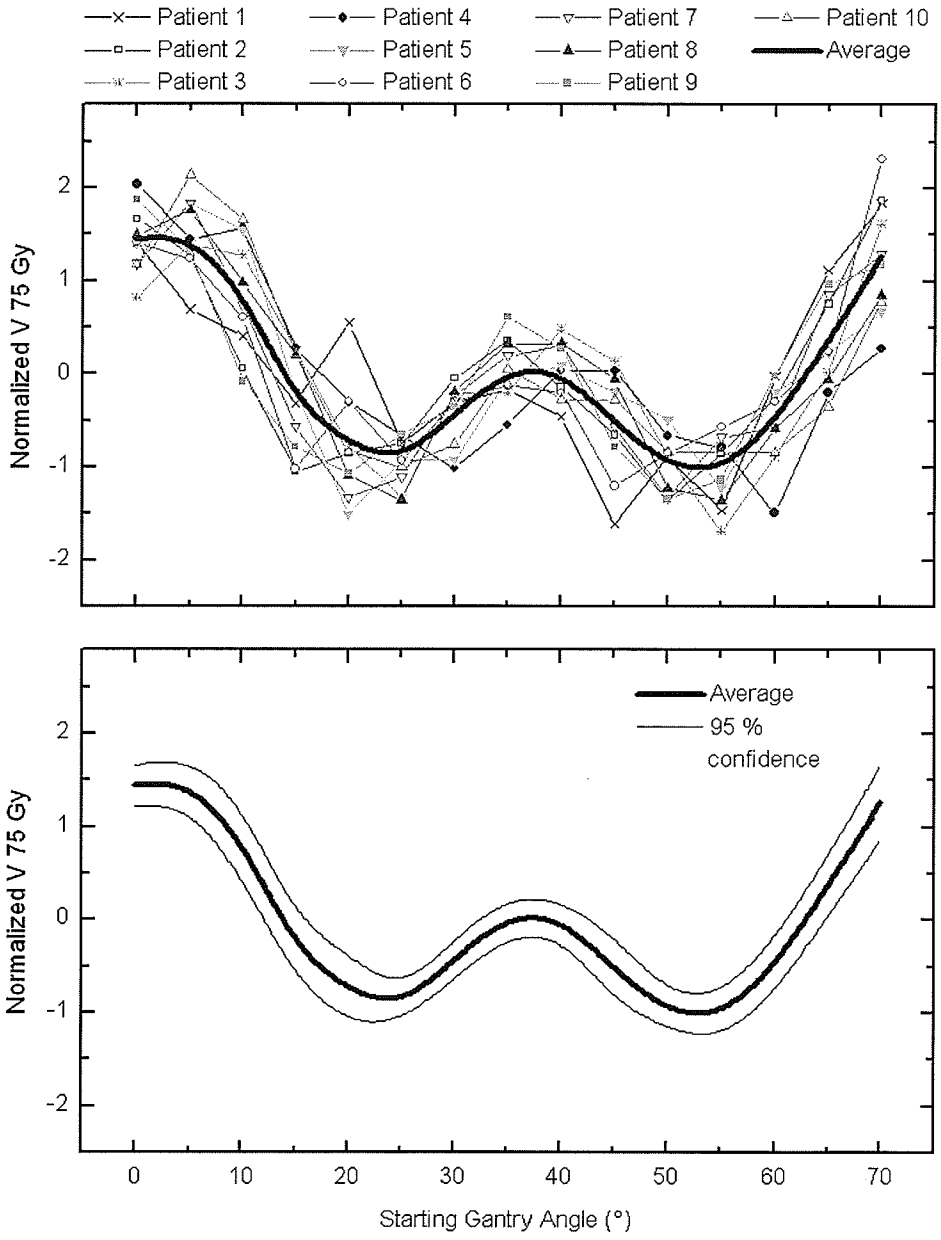

Table 2.1: Rectal V 75 Gy and V 70 Gy (at a starting gantry angle of 0° and 20°) and the range of variation (R_{var}) for the 10 patient cohort using 5 and 7 equiangular-spaced beams. *Diff (0°/20°)* is the difference in the metric between 0° and 20° using 5 equiangular-spaced beams. *Diff (0°/0°)* is the difference in the metric between 0° using 5 equiangular-spaced beams and 0° using 7 equiangular-spaced beams. *Diff (20°/0°)* is the difference in the metric between 20° using 5 equiangular-spaced beams (class solution) and 0° using 7 equiangular-spaced beams. A negative value in *Diff (20°/0°)* indicates that the metric at 20° using 5 equiangular-spaced beams is lower compared to it's value at 0° using 7 equiangular-spaced beams.

	Rectal V 75 Gy (%)								Rectal V 70 Gy (%)							
	5 Beams				7 Beams				5 Beams				7 Beams			
Pat	R_{var}	At 0°	At 20°	Diff (0°/20°)	R_{var}	At 0°	Diff (0°/0°)	Diff (20°/0°)	R_{var}	At 0°	At 20°	Diff (0°/20°)	R_{var}	At 0°	Diff (0°/0°)	Diff (20°/0°)
1	2.4	4.4	3.8	0.6	0.8	2.0	2.4	1.8	3.8	9.1	8.4	0.7	1.4	5.5	3.6	2.9
2	3.2	7.4	4.9	2.5	0.8	5.2	2.2	-0.3	4.3	12.1	8.3	3.8	0.9	8.6	3.5	-0.3
3	2.9	12.2	10.8	1.4	1.5	9.6	2.6	1.2	5.0	18.8	16.4	2.4	2.5	14.7	4.1	1.7
4	3.0	18.9	16.9	2.0	0.6	15.6	3.3	1.3	4.4	25.6	23.1	2.5	1.3	21.5	4.1	1.6
5	2.3	7.4	5.4	2.0	0.6	5.5	1.9	-0.1	2.6	10.3	8.2	2.1	0.9	8.1	2.2	0.1
6	3.9	16.2	14.3	1.9	0.9	11.5	4.7	2.8	5.8	24.1	21.3	2.8	1.7	17.7	6.4	3.6
7	2.9	10.9	8.6	2.3	0.5	9.0	1.9	-0.4	5.2	18.1	13.1	5.0	1.3	14.0	4.1	-0.9
8	2.4	16.8	14.8	2.0	1.1	13.5	3.3	1.3	4.6	23.3	19.0	4.3	1.5	18.3	5.0	0.7
9	4.6	18.3	14.1	4.2	1.0	13.6	4.7	0.5	6.6	26.4	20.2	6.2	1.5	20.1	6.3	0.1
10	3.9	19.9	17.4	2.5	0.9	17.5	2.4	-0.1	5.2	27.9	24.2	3.7	0.9	23.9	4.0	0.3
Mean	3.2			2.1	0.9		2.9	1.0	4.8			3.4	1.4		4.3	1.0
S.D.	0.8			0.9	0.3		1.0	1.1	1.1			1.6	0.5		1.3	1.4

2.3.2 Seven Equiangular-spaced Beams

Figure 2.4 illustrates the PTV, bladder, and rectum dose-volume histograms (DVH), with 7 equiangular-spaced beams, for all 11 IMRT plans of a typical prostate patient. The PTV mean dose and PTV maximum dose averaged over starting gantry angle

for the 10 patient cohort were 80.7 ± 0.3 Gy and 81.8 ± 0.4 Gy, respectively. In contrast to the 5 beam arrangement, the variation in rectal V 75 Gy as a function of starting gantry angle for all 10 patients was not statistically significant (p = 0.125). However, the variation in rectal V 70 Gy continued to demonstrate statistical significance ($p < 0.001$) albeit with the disappearance of the 'W' pattern (Figure 2.5).

Figure 2.4: PTV, bladder, and rectum dose-volume histograms, with 7 equiangular-spaced beams, for all 11 IMRT plans (starting gantry angles) of a typical prostate patient (patient 9).

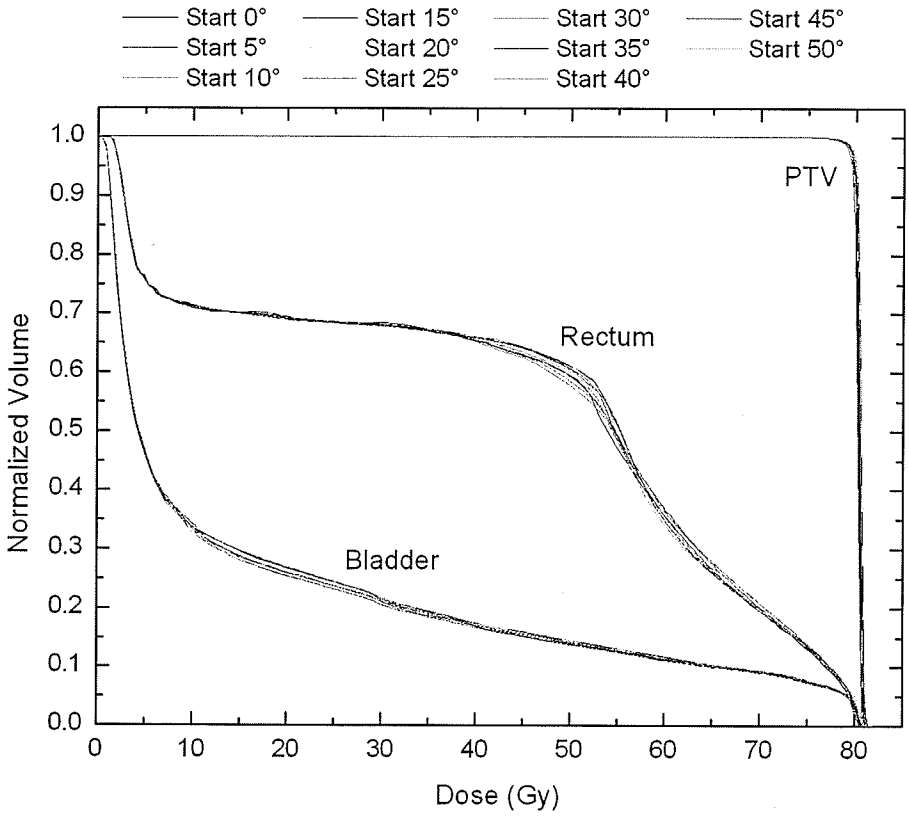

As indicated in Table 2.1, the average range of variation (R_{var}) with starting gantry angle for the 10 patient cohort was 0.9 ± 0.3 % and 1.4 ± 0.5 % in the rectal V 75 Gy and V 70 Gy, respectively. The variations in the rectal V 65 Gy and V 60 Gy also continued to show statistical significance ($p < 0.001$, $p = 0.009$, respectively). As with 5 beams, the variation in bladder V 80 Gy as a function of starting gantry angle was not statistically significant ($p = 0.493$). On the other hand, the variation in bladder V 75 Gy, V 70 Gy, and V 65 Gy, was, unlike with 5 beams, statistically significant ($p = 0.034$, $p = 0.003$, $p = 0.005$, respectively). However, there was very little dosimetric variation with starting gantry angle in the bladder metrics ($R_{var} < 1.5\%$).

Figure 2.5: Rectal V 75 Gy (top) and V 70 Gy (bottom) as a function of starting gantry angle using 7 equiangular-spaced beams. The variation in rectal V 75 Gy for the 10 patient cohort was not statistically significant (p = 0.125). However, the variation in rectal V 70 Gy demonstrated statistical significance (p < 0.001) albeit with the disappearance of the 'W' pattern and little dosimetric variation with starting gantry angle.

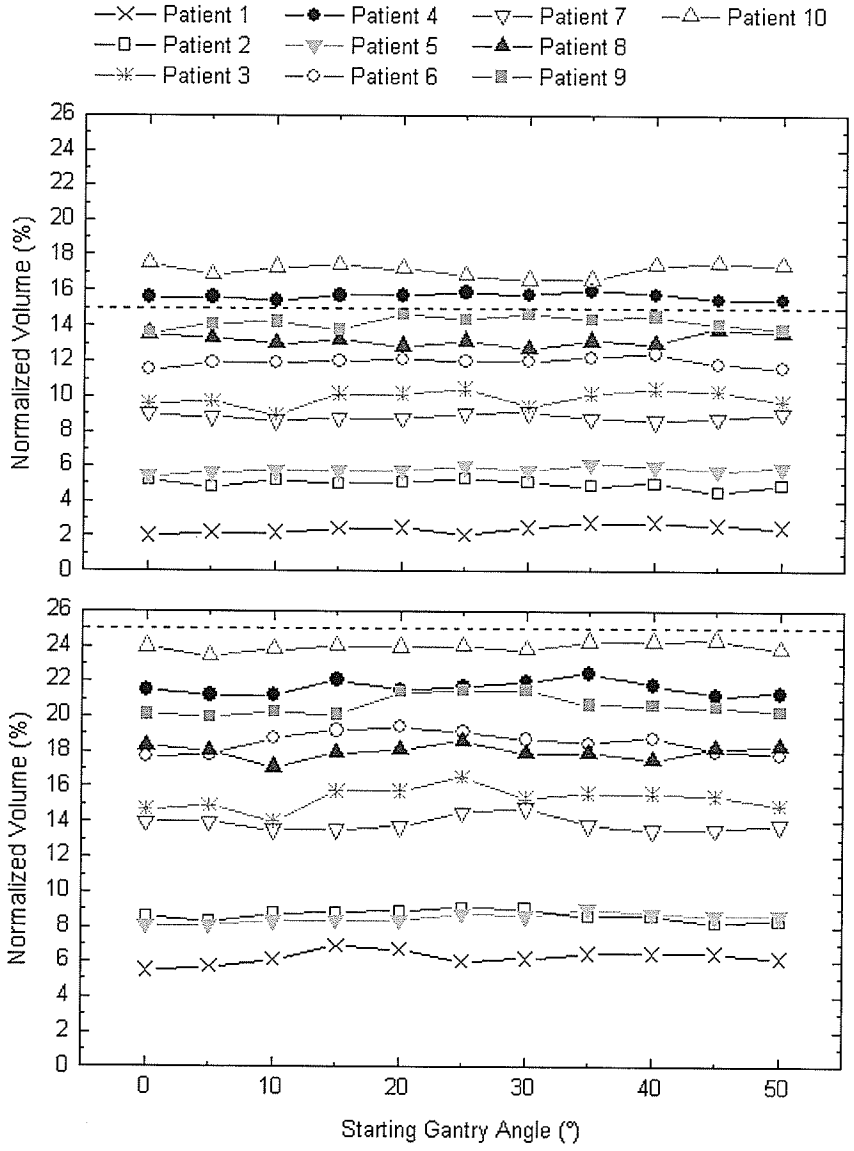

2.3.3 Comparison between Five and Seven Equiangular-spaced Beams

The average and minimum values in each metric as a function of starting gantry angle were calculated for each patient for both 5 and 7 equiangular-spaced beams. To test for statistically significant differences between 5 and 7 equiangular-spaced beams, a p value was calculated using the average metric values (p_{avg}) and the minimum metric values (p_{min}) for the patient cohort. The median coefficient of variation (C_{var}) for the patient cohort was also calculated to quantify the magnitude of variation in each metric between 5 and 7 equiangular-spaced beams. The p_{avg} demonstrated statistically significant differences in the average rectal metrics but not in the average bladder metrics between 5 and 7 equiangular-spaced beams (Table 2.2). However, the differences in minima for the rectal metrics (as indicated by p_{min}) were statistically insignificant between 5 and 7 equiangular-spaced beams. The 10 patient cohort also demonstrated a smaller R_{var} (Table 2.1) and a smaller median C_{var} (Table 2.2) for the rectal metrics using 7 equiangular-spaced beams. As expected, there were improvements in the rectal V 75 Gy and V 70 Gy with equivalent bladder sparing by using 7 instead of 5 equiangular-spaced beams observed using a direct anterior beam (0°) as the starting gantry angle for all patients with an average improvement of 2.9 ± 1.0 % and 4.3 ± 1.3 % in rectal V 75Gy and V 70 Gy, respectively (Table 2.1). Most importantly, Table 2.1 shows that nearly equivalent rectal V 75 Gy and V 70 Gy can be achieved for most patients by using 5 equiangular-spaced beams at an optimal starting gantry angle of 20° (class solution) compared to 7 equiangular-spaced beams at a starting gantry angle of 0° (average

differences in rectal V 75 Gy and V 70 Gy between the class solution 20° (5 beams) and 0° (7 beams) are only 1.0 ± 1.1 % and 1.0 ± 1.4 %, respectively).

Table 2.2: Statistical comparison between 5 and 7 equiangular-spaced beams for rectum and bladder metrics.

	p_{avg}	Median C_{var} (%)		p_{min}
		(5 B)	(7 B)	
Rectal V 75 Gy	0.002	8.4	2.5	0.458
Rectal V 70 Gy	0.001	8.9	3.1	0.796
Rectal V 65 Gy	0.001	8.6	3.7	0.109
Rectal V 60 Gy	< 0.001	8.0	3.8	0.802
Bladder V 80 Gy	1.000	8.3	5.8	0.672
Bladder V 75 Gy	0.999	2.2	1.6	1.000
Bladder V 70 Gy	0.388	1.8	1.2	1.000
Bladder V 65 Gy	0.150	1.7	1.2	1.000

2.4 Discussion

It has been demonstrated that the choice of starting gantry angle in a 5 beam equiangular-spaced beam arrangement is important in order to satisfy the RTOG 0126 protocol metrics for the rectum. The characteristic 'W' pattern observed in the rectal V 75 Gy and V 70 Gy as a function of starting gantry angle is significant since it indicates

two minima corresponding to optimal starting gantry angles for rectal sparing. This pattern is particularly important for Patients 8 and 9 with respect to satisfying the rectal V 75 Gy metric. For these patients, the rectal V 75 Gy is only below the 15% tolerance in a small region centered on two optimal starting gantry angles (minima in V 75 Gy). In fact, Patient 9 experiences a nearly 5% variation in rectal V 75 Gy from a starting gantry angle of 0° (maximum V 75 Gy) to 50° (minimum V 75 Gy). There is clinical evidence of reduced grade 2 rectal toxicity if the rectal V 75 Gy and V 70 Gy are below 15% and 25%, respectively [22-25]. The 'W' pattern in rectal V 75 Gy and V 70 Gy is apparent for all patients except Patient 1. This patient presents a uniquely distinct pattern with a much less pronounced 'W' pattern. A possible explanation for this can be attributed to the small rectal volume of 42 cc.

The symmetrical 'W' pattern variation in rectal V 75 Gy and V 70 Gy (with two minima near 20° and 50°) is due to the geometrical symmetry of the pelvic region about an anterior-posterior axis. Variations away from perfect symmetry are due to small asymmetries in patient geometry. Note that a starting gantry angle of 20° results in a nearly exact left lateral field, while a starting gantry angle of 50° results in a nearly exact right lateral field. The presence of this lateral field may assist in reducing the rectal high dose metrics, and will be discussed in subsequent chapters.

In contrast, the insignificant differences in the bladder metrics as a function of starting gantry angle with 5 equiangular-spaced beams lead us to the conclusion that the choice of starting gantry angle matters for rectal sparing but has no consequence for the

bladder. An explanation for the different responses with starting gantry angle observed between the rectum and bladder is possibly due to the volume of each organ in the primary beam path. Specifically, a much smaller bladder volume is exposed to the primary beams compared to the rectum, therefore, dose-volume variations will be magnified over the larger rectal volume. It is important to note that a starting direct anterior beam (0°), with 5 equiangular-spaced beams, is nearly the worst starting gantry angle choice for rectal sparing. A starting direct posterior beam (starting gantry angle of 36°), as used by Zelefsky *et al.*, is also inferior for rectal sparing since the rectal V 75 Gy and V 70 Gy class solutions demonstrate a local maxima in the 'W' pattern. An immediate clinical implication is that the two most commonly utilized equiangular-spaced (or nearly equiangular-spaced) clinical beam arrangements are not optimal and further rectal sparing (in high dose metrics) could be achieved by implementation of our class solution. Stein *et al.* concluded that beams coming from the direction of the rectum are preferable since they allow greater control over dose distributions in regions close to the sensitive structure [7]. Our results partially support this conclusion but provide further refinement for the specific case of 5 equiangular-spaced beams; optimal rectal sparing will not be achieved while incorporating a direct posterior beam. Instead, an optimal starting gantry angle near 20° or 50° will involve a posterior oblique beam approximately 15° offset from a direct posterior beam (gantry 164° or 194°).

The use of 7 equiangular-spaced beams clearly resulted in the dose distribution becoming less dependent on beam orientation. This was demonstrated by the disappearance of the characteristic 'W' pattern in rectal V 75 Gy (resulting in statistically

insignificant variations) and by the reduction of the C_{var} for all metrics. Even though the rectal V 70 Gy, V 65 Gy, and V 60 Gy continued to show statistically significant variations with 7 beams, unlike with 5 beams, there was little dosimetric variation (R_{var} typically < 2.5 %). These results support the findings of Stein *et al.* [7], demonstrating that as the number of equiangular-spaced beams is increased, the rectal dose dependence on beam orientation diminishes. The statistically significant variations in bladder V 75 Gy, V 70 Gy, and V 65 Gy also showed little dosimetric variation (R_{var} typically < 1.5 %). Therefore, one can conclude that by using 7 equiangular-spaced, coplanar beams, the choice of starting gantry angle is irrelevant for rectal and bladder sparing. It was also clear that with the use of 7 instead of 5 equiangular-spaced beams, reductions in the rectal metrics could be achieved at a starting gantry angle of 0°. For instance, the rectal V 75 Gy < 15% could only be satisfied in patients 6, 8, and 9 with the use of 7 beams at a starting gantry angle of 0° and the rectal V 70 Gy < 25% could only be satisfied in patients 4, 9, and 10 with the use of 7 beams at a starting gantry of 0°.

Of particular interest is the fact that the differences in minima for the rectal and bladder metrics were statistically insignificant between 5 and 7 equiangular-spaced beams. The implication of this is that with an intelligent selection of starting gantry angle using 5 equiangular-spaced beams, achievable plan quality can be equivalent to plans using 7 equiangular-spaced beams. This was demonstrated by the nearly equivalent rectal V 75 Gy and V 70 Gy for most patients at an optimal starting gantry angle of 20° (class solution) using 5 equiangular-spaced beams compared to using 7 equiangular-spaced beams at a starting gantry angle of 0°. This is an important result in that it provides

further justification for the use of the *fewest number of beams possible* since a larger number of beams may have the undesirable consequence of spreading low doses to larger volumes of normal tissues [26, 27], increase treatment delivery time, quality assurance efforts, and the probability of patient movement during delivery [28]. Patients 1, 3, 4, and 6 experienced larger improvements in rectal V 75 Gy and V 70 Gy by using 7 equiangular-spaced beams starting at 0° compared to the class solution optimal starting gantry angle (20° using 5 equiangular-spaced beams). This represents a drawback of using a class solution approach in that patient geometric variability produces a $\pm 5°$ variation in the location of the minimum in rectal V 75 Gy and V 70 Gy. Therefore, the use of a class solution may not produce the full dosimetric advantage in rectal sparing for all patients. Chapter 3 presents a beam orientation optimization algorithm to customize optimal equiangular-spaced beams for a particular patient. Nonetheless, a class solution ultimately has the distinct advantage of being simple to implement.

This study has only exhaustively searched a small subspace of the beam configuration space. However, this subspace (equiangular-spaced beam arrangements) is commonly used clinically for IMRT delivery and, therefore, an important region to investigate and understand. This chapter has statistically proven on a group of patient data that a class solution exists using 5 equiangular-spaced beams for prostate IMRT and has demonstrated that there are some beam configurations that are better than others (i.e. optimal), improving the rectal high dose metrics (V 75 Gy, V 70 Gy) while maintaining PTV coverage. The conclusions in this study are easy to implement in the clinic immediately without having to rely on computationally intensive beam orientation

optimization algorithms. This work has provided direct evidence for clinics using common equiangular-spaced beam angles to change their starting gantry angle to improve rectal sparing.

2.5 Conclusions

This chapter has demonstrated that the choice of starting gantry angle in a 5 equiangular-spaced beam arrangement for the treatment of prostate cancer under the RTOG 0126 protocol is important. Since a class solution was proven for the clinically common 5 equiangular-spaced beam approach, these results can be immediately applied within the clinical setting unlike many other beam orientation optimization methods which demonstrate clinically infeasible computation times. An intelligent choice of starting gantry angle near 20° or 50° facilitates optimal rectal sparing with minima in the V 75 Gy and V 70 Gy. In fact, the use of starting gantry angle optimization for 5 equiangular-spaced beams can produce plans that achieve equivalent rectal sparing to plans using 7 equiangular-spaced beams. However, the starting gantry angle with 5 equiangular-spaced beams was found to be irrelevant for the bladder, with no adverse nor beneficial effects. The use of 7 equiangular-spaced beams has the advantage of producing very little dosimetric variation in the rectal and bladder metrics as a function of starting gantry angle, thus eliminating the need for starting gantry angle optimization. However, the drawback of using 7 beams is the increased treatment delivery time which is an important consideration for clinics faced with challenges in patient throughput. This work

will ultimately assist the clinician in making an informed decision regarding the use of 5 or 7 equiangular-spaced beams for the treatment of prostate cancer.

2.6 Bibliography

1. De Meerleer, G.O., L.A. Vakaet, et al., *Radiotherapy of prostate cancer with or without intensity modulated beams: a planning comparison.* Int J Radiat Oncol Biol Phys, 2000. **47**(3): p. 639-48.
2. Nutting, C.M., D.J. Convery, et al., *Reduction of small and large bowel irradiation using an optimized intensity-modulated pelvic radiotherapy technique in patients with prostate cancer.* Int J Radiat Oncol Biol Phys, 2000. **48**(3): p. 649-56.
3. Zelefsky, M.J., Z. Fuks, et al., *Clinical experience with intensity modulated radiation therapy (IMRT) in prostate cancer.* Radiother Oncol, 2000. **55**(3): p. 241-9.
4. Zelefsky, M.J., Z. Fuks, et al., *High dose radiation delivered by intensity modulated conformal radiotherapy improves the outcome of localized prostate cancer.* J Urol, 2001. **166**(3): p. 876-81.
5. Zelefsky, M.J., Z. Fuks, et al., *High-dose intensity modulated radiation therapy for prostate cancer: early toxicity and biochemical outcome in 772 patients.* Int J Radiat Oncol Biol Phys, 2002. **53**(5): p. 1111-6.
6. Zelefsky, M.J., Z. Fuks, et al., *Intensity-modulated radiation therapy for prostate cancer.* Semin Radiat Oncol, 2002. **12**(3): p. 229-37.

7. Stein, J., R. Mohan, et al., *Number and orientations of beams in intensity-modulated radiation treatments.* Med Phys, 1997. **24**(2): p. 149-60.

8. Burman, C.M., M.J. Zelefsky, et al., *Treatment Planning, Dose Delivery, and Outcome of IMRT for Localized Prostate Cancer*, in *A Practical Guide to Intensity-Modulated Radiation Therapy*, Z. Fuks, S.A. Leibel, and C.C. Ling, Editors. 2003, Medical Physics Publishing: Madison, Wisconsin. p. 169-190.

9. Price, R.A., G.E. Hanks, et al., *Advantages of using noncoplanar vs. axial beam arrangements when treating prostate cancer with intensity-modulated radiation therapy and the step-and-shoot delivery method.* Int J Radiat Oncol Biol Phys, 2002. **53**(1): p. 236-43.

10. Bortfeld, T. and W. Schlegel, *Optimization of beam orientations in radiation therapy: some theoretical considerations.* Phys Med Biol, 1993. **38**(2): p. 291-304.

11. Soderstrom, S. and A. Brahme, *Which is the most suitable number of photon beam portals in coplanar radiation therapy?* Int J Radiat Oncol Biol Phys, 1995. **33**(1): p. 151-9.

12. Das, S., T. Cullip, et al., *Beam orientation selection for intensity-modulated radiation therapy based on target equivalent uniform dose maximization.* Int J Radiat Oncol Biol Phys, 2003. **55**(1): p. 215-24.

13. Djajaputra, D., Q. Wu, et al., *Algorithm and performance of a clinical IMRT beam-angle optimization system.* Phys Med Biol, 2003. **48**(19): p. 3191-212.

14. Hou, Q., J. Wang, et al., *Beam orientation optimization for IMRT by a hybrid method of the genetic algorithm and the simulated dynamics.* Med Phys, 2003. **30**(9): p. 2360-7.

15. Meedt, G., M. Alber, et al., *Non-coplanar beam direction optimization for intensity-modulated radiotherapy.* Phys Med Biol, 2003. **48**(18): p. 2999-3019.

16. Pugachev, A., J.G. Li, et al., *Role of beam orientation optimization in intensity-modulated radiation therapy.* Int J Radiat Oncol Biol Phys, 2001. **50**(2): p. 551-60.

17. Pugachev, A. and L. Xing, *Incorporating prior knowledge into beam orientation optimization in IMRT.* Int J Radiat Oncol Biol Phys, 2002. **54**(5): p. 1565-74.

18. Rowbottom, C.G., C.M. Nutting, et al., *Beam-orientation optimization of intensity-modulated radiotherapy: clinical application to parotid gland tumours.* Radiother Oncol, 2001. **59**(2): p. 169-77.

19. Wang, X., X. Zhang, et al., *Effectiveness of noncoplanar IMRT planning using a parallelized multiresolution beam angle optimization method for paranasal sinus carcinoma.* Int J Radiat Oncol Biol Phys, 2005. **63**(2): p. 594-601.

20. Shepard, D.M., M.A. Earl, et al., *Direct aperture optimization: a turnkey solution for step-and-shoot IMRT.* Med Phys, 2002. **29**(6): p. 1007-18.

21. Siebers, J.V., M. Lauterbach, et al., *Incorporating multi-leaf collimator leaf sequencing into iterative IMRT optimization.* Med Phys, 2002. **29**(6): p. 952-9.

22. Fiorino, C., G. Sanguineti, et al., *Rectal dose-volume constraints in high-dose radiotherapy of localized prostate cancer.* Int J Radiat Oncol Biol Phys, 2003. **57**(4): p. 953-62.

23. Huang, E.H., A. Pollack, et al., *Late rectal toxicity: dose-volume effects of conformal radiotherapy for prostate cancer.* Int J Radiat Oncol Biol Phys, 2002. **54**(5): p. 1314-21.

24. Boersma, L.J., M. van den Brink, et al., *Estimation of the incidence of late bladder and rectum complications after high-dose (70-78 GY) conformal radiotherapy for prostate cancer, using dose-volume histograms.* Int J Radiat Oncol Biol Phys, 1998. **41**(1): p. 83-92.

25. Jackson, A., M.W. Skwarchuk, et al., *Late rectal bleeding after conformal radiotherapy of prostate cancer. II. Volume effects and dose-volume histograms.* Int J Radiat Oncol Biol Phys, 2001. **49**(3): p. 685-98.

26. Liu, H.H., M. Jauregui, et al., *Beam angle optimization and reduction for intensity-modulated radiation therapy of non-small-cell lung cancers.* Int J Radiat Oncol Biol Phys, 2006. **65**(2): p. 561-72.

27. Wang, X., X. Zhang, et al., *Development of methods for beam angle optimization for IMRT using an accelerated exhaustive search strategy.* Int J Radiat Oncol Biol Phys, 2004. **60**(4): p. 1325-37.

28. Kim, S., H.C. Akpati, et al., *An immobilization system for claustrophobic patients in head-and-neck intensity-modulated radiation therapy.* Int J Radiat Oncol Biol Phys, 2004. **59**(5): p. 1531-9.

CHAPTER THREE: A SIMPLE GEOMETRIC ALGORITHM TO PREDICT OPTIMAL STARTING GANTRY ANGLES USING EQUIANGULAR-SPACED BEAMS FOR INTENSITY MODULATED RADIATION THERAPY OF PROSTATE CANCER

This chapter is adapted from a manuscript entitled "A Simple Geometric Algorithm to Predict Optimal Starting Gantry Angles Using Equiangular-spaced Beams for Intensity Modulated Radiation Therapy of Prostate Cancer" by Peter Potrebko, Boyd McCurdy, James Butler, Adel El-Gubtan, and Zoann Nugent, published in *Medical Physics* 34 (2007), 3951-3961.

3.1 Introduction

Intensity-modulated radiation therapy (IMRT) for the treatment of prostate, head-and-neck, and other cancers has been shown to provide dosimetric improvements over three-dimensional conformal radiotherapy (3D-CRT) and, therefore, has gained widespread clinical acceptance [1-4]. In current IMRT treatment planning, the selection of a set of suitable beam orientations is based on the experience and intuition of the planner or by a trial-and-error approach. However, manually selected beam orientations may be far from optimal especially considering the counterintuitive effects of intensity modulation [5]. A common approach has been to avoid the suboptimal placement of beams altogether by employing a relatively large number of beams, such as nine coplanar equiangular-spaced beams, so that the IMRT plan may not be sensitive to the choice of

individual beam angles. The evidence for such a strategy has come from a number of investigations employing various target geometries [5-7]. Bortfeld and Schlegel [6] demonstrated that, theoretically, the optimal beam configuration with more than three beams tends to be an even distribution over an angular range of 0° to 360° in gantry angle. The rationale for this was that a more even distribution results in a smaller burden on the normal tissue surrounding the target. These authors also demonstrated that as the number of beams increases, the dose distribution becomes less dependent on beam orientation. Söderström and Brahme [7] concluded that if a large number of beam angles ($\geq$5) are used, particularly when the tumor is deep seated, it is often sufficient to select equiangular-spaced beam angles to produce a good treatment plan. However, a larger number of beams may have the undesirable consequence of spreading low doses to larger volumes of normal tissues [8, 9]. It may also increase treatment delivery time, quality assurance efforts, and the probability of patient movement during delivery [10].

The selection of optimal beam directions with *the fewest number of beams possible* would be advantageous in IMRT. Many investigators have studied computerized beam angle optimization (BAO) methods for the automatic selection of the best beam orientations in both 3D-CRT [6, 11-23] and IMRT [5-9, 24-46]. Different methods, including exhaustive search [8, 9, 23, 27, 32, 42, 46], simulated annealing [14, 15, 20, 24, 25, 33, 36-38], genetic algorithms [11, 19, 28, 31, 39, 40], and integer programming [18, 26, 29, 43] have been used. A common approach has been to optimize an objective function (OF) incorporating dose-volume constraints with respect to the beam orientation. However, such an OF can contain multiple local minima which may lead to a

suboptimal solution if the optimization method becomes trapped in a local minimum [47]. An exhaustive search can circumvent the local minima problem but is time-consuming because of the large search space. Stochastic optimization methods such as simulated annealing and genetic algorithms are capable of escaping from local minima but also have the disadvantage of long computation times. Yang *et al.* [43] employed a faster deterministic method which used a mixed integer programming algorithm to search the solution space in a systematic manner (thereby avoiding local minima traps), however, it still required at least 30 minutes to finish the optimization. In general, the computationally intensive nature of dosimetric-based optimization approaches gives rise to clinically infeasible computation times (0.5 to >10 hours) per patient.

Only a few investigators have explored geometry-based methods in order to reduce optimization time, however, these studies were limited to 3D-CRT [11-13, 17]. In this chapter, a clinical geometric BAO algorithm for IMRT is proposed, based on minimizing beam intersection volume (BIV) within organ's-at-risk (OARs). A mathematical theory is presented which explains the correlation of BIV with dose and dose-volume metrics. The algorithm is applied to optimize coplanar, equiangular-spaced beam arrangements since these arrangements (or nearly equiangular ones) are commonly used clinically in prostate IMRT [5, 48-53]. It will be demonstrated that the BIV in the rectum is strongly correlated to the rectal high dose metrics (from Chapter 2) and, therefore, facilitates choosing an optimal starting gantry angle for rectal sparing using 5 equiangular-spaced beams.

3.2 Methods and Materials

3.2.1 Theory

A mathematical relationship between beam geometry and the dose distribution for both 3D-CRT and IMRT is presented here. Specifically, a clear link between the beam intersection volume and the dose distribution can be derived from the work of Pugachev *et al.* [37] where filtered backprojection [54] was employed to relate the dose distribution on a two-dimensional (2D) dose plane $D(x,y)$ to the one-dimensional incident dose intensity profile $I(R)$ (Figure 3.1a). For simplicity, Pugachev *et al.* assumed parallel beam geometry (fully divergent beam calculations are performed in the current work) and only considered primary beams (scattering was neglected). For N_b incident beams, with the ith beam denoted by direction θ_i, each incident beam was divided into a series of beamlets. The number of activated beamlets in an incident beam was determined by the BEV projection of the planning target area (PTA). The dose at point (x,y) was then given by

$$D(x,y) = \sum_{i=1}^{N_b} \sum_{j=1}^{N_p} I_i(R)\delta(x\cos\theta_i + y\sin\theta_i - R_j) \tag{3.1}$$

where N_p was the number of pencil beams in the ith beam, $I_i(R)$ was the dose intensity profile of the ith beam, R was the coordinate of the projection line (Figure 3.1a). The function $\delta(p)$ corresponded to the propagation of a single beamlet and was defined by

$$\delta(p) = \begin{cases} 1, & if\,|p| < \Delta R/2 \\ 0, & otherwise \end{cases} \tag{3.2}$$

where ΔR was the width of a beamlet.

Figure 3.1: a) Backprojection geometry (2D) with an arbitrary Planning Target Area (PTA). b) Case I geometry. The *i*th beam is at $\theta = 0°$, has width $2w$ (encompassing PTA), and traverses a distance $2L$ within the phantom. Assume the dose intensity profile *I(R)* is given by a 'top-hat' function. c) Case II geometry. An Organ-at-Risk (OAR) of width $2a$ lies within the beam. Assume the dose intensity profile *I(R)* is given by a 'well' function. d) Case III geometry. An OAR of width $2a$ which is offset to the side of the beam. This scenario emulates what would be seen if the beam was incident at an oblique angle relative to the Case II example. Assume the dose intensity profile *I(R)* is given by an asymmetric 'step' function.

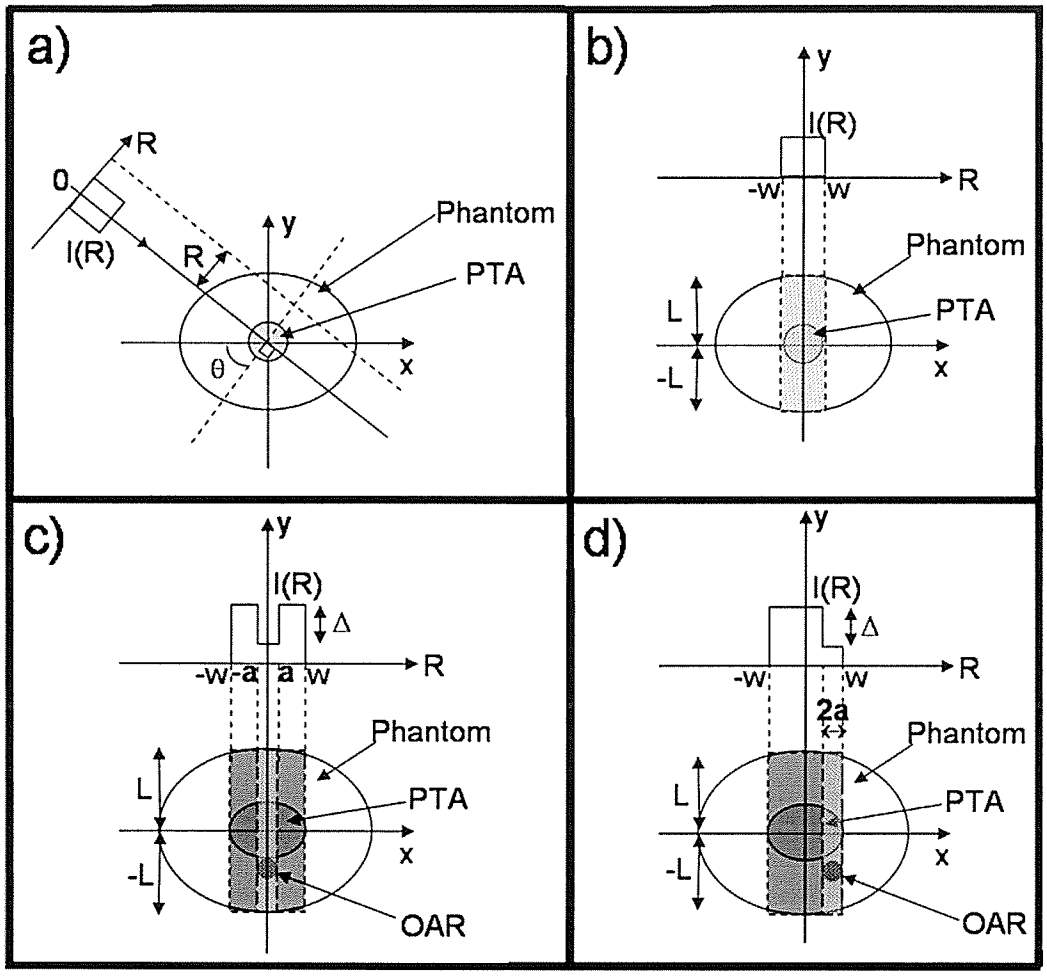

Case I (3D-CRT)

For mathematical simplicity suppose the ith beam is at $\theta_i = 0°$, has width $2w$ to encompass the PTA, and traverses a distance $2L$ within the phantom (Figure 3.1b). Assume the idealized intensity profile is given by

$$I_i(R) = \begin{cases} 1, & if\ -w \le R \le w \\ 0, & otherwise \end{cases} \tag{3.3}$$

According to Eq. (3.1), the dose distribution from the ith beam is

$$D_i(x,y) = I_i(R) \tag{3.4}$$

In this 2D example, if we wish to consider the total dose over an area of the beam rather than simply a point dose, we define a more useful quantity called the areametric dose (or area integrated dose) of the ith beam given by

$$\widetilde{D}_i = \iint D_i(x,y)dxdy = \int_{-L}^{+L}\int_{-w}^{+w} 1 \cdot dxdy = 1 \cdot 4Lw = 1 \cdot Area_i \tag{3.5}$$

Thus, we see that the areametric dose is directly proportional to the beam area weighted by the intensity profile. Note that if the integration limits were taken over an OAR area inside the beam one would conclude that the areametric dose in the OAR is proportional to the area of the OAR encompassed by the beam. The intersection area of all N_b beams of equal intensity will correspond to the area of maximum dose of the total dose distribution which is given by

$$\widetilde{D}_{\max} = \bigcap_{i=1}^{N_b} \widetilde{D}_i \propto \bigcap_{i=1}^{N_b} Area_i \tag{3.6}$$

Generalizing to three dimensions, one can in a similar manner define a volumetric dose such that the volume of maximum dose will be given by the intersection volume of all beams

$$\widetilde{D}_{\max} \propto \bigcap_{i=1}^{N_b} Volume_i \tag{3.7}$$

Case II (IMRT- OAR directly in beam path)

Suppose we have an OAR of width $2a$ in the beam (Figure 3.1c). Let Δ_i be a parameter representing an arbitrary level of intensity modulation in the beam. Assume the intensity profile is now given by

$$I_i(R) = \begin{cases} 1, & -w \le R < -a \\ (1-\Delta_i), & -a \le R \le a \\ 1, & a < R \le w \\ 0, & otherwise \end{cases} \tag{3.8}$$

According to Eq. (3.1), the dose distribution from the ith beam is

$$D_i(x,y) = I_i(R) \tag{3.9}$$

The areametric dose of the ith beam is

$$\begin{aligned} \widetilde{D}_i &= \iint D_i(x,y)dxdy = \int_{-L}^{+L}\int_{-w}^{-a} 1 \cdot dxdy + \int_{-L}^{+L}\int_{-a}^{+a}(1-\Delta_i)dxdy + \int_{-L}^{+L}\int_{a}^{w} 1 \cdot dxdy \\ \widetilde{D}_i &= 1 \cdot 4Lw - \Delta_i \cdot 4La = 1 \cdot Area_i - \Delta_i \cdot 4La \end{aligned} \tag{3.10}$$

It is evident that the areametric dose has been reduced by a strip of width $2a$ and length $2L$ weighted by the reduction in intensity Δ_i due to the presence of the OAR, as compared to the simple 'top-hat' intensity function assumed in the previous example.

Case III (IMRT- OAR offset to side of beam path)

Suppose we have an OAR of width $2a$ which is offset to the side of the beam (Figure 3.1d). This scenario emulates what would be observed if the beam in Case II was incident at an oblique angle. Assume the intensity profile is given by

$$I_i(R) = \begin{cases} 1, & -w \le R < w - 2a \\ (1-\Delta_i), & w - 2a \le R \le w \\ 0, & otherwise \end{cases} \tag{3.11}$$

According to Eq. (3.1), the dose distribution from the *i*th beam is

$$D_i(x,y) = I_i(R) \tag{3.12}$$

The areametric dose of the *i*th beam is

$$\begin{aligned} \widetilde{D}_i &= \iint D_i(x,y)dxdy = \int_{-L}^{+L}\int_{-w}^{w-2a} 1 \cdot dxdy + \int_{-L}^{+L}\int_{w-2a}^{w} (1-\Delta_i)dxdy = 1 \cdot 4Lw - \Delta_i \cdot 4La \\ \widetilde{D}_i &= 1 \cdot Area_i - \Delta_i \cdot 4La \end{aligned} \tag{3.13}$$

As was seen in Case II, the areametric dose consists of two terms. The first term represents the unmodulated component with unit intensity (from Case I), and the second term represents the intensity modulated component producing a reduction in areametric dose by a strip of width $2a$ and length $2L$ weighted by the reduction in intensity Δ_i due to the presence of the OAR.

In summary, the mathematical theory presented establishes a relationship between geometry (BIV) and dose. For N_b incident beams, the theory postulates that the volume of maximum dose will occur in the N_b beam intersection volume. An ideal treatment would consist of the N_b BIV exactly corresponding to the Planning Target Volume (PTV) in order to minimize high dose regions in the surrounding healthy tissue. However, this ideal treatment could only be achieved with $N_b \to \infty$ for maximum target conformity. In practice, the use of a finite number of beams will result in the N_b BIV never exactly corresponding to the PTV and, therefore, producing regions of high dose in adjacent normal tissue. This will be especially important for the sparing of OARs that are in close

proximity to, as well as overlapping with the PTV, such as the rectum in prostate radiotherapy. Therefore, this work proposes locating optimal starting gantry angles for OAR sparing in IMRT using an equiangular-spaced arrangement that minimizes N_b BIV in the OAR. The inclusion of a dose calculation in the BIV theory would create weighting terms to scale the magnitude of the BIV distributions towards an absolute dose variation with beam angle. However, it will be demonstrated that the relative variation of the BIV distributions can accurately predict the relative variation of the dose distribution with beam angle and thus a more time-consuming calculation of dose is unnecessary.

3.2.2 IMRT Treatment Plans

The generation of the IMRT treatment plans using a cohort of prostate patients has been discussed in detail in Chapter 2. In brief, ten patients with localized prostate cancer treated in the supine position from October 2004 to January 2006 at CancerCare Manitoba according to the Radiation Therapy Oncology Group (RTOG) 0126 protocol were selected for this retrospective study. The Arm 2 prescription (79.2 Gy in 44 fractions) of the protocol using IMRT with 5 and 7 equiangular-spaced beam arrangements was applied. The starting gantry angles of 0°, 72°, 144°, 216°, 288° (5 beams) and 0°, 51°, 102°, 153°, 204°, 255°, 306° (7 beams) were incremented by 5° until the starting beam reached the initial angular position of the second beam, resulting in 15 (5 beams) and 11 (7 beams) plans per patient. All plans were generated in Pinnacle^3 using direct machine parameter optimization with 6 MV photon beams and static multileaf collimator delivery. The PTV coverage satisfied the RTOG 0126 protocol requirements

(V 79.2 Gy at least 98%) for all plans. Therefore, the target coverage remained constant for all plans and the variation in several bladder and rectum dose metrics (based on the RTOG 0126 protocol) as a function of starting gantry angle was investigated. In this chapter, minimization of N_b BIV in the rectum is employed to find optimal starting gantry angles that minimize the high dose rectal metrics such as V 75 Gy < 15%, and V 70 Gy < 25% and compared to results established in Chapter 2.

3.2.3 Algorithm

A starting gantry angle optimization algorithm was developed which interfaces to Pinnacle[3] version 7 (Philips Radiation Oncology Systems, Milpitas, CA, USA) in order to extract the Cartesian coordinates of the physician-delineated contours of the PTV, rectum, and bladder from patient treatment plans. The following represent the main steps of the starting gantry angle optimization algorithm: 1) For each beam source position (gantry angle) in the equiangular-spaced beam arrangement, a Beams-Eye-View (BEV) image of the PTV is produced. 2) Each BEV is divided into a grid of incident ray lines (beamlets) and ray tracing is performed through the BEV to generate a 3D matrix which models the geometrically diverging un-modulated primary beam in 3D space. 3) The coincidence volume of all 3D beams in the equiangular-spaced arrangement and all individual OARs is then calculated. 4) Each gantry angle in the equiangular-spaced arrangement is then incremented by 5° and steps 1-4 are repeated until beam 1 surpasses the original position of beam 2. In essence, the algorithm implements a very simple geometric case of the backprojection method as discussed in the theory and exhaustively

searches the coplanar, equiangular solution space. The algorithm calculated the N_b BIV in the rectum and bladder using N_b = 5 and N_b = 7 equiangular-spaced beams for a 10 patient cohort.

The Cartesian coordinates of the 75 Gy, 70 Gy, 65 Gy, and 60 Gy isodose contours were imported into the algorithm from the treatment plans. The algorithm calculated the N_b, N_b-1, N_b-2, N_b-3, and N_b-4 BIV components in the rectum within each isodose volume in order to demonstrate that the BIV within an isodose volume can reproduce the dose-volume metric. In fact, it will be demonstrated that the rectal dose-volume metrics are the superposition of the BIV components in the rectum within each isodose volume.

3.2.4 Statistical Analysis

The coefficient of variation (C_{var}), defined as the ratio of the standard deviation to the mean, and the range of variation (R_{var}), defined as the difference between the maximum value and the minimum value, were used to quantify the magnitude of variation with starting gantry angle for the dose metrics from the planning studies as well as the N_b BIV distributions. The similarity in the pattern of variation with starting gantry angle over the 10 patient cohort for the dose metrics and N_b BIV distributions was assessed by performing a statistical normalization of the data called the Z-transform $[(x_i - \bar{x})/\sigma]$, where x_i is the data value at starting gantry angle index i, $\bar{x}$ is the mean, and σ is the standard deviation. Pearson's correlation coefficient (r_{corr}), based on Z-

transformed data, was used to correlate the variation with starting gantry angle of the metrics to the N_b BIV. For 5 equiangular-spaced beams, an r_{corr} value greater than 0.514 (corresponding to a p value of less than 0.05) was considered to be a significant correlation. For 7 equiangular-spaced beams, an r_{corr} value greater than 0.602 (corresponding to a p value of less than 0.05) was considered to be a significant correlation.

3.3 Results

3.3.1 Five Equiangular-spaced Beams

Figure 3.2 illustrates the statistically normalized (Z-transform) rectal V 75 Gy, V 70 Gy, and 5 BIV with the rectum, as a function of starting gantry angle for all 10 patients using 5 equiangular-spaced beams. The similarity in 'W' pattern (with two separate minima centered near 20° and 50°) of the normalized average, minimum, and maximum values for the 10 patient cohort indicated a class solution for both the rectal V 75 Gy and V 70 Gy. This distinctive pattern was reproduced by the rectal 5 BIV. The range of variation (R_{var}) and the coefficient of variation (C_{var}) in the rectal 5 BIV were comparable to those in the rectal V 75 Gy and V 70 Gy for each patient (Table 3.1). A high correlation coefficient (r_{corr}) was found between the rectal 5 BIV and the rectal V 75 Gy and V 70 Gy indicating a strong correlation between the geometric BIV and high dose metrics (Table 3.1). The algorithm predicted the location of the two minima in rectal V 75 Gy and V 70 Gy (optimal starting gantry angles) to within 5° (Table 3.2 and Table 3.3). The predicted minima in rectal V 75 Gy and V 70 Gy differed at most by only 0.9% and 1.2%, respectively from the observed minima for the 10 patient cohort.

Figure 3.2: The statistically normalized (Z-transform) rectal a) V 75 Gy, b) V 70 Gy, and c) 5 BIV, as a function of starting gantry angle for all 10 patients using 5 equiangular-spaced beams. The characteristic 'W' pattern (with two separate minima centered near 20° and 50°) observed in the rectal V 75 Gy and V 70 Gy was reproduced by the rectal 5 BIV.

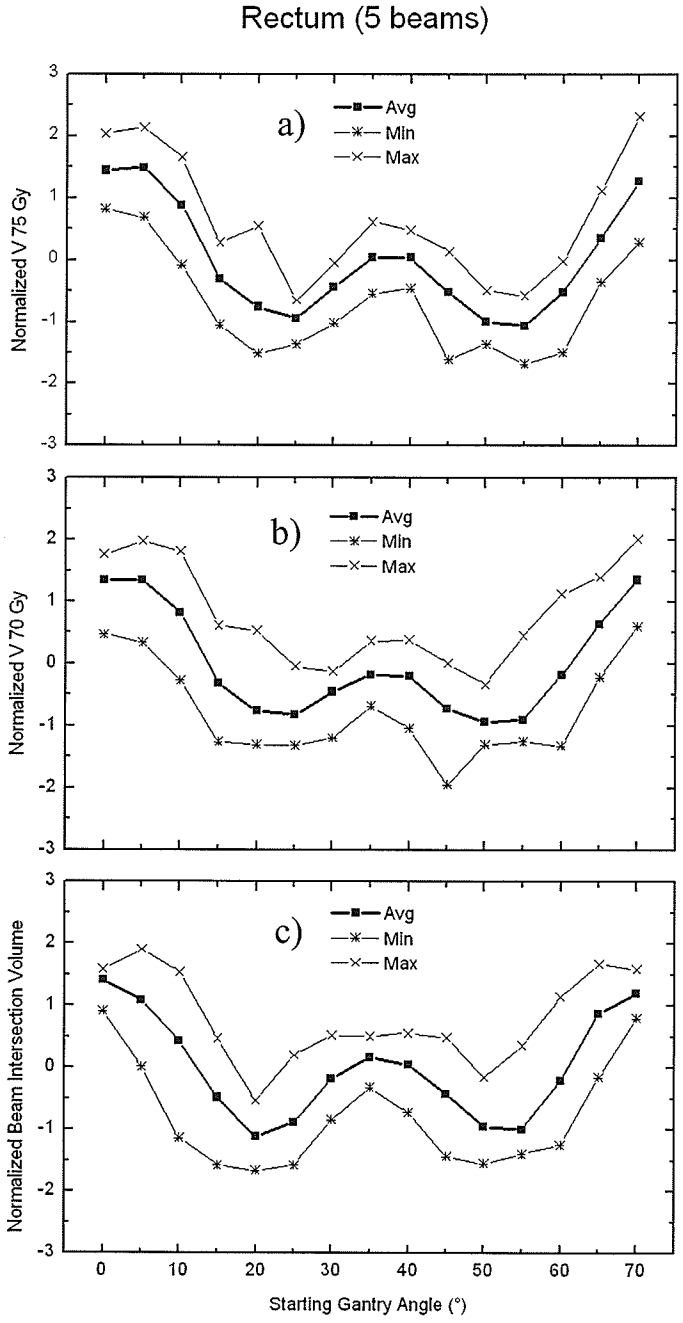

Table 3.1: The range of variation (R_{var}), coefficient of variation (C_{var}), and correlation coefficient (r_{corr}) for the rectal V 75 Gy, V 70 Gy, and beam intersection volume (BIV) using 5 equiangular-spaced beams for the 10 patient cohort.

	Rectal R_{var} (%)			*Rectal C_{var} (%)*			*Rectal BIV r_{corr}*	
Patient	V 75 Gy	V 70 Gy	BIV	V 75 Gy	V 70 Gy	BIV	V 75 Gy	V 70 Gy
1	2.4	3.8	5.9	20	13	14	0.78	0.76
2	3.2	4.3	6.7	17	15	15	0.97	0.98
3	2.9	5.0	6.9	8	8	9	0.78	0.85
4	3.0	4.4	8.6	5	6	8	0.88	0.87
5	2.3	2.6	3.3	11	9	8	0.90	0.92
6	3.9	5.8	9.4	8	8	9	0.50	0.90
7	2.9	5.2	9.9	9	12	13	0.92	0.95
8	2.4	4.6	6.3	5	8	8	0.89	0.96
9	4.6	6.6	8.6	9	10	9	0.94	0.96
10	3.9	5.2	9.1	7	7	8	0.92	0.94

Table 3.2: The locations of the two minima in rectal V 75 Gy (optimal starting gantry angles) as predicted by the algorithm for the 10 patient cohort.

	V 75 Gy min #1 (%)			V 75 Gy min #2 (%)		
Patient	Observed	Predicted	Difference (%)	Observed	Predicted	Difference (%)
1	2.9 (25°)	3.8 (20°)	0.9	2.3 (45°)	2.3 (45°)	0.0
2	4.7 (15°)	4.7 (15°)	0.0	4.4 (50°)	4.4 (50°)	0.0
3	10.3 (25°)	10.8 (20°)	0.5	10.0 (55°)	10.7 (50°)	0.7
4	16.3 (30°)	16.6 (25°)	0.3	15.9 (60°)	16.5 (55°)	0.6
5	5.4 (20°)	5.8 (25°)	0.4	5.6 (55°)	5.6 (55°)	0.0
6	13.5 (15°)	13.5 (15°)	0.0	13.3 (45°)	13.3 (45°)	0.0
7	8.6 (20°)	8.6 (20°)	0.0	8.6 (50°)	9.2 (55°)	0.6
8	14.6 (25°)	14.8 (20°)	0.2	14.6 (55°)	14.7 (50°)	0.1
9	14.1 (20°)	14.1 (20°)	0.0	13.7 (50°)	13.7 (50°)	0.0
10	17.2 (25°)	17.2 (25°)	0.0	17.4 (55°)	17.4 (55°)	0.0

Table 3.3: The locations of the two minima in rectal V 70 Gy (optimal starting gantry angles) as predicted by the algorithm for the 10 patient cohort.

	V 70 Gy min #1 (%)			V 70 Gy min #2 (%)		
Patient	Observed	Predicted	Difference (%)	Observed	Predicted	Difference (%)
1	7.2 (25°)	8.4 (20°)	1.2	5.8 (45°)	5.8 (45°)	0.0
2	8.3 (15°)	8.3 (15°)	0.0	7.8 (50°)	7.8 (50°)	0.0
3	16.1 (25°)	16.4 (20°)	0.3	16.2 (55°)	16.5 (50°)	0.3
4	22.4 (30°)	22.7 (25°)	0.3	21.7 (60°)	22.3 (55°)	0.6
5	8.1 (30°)	8.4 (25°)	0.3	8.1 (55°)	8.1 (55°)	0.0
6	19.8 (15°)	19.8 (15°)	0.0	19.4 (45°)	19.4 (45°)	0.0
7	13.1 (20°)	13.1 (20°)	0.0	13.1 (50°)	13.9 (55°)	0.8
8	18.9 (25°)	19.0 (20°)	0.1	18.7 (50°)	18.7 (50°)	0.0
9	20.2 (20°)	20.2 (20°)	0.0	19.8 (50°)	19.8 (50°)	0.0
10	24.0 (25°)	24.0 (25°)	0.0	24.0 (55°)	24.0 (55°)	0.0

Figure 3.3 illustrates the exact reproduction (r_{corr} = 0.99-1.00) of the rectal V 75 Gy, V 65 Gy, and V 60 Gy variation with starting gantry angle using the superposition of the BIV components (5 BIV + 4 BIV + 3 BIV + 2 BIV + 1 BIV) in the rectum and within each isodose volume (total BIV 75 Gy, total BIV 65 Gy, and total BIV 60 Gy) for a typical prostate patient. It was interesting to observe that the bladder V 75 Gy, V 70 Gy, and 5 BIV did not exhibit any 'W' pattern as was seen for the rectum. In fact, the small coefficient of variation (C_{var}) observed in the relatively flat distribution with starting gantry angle of the bladder V 75 Gy and V 70 Gy was reproduced by the bladder 5 BIV for each patient (Table 3.4).

Figure 3.3: The exact reproduction of the rectal a) V 75 Gy, b) V 65 Gy, and c) V 60 Gy variation with starting gantry angle using the superposition of the BIV components in the rectum and within each isodose volume for a typical prostate patient.

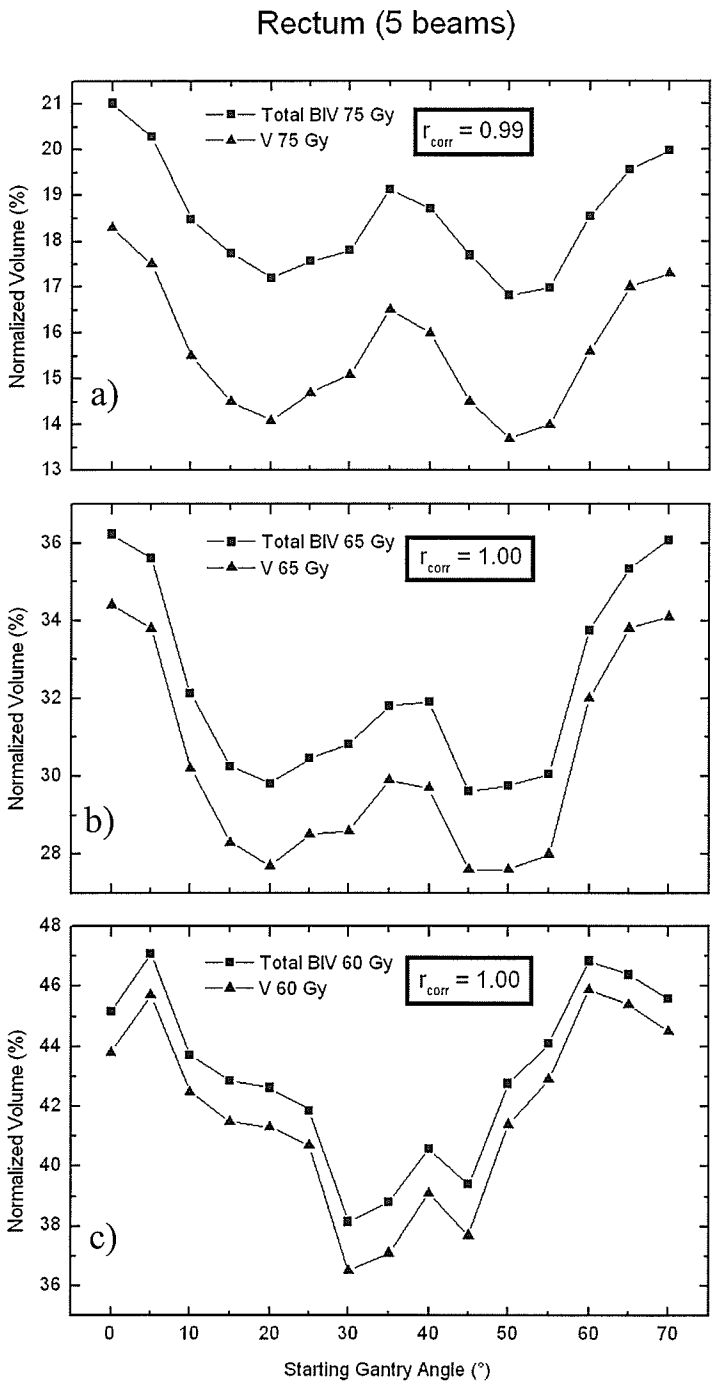

Table 3.4: The coefficient of variation (C_{var}) for the bladder V 75 Gy, V 70 Gy, and beam intersection volume (BIV) using 5 and 7 equiangular-spaced beams for the 10 patient cohort.

	5 beam Bladder C_{var} (%)			7 beam Bladder C_{var} (%)		
Patient	V 75 Gy	V 70 Gy	BIV	V 75 Gy	V 70 Gy	BIV
1	2	2	1	1	1	2
2	3	2	2	2	1	2
3	2	2	1	1	1	2
4	2	2	1	1	1	1
5	2	2	2	2	2	2
6	2	2	2	3	1	2
7	3	2	2	2	2	2
8	1	2	1	1	1	1
9	2	1	2	3	2	1
10	1	1	1	2	1	1

3.3.2 Seven Equiangular-spaced Beams

Figure 3.4 illustrates the statistically normalized (Z-transform) rectal V 75 Gy, V 70 Gy, and 7 BIV, as a function of starting gantry angle for all 10 patients using 7 equiangular-spaced beams. The 7 BIV demonstrated a characteristic 'W' pattern, however, unlike with 5 beams, there was no such dosimetric pattern in the rectal V 75 Gy and V 70 Gy. The range of variation (R_{var}) and the coefficient of variation (C_{var}) in the rectal V 75 Gy, V 70 Gy, and 7 BIV were reduced compared to those with 5 beams (Table 3.5). Only one patient (7) demonstrated a significant correlation (r_{corr}) between the rectal 7 BIV and the rectal V 75 Gy and V 70 Gy.

Figure 3.4: The statistically normalized (Z-transform) rectal a) V 75 Gy, b) V 70 Gy, and c) 7 BIV, as a function of starting gantry angle for all 10 patients using 7 equiangular-spaced beams. The 7 BIV demonstrated a characteristic 'W' pattern, however, unlike with 5 beams, there was no such dosimetric pattern in the rectal V 75 Gy and V 70 Gy.

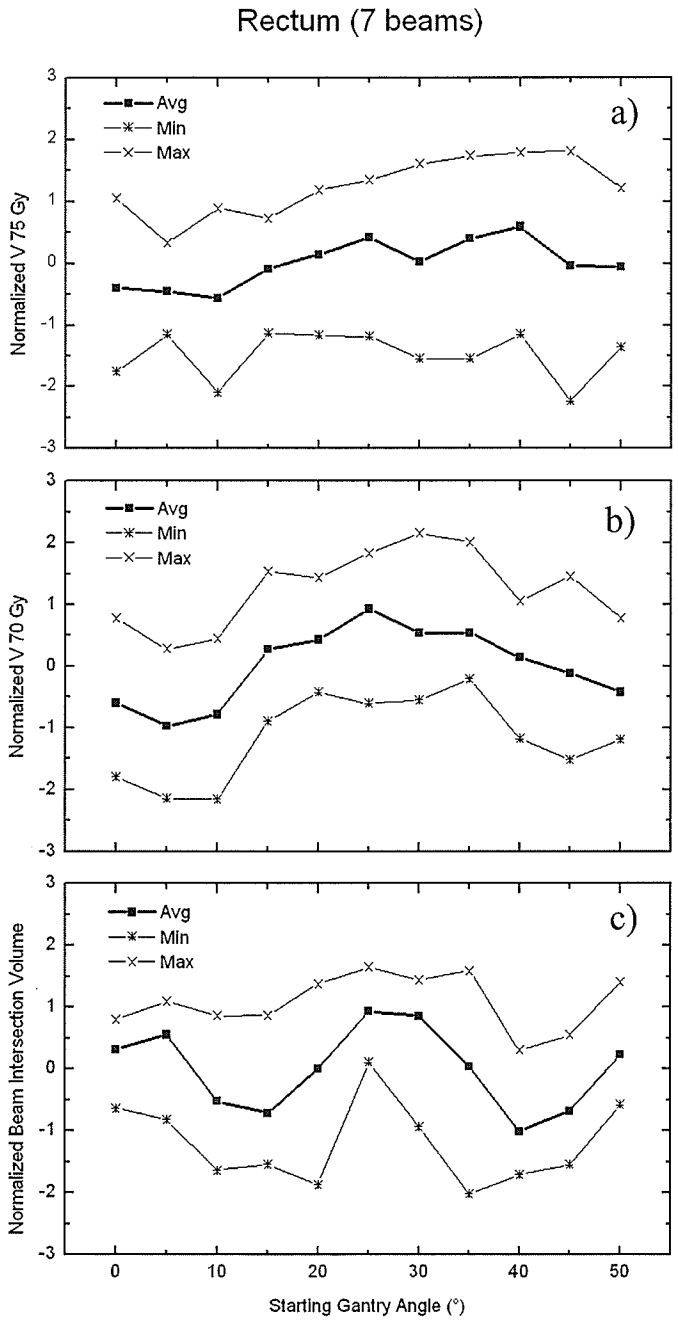

Table 3.5: The range of variation (R_{var}), coefficient of variation (C_{var}), and correlation coefficient (r_{corr}) for the rectal V 75 Gy, V 70 Gy, and beam intersection volume (BIV) using 7 equiangular-spaced beams for the 10 patient cohort.

	Rectal R_{var} (%)			*Rectal C_{var} (%)*			*Rectal BIV r_{corr}*	
Patient	V 75 Gy	V 70 Gy	BIV	V 75 Gy	V 70 Gy	BIV	V 75 Gy	V 70 Gy
1	0.8	1.4	2.6	11	7	8	-0.43	-0.21
2	0.8	0.9	2.8	4	3	8	0.39	0.33
3	1.5	2.5	3.2	5	4	5	0.19	0.56
4	0.6	1.3	4.1	1	2	4	0.42	0.38
5	0.6	0.9	1.0	3	3	3	-0.06	-0.02
6	0.9	1.7	4.3	2	3	5	-0.40	0.20
7	0.5	1.3	5.5	2	3	10	0.78	0.82
8	1.1	1.5	2.9	3	2	4	-0.17	0.68
9	1.0	1.5	3.9	2	3	6	0.02	0.37
10	0.9	0.9	4.6	2	1	5	-0.89	-0.30

As was observed with 5 beams, the bladder V 75 Gy, V 70 Gy, and 7 BIV did not exhibit any 'W' pattern. The small coefficient of variation (C_{var}) observed in the relatively flat distribution with starting gantry angle of the bladder V 75 Gy and V 70 Gy was reproduced by the bladder 7 BIV for each patient (Table 3.4).

3.4 Discussion

It has been demonstrated that, even with intensity modulation, there was a strong correlation between the characteristic 'W' pattern observed in the rectal V 75 Gy and V 70 Gy with the 5 BIV as a function of starting gantry angle. This was a verification of the theory presented in that it confirmed that the volume of maximum dose within a critical structure (as assessed by the rectal V 75 Gy and V 70 Gy) was proportional to the intersection volume of all beams within that structure despite the ability to highly modulate the radiation beams. It is important to note that even with the assumption of uniform incident intensity (equal beamlet weights) for all beams in the purely geometric BIV algorithm, there was a strong correlation between the geometric 5 BIV and high dose rectal metrics. This can be understood from the theory presented in section 3.2.1 of the Methods and Materials in that, for each beam, the intensity acts as a weighting in the proportionality between the maximum dose in a critical structure and the volume of beam intersection within that structure (herein referred to as the 'proportionality relationship'). In current practice, an IMRT beam will never be so highly modulated to have it's intensity completely diminished within a critical structure since a minimum non-zero level of intensity is required for target coverage. Therefore, a proportionality relationship will always exist. In prostate IMRT, the results of this work demonstrate that the low level of intensity modulation with 5 beams produces a very strong proportionality relationship.

The 'W' pattern observed in the rectal V 75 Gy, V 70 Gy and 5 BIV as a function of starting gantry angle was produced by the beam geometry. Figure 3.5 illustrates this effect in two dimensions on a representative computerized tomography (CT) slice for a typical prostate patient (patient 9). Figure 3.5a and 3.5c illustrate the 'W' pattern maxima in rectal 5 BIV at starting gantry angles of 0° and 35°. These two equiangular-spaced beam configurations are nearly mirror reflections of each other about the patient midline. From a geometrical point of view, a perfectly symmetric 'W' pattern (with equal magnitude maxima at starting gantry angles of 0° and 35°) should be produced if the rectum and PTV are perfectly symmetric about their midline on each CT slice. This is approximately the case on the CT slice shown in Figure 3.5a and 3.5c where the rectal 5 BIV at starting gantry angles of 0° and 35° are approximately equal. However, the observed 'W' patterns in rectal V 75 Gy, V 70 Gy, and 5 BIV are not symmetric, demonstrating a slightly lower maximum at 35° compared to 0°. This likely results from the fact that the rectum and PTV are not perfectly symmetric about their midline in 3D. Figure 3.5b and 3.5d also demonstrates the 'W' pattern minima in rectal 5 BIV at starting gantry angles of 20° and 50°. Again, these two equiangular-spaced beam configurations are nearly mirror reflections of each other about the patient midline. The optimal configurations for rectal sparing occur with a nearly lateral beam (gantry 92° or 266°) which minimizes the 5 BIV in the rectum and furthermore helps to form a sharp dose gradient between the PTV and rectum as will be further discussed in Chapter 5.

Figure 3.5: Geometrical 'W' pattern effect in two dimensions on a representative CT slice for a typical prostate patient. a) and c) are maxima in rectal 5 BIV at starting gantry angles of 0° and 35°. b) and d) are minima in rectal 5 BIV at starting gantry angles of 20° and 50°. The PTV and rectum contours are shown in red and black, respectively. The rectal 5 BIV is shaded in black.

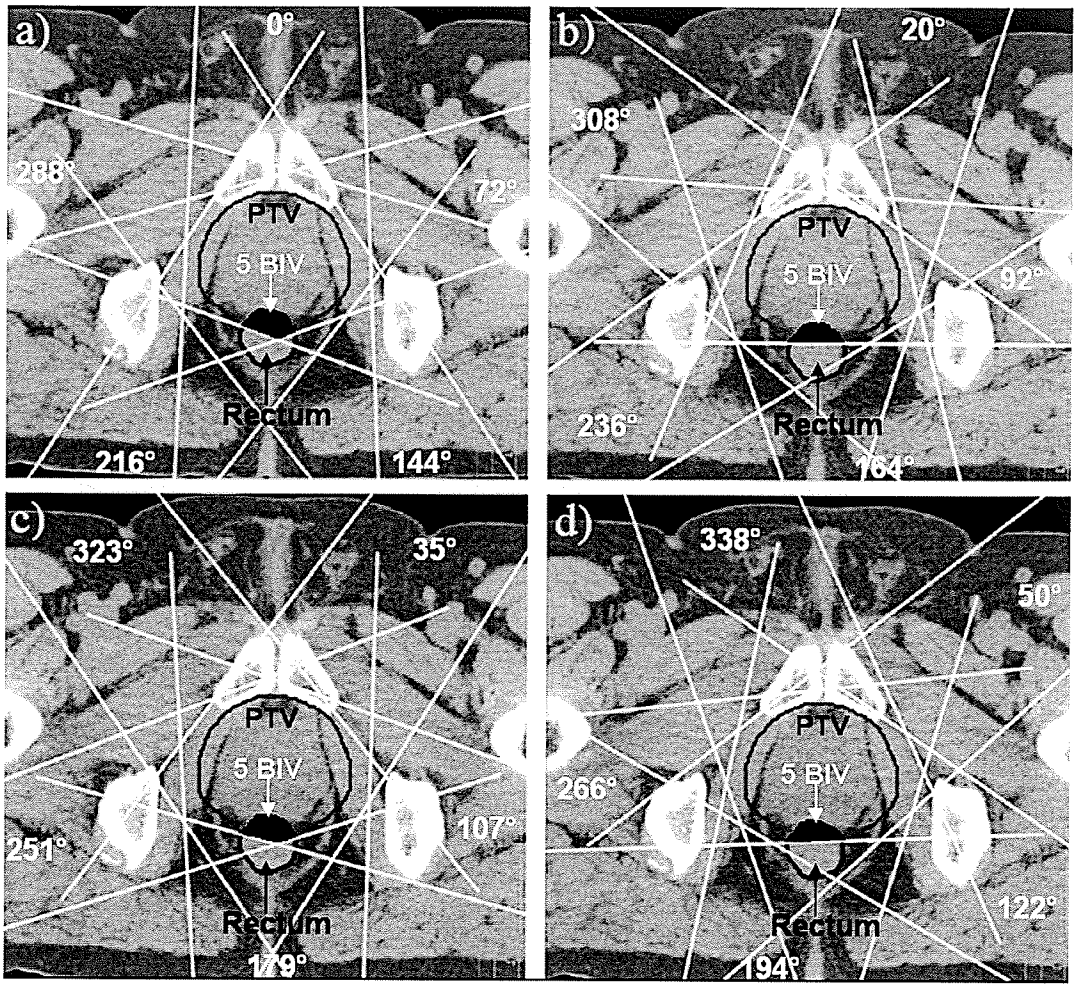

Schreibmann *et al.* [40] investigated beam orientation class solutions in prostate IMRT. The authors used a genetic algorithm to optimize the beam orientations and a gradient-based method to optimize the intensity profiles of the beams. They concluded that the optimized 5 beam configurations in all 15 patient cases they examined had a similar beam setup, with nearly equiangular-spaced beams starting at the beam position of 20°- 45°. They proposed a class solution with 5 incident nearly equiangular-spaced beams (gantry = 35°, 110°, 180°, 250°, 325°) by averaging the optimal gantry angles of all fifteen patients even though optimal starting gantry angle solutions for individual patients were either near 15° *or* 50°. However, the results from this chapter and Chapter 2 indicate that there is degeneracy in the optimal starting gantry angle solution with two possible solutions (not attributable to prostate patient variability). It has been demonstrated that a class solution with starting gantry angle of 35° is not optimal since it coincides with a local maximum in the 'W' pattern of the rectal V 75, V 70 Gy, and 5 BIV. Schreibmann *et al.* suggested that this class solution seems to be physically sensible since setting the angles of beams 1, 2, and 4 to 35°, 110°, and 250°, respectively balances the dose to the femoral heads and the locations of the third (180°) and fifth (325°) beams are chosen to balance the dose requirements of the PTV and rectum. However, this work has reproduced the optimal starting gantry angles of Schreibmann *et al.* solely based on variations in 5 BIV with the rectum as a function of starting gantry angle. Therefore, the optimal starting gantry angles seem to be primarily the result of rectal sparing required by the objective function of the IMRT optimization and are highly correlated with the geometric effect of rectal 5 BIV. These results are a validation of the optimal 5 equiangular-spaced beam configurations for individual patients presented by

Schreibmann *et al.* and provide further refinement by recognizing that two optimal class solutions exist for prostate IMRT with equiangular-spaced beams. Furthermore, this work has been able to reproduce the Schreibmann *et al.* dosimetrically optimized beam configurations based on simple geometrical 5 BIV with the rectum without the need to invoke complicated, time-consuming and computationally-intensive dosimetric optimization methods.

The exact reproduction of the rectal dose-volume metric variation with starting gantry angle through the superposition of the BIV components within the isodose volume using 5 equiangular-spaced beams (Figure 3.3) demonstrates, as expected, that a dose-volume histogram is the superposition of volume-weighted BIV components. The small discrepancy (1-3%) between the normalized volume of the rectal dose-volume metric and the total BIV for each starting gantry angle is due to the algorithm performing several image processing operations (region filling, dilation, erosion) on the rectal and PTV contours which discretize the smooth contours into coarser pixels. Figure 3.3 also illustrates the high accuracy of the algorithm since the small volumetric discrepancies arising from the image processing operations did not affect the angular accuracy (demonstrated by the high correlation coefficients of 0.99-1.00). Even though the superposition of the BIV components within an isodose volume was calculated with *a priori* knowledge of the dose distribution, this demonstrates that beam geometry (BIV) can reproduce effects in the dose distribution and will be explored further in Chapter 4. This is the first work to reproduce dose-volume metrics based on geometry alone and has exciting implications for radiotherapy optimization as will be discussed in Chapter 4.

The use of 7 equiangular-spaced beams resulted in the dose distribution becoming less dependent on rectal BIV. This was demonstrated by the disappearance of the dosimetric 'W' pattern in rectal V 75 Gy and V 70 Gy (from Chapter 2) although the 7 BIV still demonstrated such a pattern. However, the range of variation (R_{var}) and the coefficient of variation (C_{var}) in the rectal 7 BIV were reduced by approximately half compared to those with 5 BIV. Apparently, the 7 BIV geometric variations were too small to translate into a strong dosimetric effect. Also, the IMRT optimization had two more degrees of freedom (beams) to compensate for beam directions delivering high rectal dose. These results support the findings of other investigators also demonstrating that as the number of IMRT beams is increased, the dose dependence on beam orientation diminishes [5, 7].

It was observed that both the bladder 5 BIV and 7 BIV did not exhibit any 'W' pattern as was seen for the rectum. Instead, a relatively flat distribution (small coefficient of variation, C_{var}) as a function of starting gantry angle in the 5 BIV and 7 BIV reproduced the flat distribution in bladder V 75 Gy and V 70 Gy. The different responses with starting gantry angle observed between the rectum and bladder are due to the volume of each organ in the primary beam paths. Specifically, a much smaller bladder volume is exposed to the primary beams compared to the rectum, therefore, dose-volume variations are magnified over the larger rectal volume. For example, for a typical prostate patient using 5 equiangular-spaced beams, the maximum in 5 BIV as a function of starting gantry angle was 35% for the rectum and only 8% for the bladder.

The presented BIV algorithm has only been applied to coplanar beam geometry, however, it may be easily used to compute BIV using non-coplanar beams. A generalized BIV algorithm which selects optimal deliverable beam orientations (that minimize the BIV within OARs) from the complete space of gantry and couch angles is presented in Chapter 4. The BIV optimization approach has potential to produce improved OAR sparing in other treatment sites such as the head-and-neck and abdomen, as will be discussed in Chapter 4. The current algorithm is written using the Interactive Data Language (IDL; RSI, Boulder, CO). With the use of this high-level programming language for developmental purposes, typical computation times for the current BIV algorithm are on the order of a few minutes but can be reduced by a factor of 100 or more by using a lower level programming language such as C.

3.5 Conclusions

In this chapter, it was demonstrated that the rectal 5 BIV is strongly correlated to the rectal high-dose metrics of IMRT plans. The geometric minima in rectal 5 BIV corresponded to the dosimetric minima in rectal V 75 Gy and V 70 Gy. The implication of this is that a geometric quantity such as BIV can be used to predict the optimal dose distribution for rectal sparing in prostate IMRT using 5 equiangular-spaced beams. It was shown that a dose-volume metric is the superposition of volume-weighted BIV components within the isodose volume. A mathematical theory was presented which explains the correlation of BIV with dose and dose-volume metrics. A geometric optimization method based on BIV has the advantage over dosimetric methods of

simplicity and rapid computation time. In this work, the geometric algorithm was able to predict the dosimetric minima to within 5° (the angular step size used here). This algorithm can be used as a standalone optimization method or act as a rapid calculation filter to reduce the search space for a dosimetric beam orientation optimization method, as will be discussed in Chapter 6. Given the clinically infeasible computation times of many dosimetric beam orientation optimization algorithms, this robust BIV algorithm has the potential to facilitate beam angle selection for prostate IMRT in clinical practice.

3.6 Bibliography

1. Chao, K.S., J.O. Deasy, et al., *A prospective study of salivary function sparing in patients with head-and-neck cancers receiving intensity-modulated or three-dimensional radiation therapy: initial results.* Int J Radiat Oncol Biol Phys, 2001. **49**(4): p. 907-16.
2. Lee, A. de, et al., *A comparison of intensity-modulated radiation therapy and concomitant boost radiotherapy in the setting of concurrent chemotherapy for locally advanced oropharyngeal carcinoma.* International Journal of Radiation Oncology, Biology, Physics, 2006. **66**(4): p. 966.
3. Urbano, Henrys, et al., *Intensity-modulated radiotherapy in patients with locally advanced rectal cancer reduces volume of bowel treated to high dose levels.* International Journal of Radiation Oncology, Biology, Physics, 2006. **65**(3): p. 907.

4. Wang, C., Xia, et al., *Intensity-modulated radiotherapy improves lymph node coverage and dose to critical structures compared with three-dimensional conformal radiation therapy in clinically localized prostate cancer.* International Journal of Radiation Oncology, Biology, Physics, 2006. **66**(3): p. 654.

5. Stein, J., R. Mohan, et al., *Number and orientations of beams in intensity-modulated radiation treatments.* Med Phys, 1997. **24**(2): p. 149-60.

6. Bortfeld, T. and W. Schlegel, *Optimization of beam orientations in radiation therapy: some theoretical considerations.* Phys Med Biol, 1993. **38**(2): p. 291-304.

7. Soderstrom, S. and A. Brahme, *Which is the most suitable number of photon beam portals in coplanar radiation therapy?* Int J Radiat Oncol Biol Phys, 1995. **33**(1): p. 151-9.

8. Liu, H.H., M. Jauregui, et al., *Beam angle optimization and reduction for intensity-modulated radiation therapy of non-small-cell lung cancers.* Int J Radiat Oncol Biol Phys, 2006. **65**(2): p. 561-72.

9. Wang, X., X. Zhang, et al., *Development of methods for beam angle optimization for IMRT using an accelerated exhaustive search strategy.* Int J Radiat Oncol Biol Phys, 2004. **60**(4): p. 1325-37.

10. Kim, S., H.C. Akpati, et al., *An immobilization system for claustrophobic patients in head-and-neck intensity-modulated radiation therapy.* Int J Radiat Oncol Biol Phys, 2004. **59**(5): p. 1531-9.

11. Ezzell, G.A., *Genetic and geometric optimization of three-dimensional radiation therapy treatment planning.* Med Phys, 1996. **23**(3): p. 293-305.

12. Haas, O.C., K.J. Burnham, et al., *Optimization of beam orientation in radiotherapy using planar geometry.* Phys Med Biol, 1998. **43**(8): p. 2179-93.

13. Meyer, J., S.M. Hummel, et al., *Automatic selection of non-coplanar beam directions for three-dimensional conformal radiotherapy.* Br J Radiol, 2005. **78**(928): p. 316-27.

14. Rowbottom, C.G., V.S. Khoo, et al., *Simultaneous optimization of beam orientations and beam weights in conformal radiotherapy.* Med Phys, 2001. **28**(8): p. 1696-702.

15. Rowbottom, C.G., M. Oldham, et al., *Constrained customization of non-coplanar beam orientations in radiotherapy of brain tumours.* Phys Med Biol, 1999. **44**(2): p. 383-99.

16. Rowbottom, C.G., S. Webb, et al., *Improvements in prostate radiotherapy from the customization of beam directions.* Med Phys, 1998. **25**(7 Pt 1): p. 1171-9.

17. Schreibmann, E., M. Lahanas, et al., *A geometry based optimization algorithm for conformal external beam radiotherapy.* Phys Med Biol, 2003. **48**(12): p. 1825-41.

18. Wang, C., J. Dai, et al., *Optimization of beam orientations and beam weights for conformal radiotherapy using mixed integer programming.* Phys Med Biol, 2003. **48**(24): p. 4065-76.

19. Wu, X. and Y. Zhu, *A mixed-encoding genetic algorithm with beam constraint for conformal radiotherapy treatment planning.* Med Phys, 2000. **27**(11): p. 2508-16.

20. Bedford, J.L. and S. Webb, *Elimination of importance factors for clinically accurate selection of beam orientations, beam weights and wedge angles in conformal radiation therapy.* Med Phys, 2003. **30**(7): p. 1788-804.

21. Gokhale, P., E.M. Hussein, et al., *Determination of beam orientation in radiotherapy planning.* Med Phys, 1994. **21**(3): p. 393-400.

22. Rowbottom, C.G., S. Webb, et al., *Beam-orientation customization using an artificial neural network.* Phys Med Biol, 1999. **44**(9): p. 2251-62.

23. Woudstra, E. and B.J. Heijmen, *Automated beam angle and weight selection in radiotherapy treatment planning applied to pancreas tumors.* Int J Radiat Oncol Biol Phys, 2003. **56**(3): p. 878-88.

24. Beaulieu, F., L. Beaulieu, et al., *Simultaneous optimization of beam orientations, wedge filters and field weights for inverse planning with anatomy-based MLC fields.* Med Phys, 2004. **31**(6): p. 1546-57.

25. Djajaputra, D., Q. Wu, et al., *Algorithm and performance of a clinical IMRT beam-angle optimization system.* Phys Med Biol, 2003. **48**(19): p. 3191-212.

26. D'Souza, W.D., R.R. Meyer, et al., *Selection of beam orientations in intensity-modulated radiation therapy using single-beam indices and integer programming.* Phys Med Biol, 2004. **49**(15): p. 3465-81.

27. Gaede, S. and E. Wong, *An algorithm for systematic selection of beam directions for IMRT.* Med Phys, 2004. **31**(2): p. 376-88.

28. Hou, Q., J. Wang, et al., *Beam orientation optimization for IMRT by a hybrid method of the genetic algorithm and the simulated dynamics.* Med Phys, 2003. **30**(9): p. 2360-7.

29. Lee, E.K., T. Fox, et al., *Simultaneous beam geometry and intensity map optimization in intensity-modulated radiation therapy.* Int J Radiat Oncol Biol Phys, 2006. **64**(1): p. 301-20.

30. Li, Y., D. Yao, et al., *A particle swarm optimization algorithm for beam angle selection in intensity-modulated radiotherapy planning.* Phys Med Biol, 2005. **50**(15): p. 3491-514.

31. Li, Y., J. Yao, et al., *Automatic beam angle selection in IMRT planning using genetic algorithm.* Phys Med Biol, 2004. **49**(10): p. 1915-32.

32. Meedt, G., M. Alber, et al., *Non-coplanar beam direction optimization for intensity-modulated radiotherapy.* Phys Med Biol, 2003. **48**(18): p. 2999-3019.

33. Pugachev, A., J.G. Li, et al., *Role of beam orientation optimization in intensity-modulated radiation therapy.* Int J Radiat Oncol Biol Phys, 2001. **50**(2): p. 551-60.

34. Pugachev, A. and L. Xing, *Pseudo beam's-eye-view as applied to beam orientation selection in intensity-modulated radiation therapy.* Int J Radiat Oncol Biol Phys, 2001. **51**(5): p. 1361-70.

35. Pugachev, A. and L. Xing, *Computer-assisted selection of coplanar beam orientations in intensity-modulated radiation therapy.* Phys Med Biol, 2001. **46**(9): p. 2467-76.

36. Pugachev, A. and L. Xing, *Incorporating prior knowledge into beam orientation optimization in IMRT.* Int J Radiat Oncol Biol Phys, 2002. **54**(5): p. 1565-74.

37. Pugachev, A.B., A.L. Boyer, et al., *Beam orientation optimization in intensity-modulated radiation treatment planning.* Med Phys, 2000. **27**(6): p. 1238-45.

38. Rowbottom, C.G., C.M. Nutting, et al., *Beam-orientation optimization of intensity-modulated radiotherapy: clinical application to parotid gland tumours.* Radiother Oncol, 2001. **59**(2): p. 169-77.

39. Schreibmann, E., M. Lahanas, et al., *Multiobjective evolutionary optimization of the number of beams, their orientations and weights for intensity-modulated radiation therapy.* Phys Med Biol, 2004. **49**(5): p. 747-70.

40. Schreibmann, E. and L. Xing, *Feasibility study of beam orientation class-solutions for prostate IMRT.* Med Phys, 2004. **31**(10): p. 2863-70.

41. Schreibmann, E. and L. Xing, *Dose-volume based ranking of incident beam direction and its utility in facilitating IMRT beam placement.* Int J Radiat Oncol Biol Phys, 2005. **63**(2): p. 584-93.

42. Wang, X., X. Zhang, et al., *Effectiveness of noncoplanar IMRT planning using a parallelized multiresolution beam angle optimization method for paranasal sinus carcinoma.* Int J Radiat Oncol Biol Phys, 2005. **63**(2): p. 594-601.

43. Yang, R., J. Dai, et al., *Beam orientation optimization for intensity-modulated radiation therapy using mixed integer programming.* Phys Med Biol, 2006. **51**(15): p. 3653-66.

44. Das, S., T. Cullip, et al., *Beam orientation selection for intensity-modulated radiation therapy based on target equivalent uniform dose maximization.* Int J Radiat Oncol Biol Phys, 2003. **55**(1): p. 215-24.

45. Soderstrom, S. and A. Brahme, *Selection of suitable beam orientations in radiation therapy using entropy and Fourier transform measures.* Phys Med Biol, 1992. **37**(4): p. 911-924.

46. Woudstra, E., B.J. Heijmen, et al., *Automated selection of beam orientations and segmented intensity-modulated radiotherapy (IMRT) for treatment of oesophagus tumors.* Radiother Oncol, 2005. **77**(3): p. 254-61.

47. Deasy, J.O., *Multiple local minima in radiotherapy optimization problems with dose-volume constraints.* Med Phys, 1997. **24**(7): p. 1157-61.

48. Burman, C.M., M.J. Zelefsky, et al., *Treatment Planning, Dose Delivery, and Outcome of IMRT for Localized Prostate Cancer*, in *A Practical Guide to Intensity-Modulated Radiation Therapy*, Z. Fuks, S.A. Leibel, and C.C. Ling, Editors. 2003, Medical Physics Publishing: Madison, Wisconsin. p. 169-190.

49. Nutting, C.M., D.J. Convery, et al., *Reduction of small and large bowel irradiation using an optimized intensity-modulated pelvic radiotherapy technique in patients with prostate cancer.* Int J Radiat Oncol Biol Phys, 2000. **48**(3): p. 649-56.

50. Zelefsky, M.J., Z. Fuks, et al., *Clinical experience with intensity modulated radiation therapy (IMRT) in prostate cancer.* Radiother Oncol, 2000. **55**(3): p. 241-9.

51. Zelefsky, M.J., Z. Fuks, et al., *High dose radiation delivered by intensity modulated conformal radiotherapy improves the outcome of localized prostate cancer.* J Urol, 2001. **166**(3): p. 876-81.

52. Zelefsky, M.J., Z. Fuks, et al., *High-dose intensity modulated radiation therapy for prostate cancer: early toxicity and biochemical outcome in 772 patients.* Int J Radiat Oncol Biol Phys, 2002. **53**(5): p. 1111-6.

53. Zelefsky, M.J., Z. Fuks, et al., *Intensity-modulated radiation therapy for prostate cancer.* Semin Radiat Oncol, 2002. **12**(3): p. 229-37.

54. Macovski, A., *Medical Imaging Systems*. 1983: Prentice-Hall.

CHAPTER FOUR: A NEW PARADIGM FOR IMPROVING IMRT: SELECTION OF BEAM ORIENTATIONS BY OPTIMIZING BEAM INTERSECTION VOLUME

This chapter is adapted from a manuscript entitled "A New Paradigm for Improving IMRT: Selection of Beam Orientations by Optimizing Beam Intersection Volume" by Peter Potrebko and Boyd McCurdy submitted to *Medical Physics* in 2007.

4.1 Introduction

Intensity-modulated radiation therapy (IMRT), sophisticated as it is, still requires the treatment planner to manually select beam orientations based on experience and intuition. There is no way of determining whether the manually chosen set of beam orientations will improve the quality of the plan (compared to standard equiangular-spaced beam arrangements) until the IMRT optimization and final dose calculation are performed. Therefore, this process involves a time-consuming trial-and-error approach. It is common clinical practice to employ a relatively large number of beams, such as nine coplanar equiangular-spaced beams. This strategy is based on several publications in the early days of IMRT which demonstrated that the IMRT plan may not be sensitive to the choice of individual beam angles when using a large number of equiangular-spaced beams [1-3]. However, more recent studies have indicated that optimal critical structure sparing will not necessarily be achieved with the use of a large number of equiangular-spaced beams [4, 5]. Furthermore, potential benefits of using a larger number of beams may be offset by the spread of low doses to larger volumes of normal tissues [6, 7],

increased treatment delivery time, quality assurance efforts, and the probability of patient movement during delivery [8].

Many beam orientation optimization (BOO) methods have been proposed in both three-dimensional conformal radiation therapy (3D-CRT) [1, 9-21] and IMRT [1-3, 6, 7, 22-43] with the ultimate goal of improving radiotherapy treatment plans using *the fewest number of optimal beams possible.* Since BOO inherently reduces to a mathematical optimization problem, several optimization techniques such as an exhaustive search (or variations of it) [6, 7, 21, 25, 30, 40, 43], simulated annealing [12, 13, 18, 22, 23, 31, 34-36], genetic algorithms [9, 17, 26, 29, 37, 38], and integer programming [16, 24, 27, 41] have been employed. Despite the ability of published BOO methods to improve IMRT treatment plans, several factors present challenges for these methods to be adopted clinically. First, the vastness of the beam orientation search space requires the evaluation of many trial sets of beam orientations, a potentially time-consuming endeavor depending on the optimization method. Second, the search space is complex and can contain local minima [44]. Therefore, slower stochastic-based optimization techniques such as simulated annealing and genetic algorithms are preferred over fast gradient algorithms to avoid local minima trapping. Third, regardless of which optimization technique is used, dose-based BOO methods in IMRT require the optimization of fluence maps for each trial set of beam orientations. This is a computationally intensive process and consequently many published dose-based BOO approaches have clinically infeasible computation times (0.5 to > 200 hours) per patient.

As an alternative to performing time-consuming dose calculations for every trial set of beam orientations in the BOO process, geometric quantities acting as surrogates for dose can be evaluated instead. Only a few geometric optimization methods (all applied to 3D-CRT) have been published [9-11, 15], despite the potential to greatly reduce the complexity and time of optimizations. Schreibmann *et al.* [15] presented a geometry-based BOO algorithm for 3D-CRT which optimized a geometrical cost function adapted from earlier work by Haas *et al.* [10]. The sparing of an Organ-at-Risk (OAR) was achieved by minimizing a term in the geometrical cost function representing the exposure of the OAR in the beams. However, this term only summed the intersection volume between each individual beam and the OAR. Therefore, dose 'hot spots' from the superposition of beams were not considered. In Chapter 3, Potrebko *et al.* proposed the use of beam intersection volume (BIV), including the superposition of BIV components, to optimize prostate IMRT plans in a limited solution space.

In this chapter, a BOO algorithm for IMRT is proposed based on optimizing BIV components within an OAR. A true multi-objective optimization technique, with the ability to optimize multiple BIV components within several critical structures, is the subject of future work. In contrast to the OAR exposure term (in the geometrical cost function) presented by Schreibmann *et al.* [15], the BIV concept evaluates the superposition of multiple beams within an OAR and thus acts as a surrogate for regions of high dose. The algorithm automatically selects 5 optimal beam orientations which produce improved OAR sparing compared to standard equiangular-spaced coplanar beam arrangements using 5, 7, and 9 fields. Three different disease sites including gastric,

prostate, and oropharynx (two examples) have been investigated here. It is demonstrated that BIV-based BOO is a practical method for the selection of beam orientations in clinical IMRT.

4.2 Methods and Materials

4.2.1 Beam Intersection Volume

In Chapter 3, a mathematical theory to establish a relationship between geometry (BIV within an OAR) and dose was presented. For N incident beams, the theory postulated that the volume of maximum dose within an OAR will occur in the N beam intersection volume within that OAR. Therefore, beam orientations which minimize N BIV within an OAR also minimize high dose regions within that OAR (as demonstrated for the rectum in prostate IMRT). It was also demonstrated that any point of a DVH can be decomposed into a superposition of volume-weighted BIV components. Building on that work, this chapter investigates the optimization of N, N-1, N-2, etc. BIV components to reduce all dose regions in the DVH of an OAR.

4.2.2 Feasible Beam Orientation Search Space

The BOO algorithm presented in this chapter interfaced to the Pinnacle^3 research version 8.1r (Philips Radiation Oncology Systems, Milpitas, CA, USA) treatment planning system to obtain Cartesian coordinates of the region-of-interest (ROI) contours from patient treatment plans. A 3D patient structure matrix (voxel size of 1 mm x 1 mm x

CT slice thickness) was generated using this ROI information. Divergent ray tracing from trial beam source positions was performed through the 3D patient structure matrix. A sphere of all beam orientations (gantry, couch) pairs was pre-computed (required less than 1 second) in 1° increments and used to define a solution space from which all infeasible beam orientations were eliminated. Beam orientations entering through inferior or superior regions where computed tomographic (CT) data are not available were identified as infeasible. Beam orientations leading to mechanical gantry/couch collisions were also identified as infeasible.

4.2.3 Simulated Annealing Optimization

A simulated annealing (SA) algorithm was employed to search for the optimal set of beam orientations which minimize the BIV within a critical structure. Many previous studies have demonstrated the efficacy of the SA method for BOO in radiotherapy [12, 13, 18, 22, 23, 31, 34-36]. The SA optimization mimics the behaviour of a physical system of interacting particles that are gradually cooled, such that the system is effectively at thermal equilibrium at any time, to eventually stabilize in the ground state [45, 46]. As in a physical system, SA properly samples local minima in the search space while searching for the global minimum as the temperature is lowered to zero. In this work, 5 equiangular-spaced beams starting at 0° (5-equi) were chosen as the initial seed beam orientation set in the search space. During the optimization, the sets of beam orientations underwent random changes to explore different combinations of gantry and couch angles. To achieve this, a beam was randomly chosen from the current set and its

orientation (gantry or couch angle) was randomly changed by a positive or negative increment of $\Delta = 5°$. In this way, the SA optimization navigated away from the initial seed beam orientation set (5-equi) in the search space to sample other regions containing potentially better solutions. For $N = 5$ beams, the BIV components (N, N-1, N-2, and N-3) within an OAR (or as used in this work the 5 BIV, 4 BIV, 3 BIV, and 2 BIV components) were computed for each trial beam orientation set. The SA optimization did not include the 1 BIV component (which is associated with low dose regions within an OAR). A Metropolis probability function [45, 46] was assigned for each BIV component:

$$P_N = \begin{cases} 1, & \Delta(N) < 0 \\ \exp\left(-\dfrac{\Delta(N)}{T}\right), & otherwise \end{cases}, P_{N-1} = \begin{cases} 1, & \Delta(N-1) < 0 \\ \exp\left(-\dfrac{\Delta(N-1)}{T}\right), & otherwise \end{cases}, \text{etc.} \qquad (4.1)$$

where $\Delta(N)$, $\Delta(N-1)$, etc. is the change in the BIV component N, N-1, etc. and T is the system temperature. The trial beam orientation set was automatically accepted if P_N, P_{N-1}, etc. were unity (all BIV components went 'downhill'). However, the trial beam orientation set could still be accepted with a non-zero probability if P_N, P_{N-1}, etc. were not unity (one or more BIV components went 'uphill') which provided the algorithm with a mechanism to escape from local minima. By assigning individual probability functions for each BIV component, this method allowed for the simultaneous optimization of multiple BIV components. Note that this is not a true multi-objective function optimization process, but does suit the purpose of demonstrating the usefulness of the BIV concept to provide optimal beam orientations. The system temperature was gradually lowered according to an inverse-logarithmic cooling schedule. Therefore, as the temperature slowly decreased, the probability of accepting a trial set of beam orientations with higher BIV components was reduced. The pre-computed infeasible beam

orientations were excluded. The algorithm also excluded parallel-opposed beam orientations for IMRT and applied a minimum beam separation of 20°. Approximately five-thousand sets of beam orientations were sampled during the optimization of coplanar and non-coplanar beams.

The geometric conformity index (CI), defined as the ratio of the 5 beam intersection volume (within the target) to the target volume, was also evaluated at each iteration during the optimization. The geometric CI is analogous to the radiation CI [47], which has been proposed to quantify the level of target conformity of a treatment plan, except here the geometric CI evaluates the 5 BIV instead of the 95% isodose volume. In this work, it was observed that by using non-coplanar (instead of coplanar) beam orientations, larger variations in the geometric CI were produced. Based on studying the variation of the geometric CI as a function of beam orientation, a trial beam orientation set was excluded if the geometric CI increased by more than 10% from the value using 5 equiangular-spaced beams. A maximum deviation of 10% was chosen to produce a reasonable balance between allowing the flexibility of non-coplanar beams while preserving target conformity. This provided a mechanism to improve critical structure sparing (by optimizing BIV) and also account for target conformity. A potential future implementation may include the geometric CI as a parameter of the optimization, similar to the PTV coverage term in the Schreibmann *et al.* [15] geometric cost function, and will be discussed in Chapter 6.

4.2.4 Calculation of BIV Components and CI

For each trial beam orientation in the SA optimization, a Beams-Eye-View (BEV) image of the target(s) was produced. Each BEV was divided into a grid (resolution of 1.6 mm x 1.6 mm at isocentre) of incident ray lines and divergent ray tracing was performed through the BEV to generate a 3D matrix which modeled the geometrically diverging primary beam in 3D space. The coincidence volume of N, N-1, N-2, and N-3 beams in the SA trial beam orientation set and an OAR was calculated, defined as the N, N-1, N-2, and N-3 beam intersection volume (BIV) components. In a similar manner, the geometric CI was calculated using the ratio of the N beam coincidence volume to the PTV.

4.2.5 Implementation on Clinical Examples

The SA algorithm was implemented on 3 treatment sites: (1) a gastric cancer patient with prescription dose of 50.4 Gy in 28 fractions and OARs included liver, spinal cord, and left and right kidneys, (2) a localized prostate cancer patient following the RTOG P-0126 protocol with prescription dose of 79.2 Gy in 44 fractions where the Planning Target Volume (PTV) included the proximal bilateral seminal vesicles and OARs included left and right femoral heads, bladder, and rectum. (3) two oropharyngeal cancer patients following the RTOG H-0022 protocol with prescription dose of 66 Gy in 30 fractions, where PTV66 included the gross tumour and lymph node metastasis, and PTV54 included the bilateral neck lymph nodes (receiving 54 Gy), and OARs included glottic larynx, brainstem, spinal cord, mandible, and left and right parotid glands. The first oropharyngeal cancer case was a stage-III squamous cell carcinoma of the left tonsil

while the second case was a stage-IV squamous cell carcinoma of the left tonsil where the primary was extending to the nasopharynx.

All SA optimizations were performed using BIV components that contributed at least 10% to the combined volume of all BIV components in the SA initial beam arrangement (5-equi). This excluded the optimization of volumetrically small BIV components which did not play an important role as surrogates for the high-to-medium doses in an OAR. The inclusion of volumetrically large, 'higher order' BIV components (i.e. 5 BIV, 4 BIV, 3 BIV, and 2 BIV) allowed the optimization to reduce the volume of more important 'higher order' BIV components at the expense of 'lower order' BIV components (i.e. 1 BIV). This is analogous to reducing volumes of high dose within an OAR at the expense of an increase in the volume of low dose within the OAR. For instance, in the prostate and stage-III oropharyngeal cases, the optimal plans improved the dose distributions in the rectum and contralateral parotid gland by shifting BIV away from the 5, 4, and 3 BIV to the initially small 2 BIV. For each case, an optimization was performed separately on the highest order (usually $N = 5$) BIV component (except in the gastric case where the 3 BIV was the highest order non-zero BIV component) since one would expect this component to have the greatest potential to produce the highest dose region in the OAR and, therefore, predominately contribute to the dose distribution. However, since other BIV components (N-1, N-2, and N-3) can also substantially contribute to the combined BIV volume, separate optimizations were performed by including successive BIV components (N, N-1, N-2, etc.) to demonstrate the resulting improvements in the DVH and show that the dose distribution within an OAR is

correlated to the superposition of BIV components. Optimizations using non-coplanar beams were performed to provide greater flexibility in minimizing BIV, which was especially useful when simultaneously minimizing several BIV components (N, N-1, N-2, etc.) for the oropharyngeal cases. Pugachev *et al.* also demonstrated the usefulness of non-coplanar beams for head-and-neck IMRT [31].

For each case, an IMRT treatment plan with 5 optimized beam orientations (5-opt) selected by the algorithm was compared to IMRT plans with 5, 7, and 9 equiangular-spaced beam orientations starting at 0° (5-equi, 7-equi, 9-equi). For the prostate case, the treatment plan with 5 optimized beam orientations was also compared to plans with 5 optimal equiangular-spaced beam orientations (from Chapter 2) and with the Zelefsky 5 beam orientations [48]. All IMRT plans were generated in Pinnacle^3 using direct machine parameter optimization (DMPO) with 6 MV photon beams, step-and-shoot multileaf collimator (MLC) delivery, and patient in a supine treatment position. The DMPO method in Pinnacle^3, based upon direct aperture optimization [49], includes the MLC positions and segment weights as parameters of the optimization [50]. A maximum of 100 total segments were used for each plan, and the same set of inverse planning objectives was used between the 5-opt, 5-equi, 7-equi, and 9-equi plans for a particular treatment site. The clinical objectives for each treatment site are summarized in Table 4.1. Dose-volume histograms (DVHs) for the target(s) and the OARs as well as isodose distributions were used to evaluate the quality of the plans. In the clinical cases presented in this chapter, the algorithm was used to optimize BIV within an OAR of interest (right kidney, rectum, contralateral parotid gland) as decided from clinical relevance for a

particular treatment site. In principle, the method could be used to improve sparing of several OARs in a treatment plan by optimizing BIV in each OAR as will be discussed in Chapter 6.

Table 4.1: Clinical objectives for each treatment site.

Tx Site	Structure	Objective
Gastric	PTV	V50.4 $\geq$ 95%
		V53.9 = 0%
	Rt Kidney	V20 < 60%
	Lt Kidney	V20 < 60%
	Liver	V30 < 60%
	Spinal Cord	D_{max} < 45 Gy
Prostate	PTV	V79.2 $\geq$ 98%
		V84.7 < 2%
	Rectum	V75 < 15%
		V70 < 25%
		V65 < 35%
		V60 < 50%
	Bladder	V80 < 15%
		V75 < 25%
		V70 < 35%
		V65 < 50%
	Lt Femur	D_{max} < 54 Gy
	Rt Femur	D_{max} < 54 Gy
Oropharynx	PTV66	V66 $\geq$ 95%
		V72.6 < 20%
	PTV54	V54 $\geq$ 95%
		V59.4 < 20%
	Glottic Larynx	V50 < 66%
	Brainstem	D_{max} < 54 Gy
	Spinal Cord	D_{max} < 45 Gy
	Mandible	D_{max} < 70 Gy
	Unspecified Tissue	V72.6 < 1%
	Lt Parotid	V30 < 50%
	Rt Parotid	V30 < 50%

4.2.6 Uncertainty Analysis

To determine whether the use of a random search in the SA algorithm may introduce additional statistical uncertainty, the algorithm's statistical uncertainty was examined using the Stage-III oropharyngeal case. This case exhibited the most complex, irregularly-shaped total PTV and the largest variations of the geometric conformity index using non-coplanar beams. It was also dosimetrically challenging since none of the standard 5, 7, and 9 equiangular-spaced beam arrangements were able to achieve a mean dose of less than 26 Gy to the contralateral parotid (as specified by the RTOG H-0022 protocol). To test the algorithm for any additional statistical uncertainty, ten BIV optimizations (including the 5, 4, and 3 BIV components within the contralateral parotid) with five non-coplanar beams were performed using different seeds of the random number generator. An IMRT plan was generated for each of the ten sets of optimal beam orientations to evaluate the quality of the dose distribution compared to standard plans (5-equi, 7-equi, and 9-equi).

4.3 Results

4.3.1 Gastric Cancer

Table 4.2 provides the BIV components within the right kidney (the closest OAR), which is in close proximity to the PTV (approximately 0.7 cm at closest approach), using 5 equiangular-spaced beams (5-equi). Optimizations were not performed using the 5 BIV and 4 BIV since each of these components contributed less

than 10% (i.e. 0% and 0.6%) to the combined volume of all BIV components in the SA initial beam arrangement (5-equi). When the algorithm minimized the 3 BIV (Table 4.2) within the right kidney, the following 5 optimal gantry angles were obtained: 92°, 134°, 236°, 293°, and 335° (the IMRT plan generated with these 5 optimal gantry angles was called 5-opt-3BIV). When the algorithm simultaneously minimized the 3 BIV and 2 BIV (Table 4.2), the following 5 optimal gantry angles (5-opt-32BIV) were obtained: 102°, 144°, 256°, 303°, and 350°. The isodose distributions for the plans with 5 optimized beams (5-opt-32BIV) and 5 equiangular-spaced beams are shown in Figure 4.1. The 5-opt-32BIV plan reduced the right kidney V 20 Gy by 41.1 %, 32.1 %, and 29.5 % compared to 5, 7, and 9 equiangular-spaced beam plans, respectively. The DVHs for the right kidney and PTV using 5 optimized beams (5-opt-3BIV, 5-opt-32BIV) compared to 5, 7, 9 equiangular-spaced beams are shown in Figure 4.2. The PTV metrics demonstrated little variation between all plans (V 50.4 Gy of 99.9 - 100.0 %, mean dose of 51.4 ± 0.2 Gy - 51.8 ± 0.2 Gy, and V 53.9 Gy of 0 %). The liver, left kidney, and spinal cord metrics also demonstrated little variation between all plans. No further minimization of the 3 BIV and 2 BIV was observed when using non-coplanar beams.

Table 4.2: The BIV components within the right kidney, rectum, and contralateral parotid for all plans in the gastric, prostate, and oropharynx cases.

Tx Site (OAR)	Plan	5 BIV (cc)	4 BIV (cc)	3 BIV (cc)	2 BIV (cc)
Gastric	5-equi	0.0	0.6	9.5	86.8
(Rt. Kidney)	5-opt-3BIV	0.0	0.0	0.7	14.6
	5-opt-32BIV	0.0	0.0	0.8	5.3
Prostate	5-equi	24.1	11.1	8.0	2.8
(Rectum)	5-equi-opt	18.2	16.0	8.4	3.4
	Zelefsky	20.3	9.1	11.2	5.1
	5-opt-5BIV	16.0	19.5	7.0	3.7
	5-opt-54BIV	17.9	9.3	12.8	5.6
	5-opt-543BIV	19.7	9.0	6.7	7.1
Stage-III					
Oropharynx	5-equi	11.9	9.7	7.9	1.8
(Contra Parotid)	5-opt-5BIV	8.7	10.2	8.8	3.3
	5-opt-54BIV	9.4	5.7	9.4	6.0
	5-opt-copl-543BIV	10.0	7.1	6.8	3.8
	5-opt-non-543BIV	11.2	2.3	1.5	5.3
Stage-IV					
Oropharynx	5-equi	6.3	3.4	3.5	11.5
(Contra Parotid)	5-opt-5BIV	5.0	3.7	2.6	4.4
	5-opt-52BIV	5.1	3.2	2.1	4.2
	5-opt-copl-5432BIV	5.2	3.1	2.0	3.7
	5-opt-non-5432BIV	5.7	1.7	1.1	1.9

Figure 4.1: The IMRT dose distributions for the gastric case using (a) 5 equiangular-spaced beams (b) 5 optimized beams (5-opt-32BIV). The 47.9 Gy (95%), 45 Gy, 30 Gy, and 20 Gy isodose lines are displayed. OARs including liver, spinal cord, and left and right kidneys are shown.

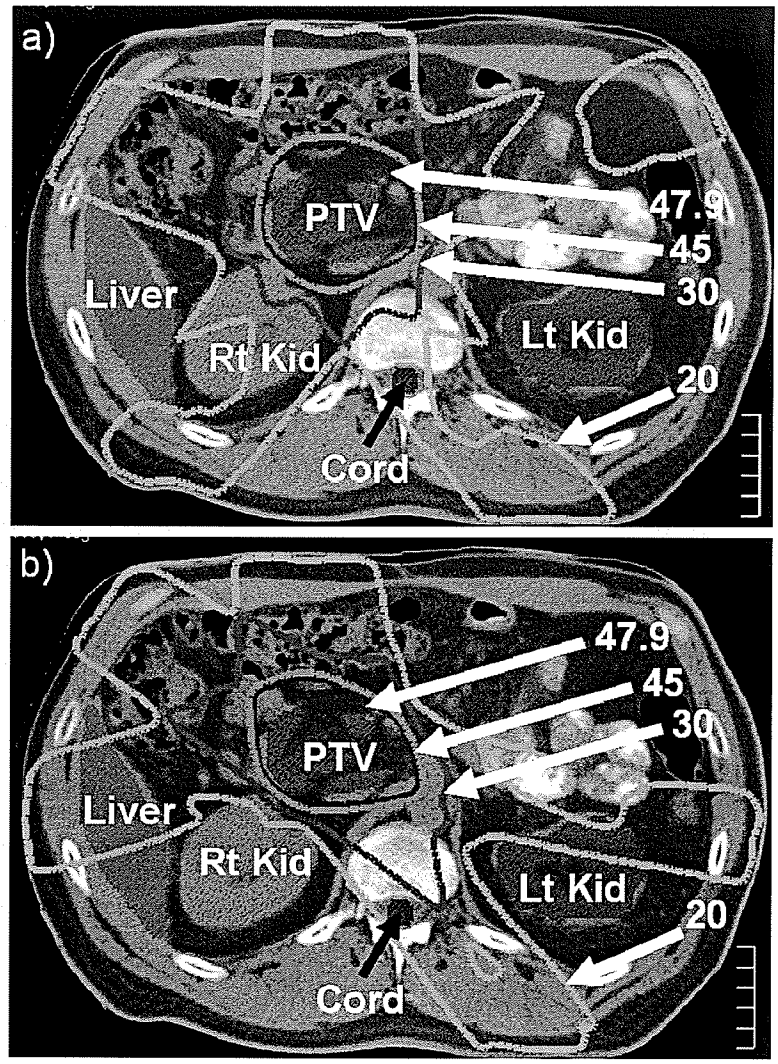

Figure 4.2: The gastric case dose-volume histograms of the right kidney and PTV using 5 optimized beams (5-opt-3BIV, 5-opt-32BIV) compared to 5, 7, 9 equiangular-spaced beams.

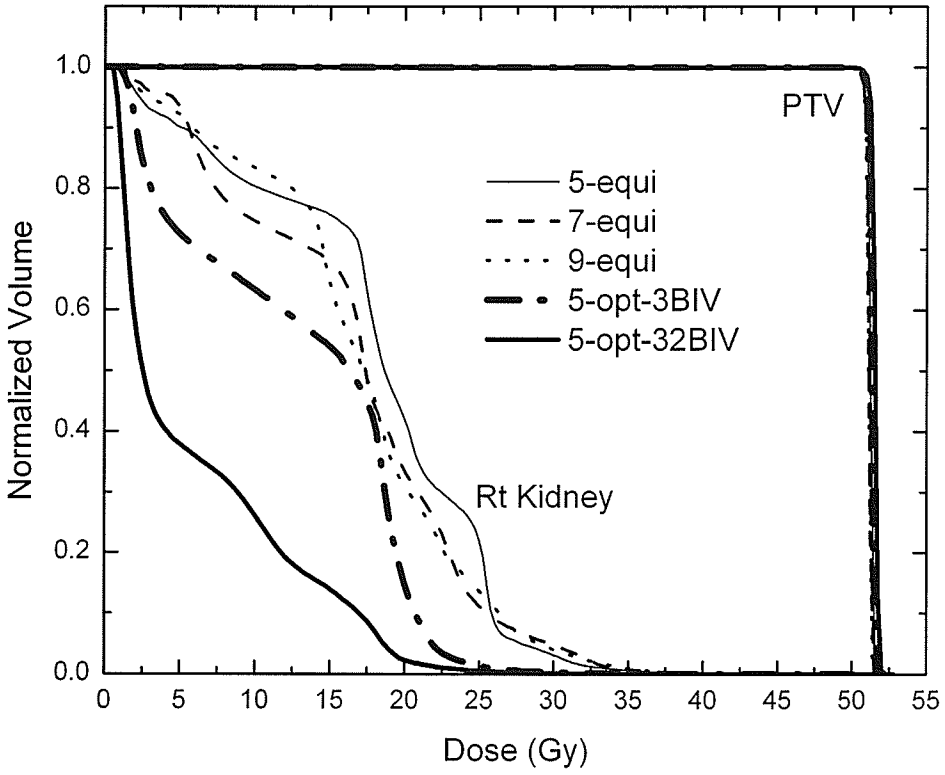

4.3.2 Prostate Cancer

Table 4.2 provides the BIV components within the rectum using 5 equiangular-spaced beams (5-equi), 5 optimal equiangular-spaced beams starting at 20° (5-equi-opt), and the Zelefsky gantry angles. Optimizations were not performed using the 2 BIV since this component contributed less than 10% (i.e. from Table 4.2, the 2 BIV (2.8 cc) is only 6 % of the total BIV in the 5-equi plan) to the combined volume of all BIV components

in the SA initial beam arrangement (5-equi). When the algorithm minimized the 5 BIV (Table 4.2) within the rectum, the following 5 optimal gantry angles (5-opt-5BIV) were obtained: 52°, 129°, 206°, 268°, and 330°. When the 5 BIV and 4 BIV were simultaneously minimized (Table 4.2), the following 5 optimal gantry angles (5-opt-54BIV) were obtained: 47°, 94°, 186°, 253°, and 315°. When the algorithm simultaneously minimized the 5 BIV, 4 BIV, and 3 BIV (Table 4.2), the following 5 optimal gantry angles (5-opt-543BIV) were obtained: 37°, 84°, 131°, 243°, and 285°. The rectal V 75 Gy, V 70 Gy, V 65 Gy, and V 60 Gy were reduced by 3.9 %, 6.2 %, 8.1 %, and 10.6 %, respectively in the 5-opt-543BIV plan compared to the 5-equi plan. The DVHs for the rectum and PTV comparing the plans with 5 optimized beams (5-opt-5BIV, 5-opt-54BIV, 5-opt-543BIV) to the 5-equi plan are shown in figure 4.3. The DVHs for the rectum and PTV comparing the 5-opt-543BIV, 5-equi-opt, and Zelefsky plans to plans with 5, 7, 9 equiangular-spaced beams starting at 0° are shown in figure 4.4. The PTV metrics demonstrated little variation between all plans (V 79.2 Gy of 99.1 - 99.7 %, mean dose of 80.8 ± 0.4 Gy - 81.2 ± 0.4 Gy, and V 84.7 Gy of 0 %). The bladder and femoral head metrics also demonstrated little variation between all plans. No further minimization of the 5 BIV, 4 BIV, and 3 BIV was observed when using non-coplanar beams.

Figure 4.3: The prostate case dose-volume histograms of the rectum and PTV using 5 optimized beams (5-opt-5BIV, 5-opt-54BIV, 5-opt-543BIV) compared to 5 equiangular-spaced beams (5-equi).

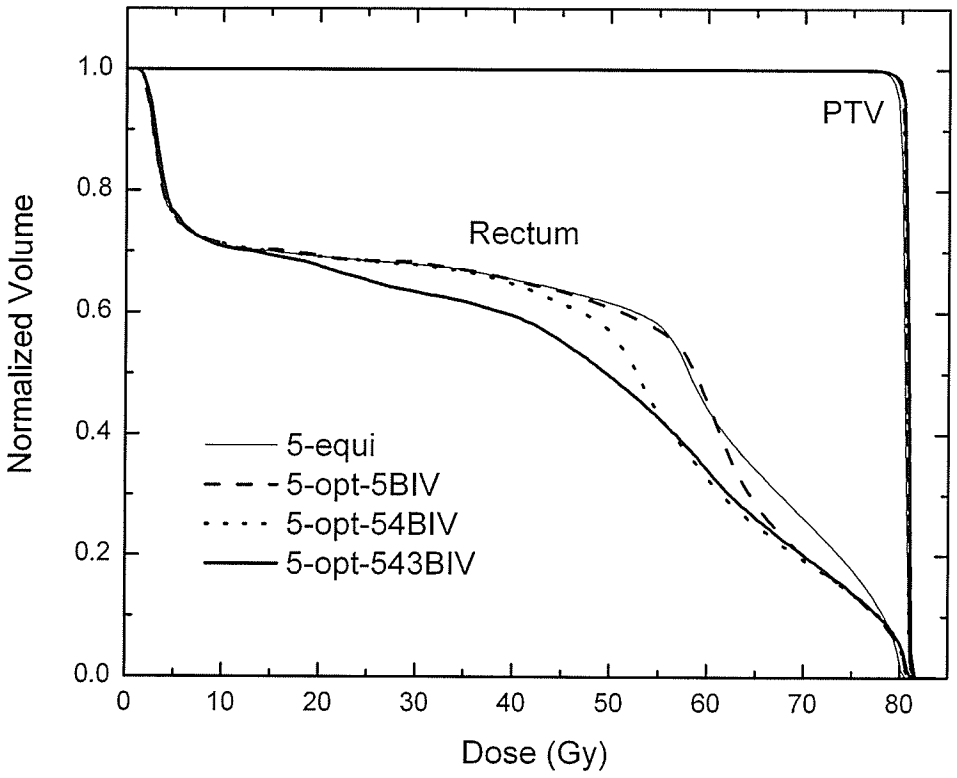

Figure 4.4: The prostate case dose-volume histograms of the rectum and PTV using 5 optimized beams (5-opt-543BIV) compared to 5, 7, 9 equiangular-spaced beams starting at 0° (5-equi, 7-equi, 9-equi), 5 optimal equiangular-spaced beams starting at 20° (5-equi-opt), and the Zelefsky gantry angles.

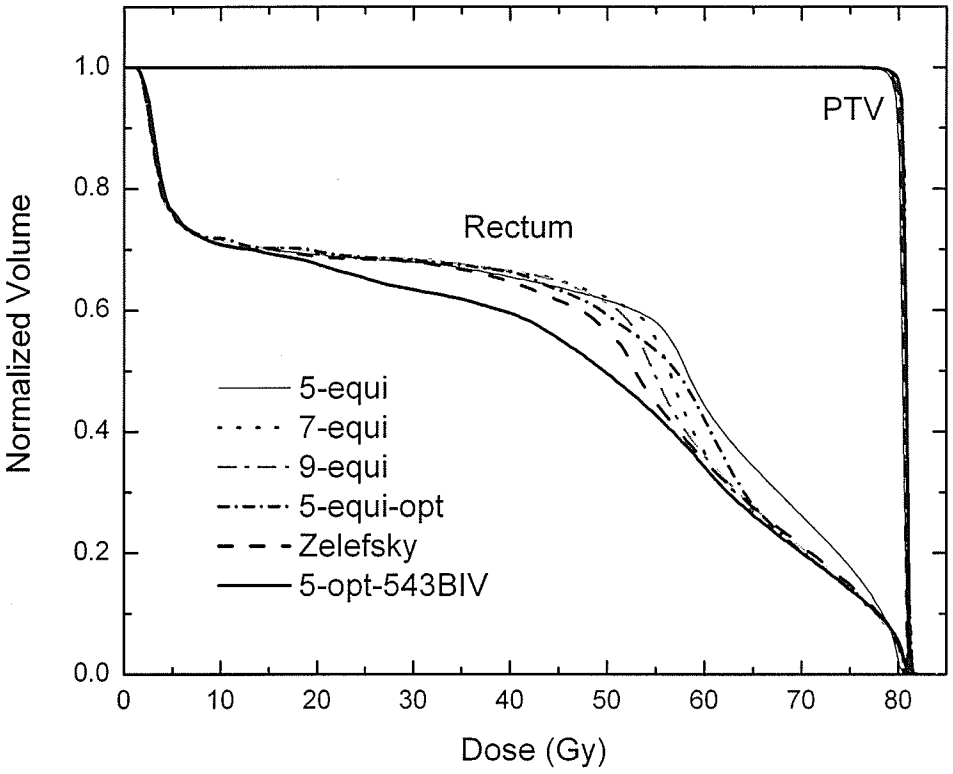

4.3.3 Oropharyngeal Cancer

Stage-III:

Table 4.2 provides the BIV components within the contralateral parotid gland using 5 equiangular-spaced beams (5-equi). Optimizations were not performed using the 2 BIV since this component contributed less than 10% (i.e. from Table 4.2, the 2 BIV (1.8 cc) is only 6 % of the total BIV in the 5-equi plan)) to the combined volume of all

BIV components in the SA initial beam arrangement (5-equi). When the algorithm minimized the 5 BIV (Table 4.2) within the contralateral parotid, the following 5 optimal gantry angles (5-opt-5BIV) were obtained: 57°, 144°, 211°, 303°, and 355°. When the 5 BIV and 4 BIV were simultaneously minimized (Table 4.2), the following 5 optimal gantry angles (5-opt-54IV) were obtained: 12°, 54°, 156°, 213°, and 300°. The algorithm was also used to simultaneously minimize the 5 BIV, 4 BIV, and 3 BIV components (Table 4.2), using 5 optimal coplanar (5-opt-copl-543BIV) beams and 5 optimal non-coplanar (5-opt-non-543BIV) beams. The optimal coplanar beam orientations (gantry angles) obtained were 3°, 45°, 112°, 204°, and 246° while the optimal non-coplanar beam orientations (gantry°, couch°) obtained were: (15°, 340°), (112°, 340°), (211°, 25°), (219°, 315°), (233°, 20°). The isodose distributions for the plans with 5 optimized non-coplanar beams (5-opt-non-543BIV) and 5 equiangular-spaced beams are shown in Figure 4.5. Tables 4.3a and 4.3b summarize the clinical metrics of the targets and OARs for each treatment plan.

Figure 4.5: The IMRT dose distributions for the stage-III oropharyngeal case using (a) 5 equiangular-spaced beams (b) 5 optimized non-coplanar beams (5-opt-non-543BIV). The 62.7 Gy (95% of PTV66), 51.3 Gy (95% of PTV54), 45 Gy, and 30 Gy isodose lines are displayed. OARs including mandible, spinal cord +5mm, and left and right parotid glands are shown.

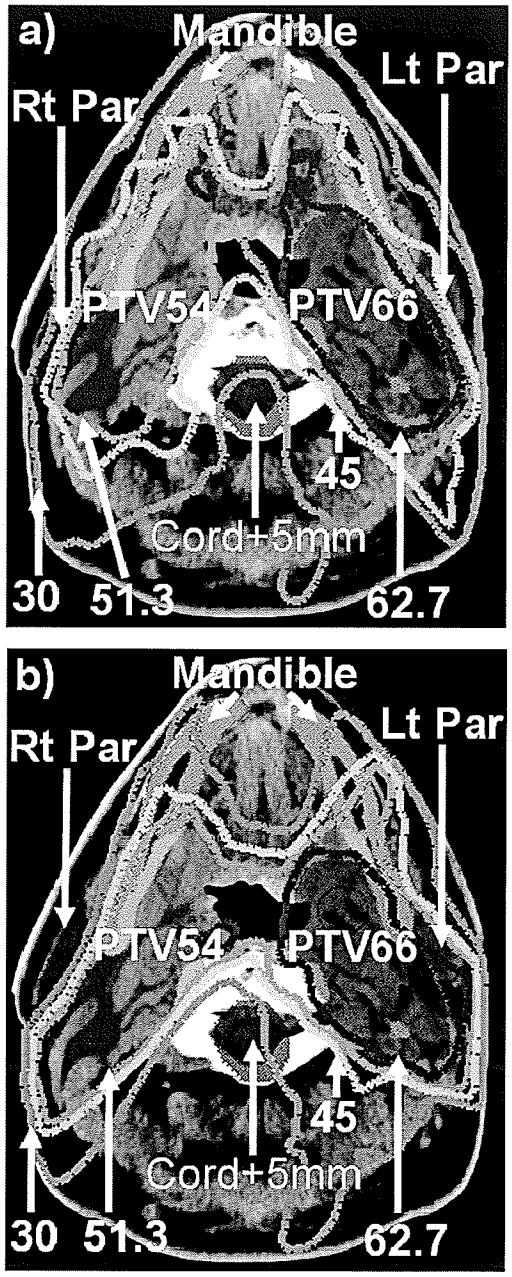

Table 4.3a: Clinical target metrics for each plan in the stage-III oropharyngeal case.

	PTV66 V66 (%)	PTV66 V72.6 (%)	PTV66 Mean (Gy)	PTV54 V54 (%)	PTV54 V59.4 (%)	PTV54 Mean (Gy)
5-equi	97.6	5.3	70.4 ± 1.8	98.1	17.0	58.3 ± 2.1
7-equi	98.2	2.5	70.2 ± 1.5	98.9	10.5	58.0 ± 1.8
9-equi	98.5	0.2	69.7 ± 1.3	98.8	8.3	57.7 ± 1.8
5-opt-5BIV	95.7	1.6	69.1 ± 1.7	96.9	6.9	57.3 ± 2.0
5-opt-54BIV	96.6	9.6	70.3 ± 2.1	97.8	12.8	58.0 ± 2.1
5-opt-copl-543BIV	95.1	16.8	70.5 ± 2.5	98.0	19.4	58.3 ± 2.2
5-opt-non-543BIV	95.0	6.4	69.9 ± 2.2	96.6	18.2	57.8 ± 2.4

Table 4.3b: Clinical organ-at-risk metrics for each plan in the stage-III oropharyngeal case. Ipar (Ipsilateral parotid), Cpar (Contralateral parotid), Cord (Spinal cord+5mm).

	Larynx V50 (%)	Brainstem Max (Gy)	Cord Max (Gy)	Mandible Max (Gy)	Ipar V30 (%)	Ipar Mean (Gy)	Cpar V30 (%)	Cpar Mean (Gy)
5-equi	26.5	30.2	38.1	70.3	46.9	31.7	41.0	29.4
7-equi	30.0	20.7	36.2	70.4	46.2	31.6	39.1	27.8
9-equi	44.5	25.6	34.6	70.1	43.8	31.1	40.7	28.0
5-opt-5BIV	38.4	26.4	38.4	70.7	43.9	30.4	36.3	26.6
5-opt-54BIV	34.3	30.2	38.5	70.2	49.4	32.5	33.5	26.5
5-opt-copl-543BIV	11.6	29.1	42.1	70.8	49.2	32.3	34.8	26.7
5-opt-non-543BIV	7.3	30.1	44.8	70.9	44.7	33.0	32.1	25.3

Stage-IV:

Table 4.2 provides the BIV components within the contralateral parotid gland using 5 equiangular-spaced beams (5-equi). When the algorithm minimized the 5 BIV (Table 4.2) within the contralateral parotid, the following 5 optimal gantry angles (5-opt-5BIV) were obtained: 2°, 49°, 141°, 208°, and 300°. When the 5 BIV and 2 BIV (the largest BIV components in the SA initial beam arrangement, i.e. 5-equi) were simultaneously minimized (Table 4.2), the following 5 optimal gantry angles (5-opt-52BIV) were obtained: 42°, 139°, 191°, 298°, and 340°. The algorithm was also used to simultaneously minimize all the BIV components (Table 4.2), i.e. 5 BIV, 4 BIV, 3 BIV, and 2 BIV, using 5 optimal coplanar (5-opt-copl-5432BIV) beams and 5 optimal non-coplanar (5-opt-non-5432BIV) beams. The optimal coplanar beam orientations (gantry angles) obtained were 37°, 139°, 191°, 298°, and 340° while the optimal non-coplanar beam orientations (gantry°, couch°) obtained were: (130°, 0°), (12°, 60°), (349°, 95°), (226°, 40°), (333°, 0°). The DVHs for the contralateral parotid gland, PTV54, and PTV66 using 5 optimized coplanar beams (5-opt-5BIV, 5-opt-52BIV, 5-opt-copl-5432BIV), 5 optimized non-coplanar beams (5-opt-non-5432BIV), compared to 5, 7, and 9 equiangular-spaced beams are shown in Figure 4.6. Tables 4.4a and 4.4b summarize the clinical metrics of the targets and OARs for each treatment plan.

Figure 4.6: The stage-IV oropharyngeal dose-volume histograms of the contralateral parotid gland, PTV54, and PTV66 using 5 optimized coplanar beams (5-opt-5BIV, 5-opt-52BIV, 5-opt-copl-5432BIV), 5 optimized non-coplanar beams (5-opt-non-5432BIV), compared to 5, 7, and 9 equiangular-spaced beams.

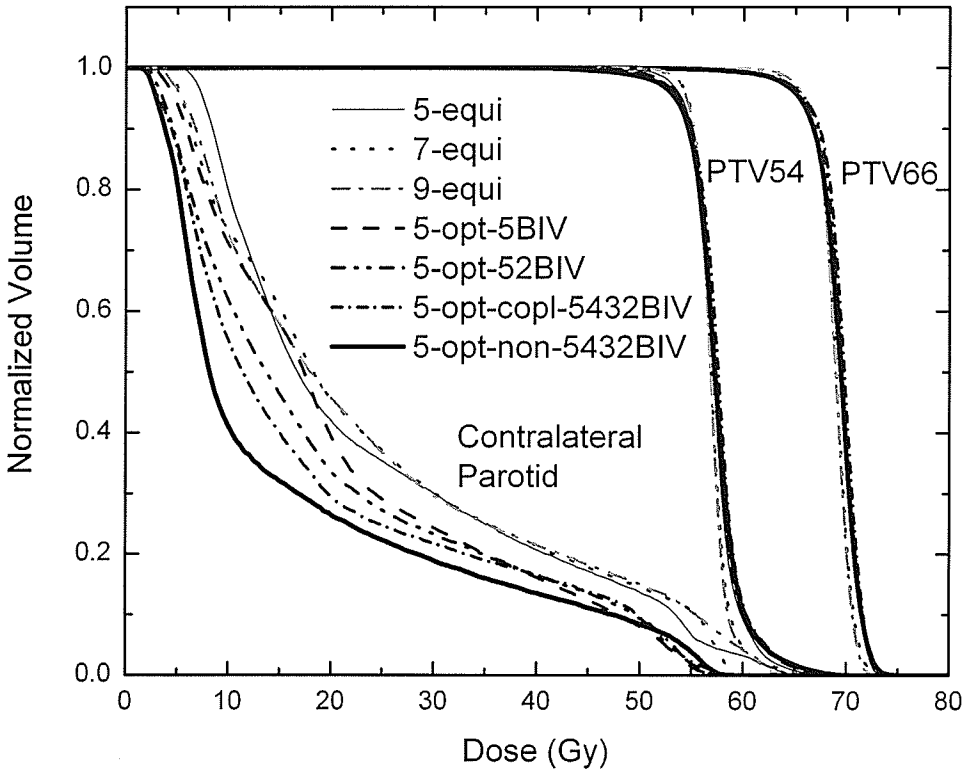

Table 4.4a: Clinical target metrics for each plan in the stage-IV oropharyngeal case.

	PTV66 V66 (%)	PTV66 V72.6 (%)	PTV66 Mean (Gy)	PTV54 V54 (%)	PTV54 V59.4 (%)	PTV54 Mean (Gy)
5-equi	95.0	5.3	69.8 ± 2.1	96.2	16.9	57.9 ± 2.3
7-equi	95.8	1.0	69.2 ± 1.7	98.0	8.4	57.4 ± 1.8
9-equi	95.9	0.4	69.2 ± 1.6	98.0	7.0	57.3 ± 1.7
5-opt-5BIV	95.0	4.8	69.6 ± 2.2	95.7	16.1	57.8 ± 2.5
5-opt-52BIV	95.6	4.2	69.7 ± 2.1	95.3	15.6	57.7 ± 2.5
5-opt-copl-5432BIV	95.7	4.1	69.9 ± 2.1	95.3	19.8	58.0 ± 2.7
5-opt-non-5432BIV	95.1	4.4	69.6 ± 2.2	95.0	18.9	57.8 ± 2.8

Table 4.4b: Clinical organ-at-risk metrics for each plan in the stage-IV oropharyngeal case. Ipar (Ipsilateral parotid), Cpar (Contralateral parotid), Cord (Spinal cord+5mm).

	Larynx V50 (%)	Brainstem Max (Gy)	Cord Max (Gy)	Mandible Max (Gy)	Ipar V30 (%)	Ipar Mean (Gy)	Cpar V30 (%)	Cpar Mean (Gy)
5-equi	0.6	50.2	40.1	70.1	44.1	32.4	30.5	24.4
7-equi	8.9	49.6	37.6	69.6	44.3	32.2	30.5	24.5
9-equi	7.1	47.7	37.4	69.7	41.5	31.7	30.1	24.6
5-opt-5BIV	16.9	51.3	40.2	71.8	44.7	31.4	24.7	21.6
5-opt-52BIV	21.4	50.8	41.1	71.2	44.5	32.4	23.6	20.0
5-opt-copl-5432BIV	14.0	51.6	41.5	71.0	45.0	32.3	22.0	18.9
5-opt-non-5432BIV	0.4	52.1	43.6	71.8	44.3	32.0	19.3	16.6

4.3.4 Uncertainty Results

Table 4.5 provides ten sets of optimal beam orientations (gantry°, couch°) for the Stage-III oropharyngeal case. The BIV components within the contralateral parotid using 5 equiangular-spaced beams (5-equi) and the ten sets of optimal beam orientations are compared in Table 4.6. The algorithm minimized the 5, 4, and 3 BIV at the expense of the 2 BIV (which was initially small in the 5-equi plan) to produce each set of optimal beam orientations. A small amount of statistical noise was observed over the ten runs, however, the average reductions in 5, 4, and 3 BIV were 1.4 ± 0.6 cc, 6.3 ± 1.0 cc, and 4.0 ± 1.4 cc at the expense of an average increase in the 2 BIV of 6.6 ± 1.9 cc compared to the 5-equi plan (Table 4.6). The dosimetric evaluation of the ten optimal plans compared to standard plans with 5, 7, and 9 equiangular-spaced beams is summarized in Table 4.7. The ten 5-opt-non-543BIV plans achieved contralateral parotid mean doses near or below the 26 Gy objective specified by the RTOG H-0022 protocol, with an average reduction in contralateral parotid mean dose of 3.2 Gy, 1.6 Gy, and 1.8 Gy (standard deviation of 0.5 Gy) compared to the 5-equi, 7-equi, and 9-equi plans. The optimized plans also exhibited, on average, more PTV dose inhomogeneity. Nonetheless, the PTV and critical structure dose metrics satisfied protocol requirements in all ten plans. In summary, the performance of the SA algorithm in consistently producing optimal beam orientations providing dosimetric improvements in critical structure sparing provides evidence that the approach is robust.

Table 4.5: Ten sets of optimal beam orientations (gantry°, couch°) for the Stage-III oropharyngeal case obtained by performing BIV optimizations with ten different seeds of the random number generator.

Run	Optimal Beam Orientations (gantry°, couch°)
1	(15, 340),(112, 340),(211, 25),(219, 315),(233, 20)
2	(17, 10),(144, 45),(211, 330),(238, 40),(325, 330)
3	(3, 275),(45, 45),(132, 350),(149, 5),(211, 345)
4	(8, 310),(25, 345),(149, 45),(227, 45),(231, 10)
5	(122, 15),(211, 330),(233, 35),(234, 0),(325, 265)
6	(20, 5),(33, 30),(37, 340),(164, 340),(226, 305)
7	(20, 340),(22, 65),(136, 330),(214, 0),(228, 330)
8	(30, 15),(72, 30),(179, 350),(211, 340),(308, 340)
9	(38, 50),(60, 0),(147, 25),(211, 325),(234, 25)
10	(140, 5),(212, 355),(234, 25),(328, 95),(341, 300)

Table 4.6: The BIV components within the contralateral parotid using 5 equiangular-spaced beams (5-equi) and the ten sets of optimal beam orientations. The algorithm minimized the 5, 4, and 3 BIV at the expense of the 2 BIV (which was initially small in the 5-equi plan) to produce each set of optimal beam orientations.

Plan	5 BIV (cc)	4 BIV (cc)	3 BIV (cc)	2 BIV (cc)
5-equi	11.9	9.7	7.9	1.8
5-opt-non-543BIV				
Run 1	11.2	2.3	1.5	5.3
Run 2	11.0	1.8	4.0	10.9
Run 3	10.1	4.3	6.8	8.5
Run 4	10.5	3.5	3.4	5.5
Run 5	10.1	3.4	4.5	7.6
Run 6	10.8	2.7	2.5	10.6
Run 7	10.2	3.5	4.4	9.9
Run 8	11.2	4.4	4.2	9.1
Run 9	9.5	3.7	4.9	7.9
Run 10	10.8	4.8	3.0	8.5
Average	10.5 ± 0.6	3.4 ± 1.0	3.9 ± 1.4	8.4 ± 1.9

Table 4.7: The dosimetric evaluation of the ten optimal plans compared to standard plans with 5, 7, and 9 equiangular-spaced beams. Cpar (Contralateral parotid).

Plan	PTV66 Mean (Gy)	PTV54 Mean (Gy)	Cpar Mean (Gy)
5-equi	70.4 ± 1.8	58.3 ± 2.1	29.4
7-equi	70.2 ± 1.5	58.0 ± 1.8	27.8
9-equi	69.7 ± 1.3	57.7 ± 1.8	28.0
5-opt-non-543BIV			
Run 1	69.9 ± 2.2	57.8 ± 2.4	25.3
Run 2	70.4 ± 2.1	58.4 ± 2.4	26.8
Run 3	70.1 ± 1.8	57.7 ± 2.3	25.6
Run 4	69.7 ± 2.4	58.1 ± 2.5	26.2
Run 5	70.3 ± 2.4	58.2 ± 2.2	25.9
Run 6	70.5 ± 2.5	58.5 ± 2.5	26.7
Run 7	70.5 ± 2.2	58.2 ± 2.3	26.5
Run 8	70.2 ± 2.6	57.9 ± 2.3	26.1
Run 9	70.4 ± 2.4	58.3 ± 2.6	26.2
Run 10	69.8 ± 1.7	58.0 ± 2.1	26.7
Average	70.2 ± 2.2	58.1 ± 2.4	26.2 ± 0.5

4.4 Discussion

The premise of minimizing BIV components within critical structures, thereby improving sparing, is an intuitively simple concept. A strong correlation between rectal dose and the BIV was demonstrated in Chapter 3 for prostate IMRT. The current chapter demonstrates for several IMRT treatment sites and multiple BIV components that the BIV is a surrogate for dose. Minimization of BIV, a geometric parameter, within critical structures is shown to translate into a reduction in dose within those structures and therefore improve sparing. This improvement demonstrates that reliance in the ability to

highly modulate the intensity of the radiation beams alone does not negate the importance of optimizing beam orientations. The proposed method automatically selects beam orientations which improve the ability of the IMRT optimization to find better solutions, as demonstrated by increased critical structure sparing. The algorithm was implemented on 4 clinical cases (gastric, prostate, oropharyngeal stage-III and -IV) to demonstrate its usefulness.

In the gastric case, with the use of 5 optimized gantry angles, substantial sparing of the right kidney (compared to the plan with 5 equiangular-spaced beams) was demonstrated. In fact, the 5-opt-32BIV plan produced far superior right kidney sparing than plans using standard clinical beam arrangements (5, 7, and 9 equiangular-spaced beams) without compromising any plan metrics for target coverage and sparing of other critical structures or changing any dose objectives in the plans. It is important to note that simultaneously minimizing the 3 BIV and 2 BIV produced far more right kidney sparing than by only minimizing 3 BIV. This is counter-intuitive since one would expect the 3 BIV to have a greater potential than the 2 BIV to produce the highest dose region in the right kidney and, therefore, predominately contribute to the dose distribution. However, since the 2 BIV was volumetrically much larger than the 3 BIV, it produced a significant contribution to the right kidney dose distribution.

In the prostate case, the use of 5 optimized gantry angles (through the simultaneous minimization of the rectal 5 BIV, 4 BIV, and 3 BIV) considerably improved rectal sparing in the moderate and high dose regions of the DVH with no

compromise in target coverage compared to the plan with 5 equiangular-spaced beams. The minimization of the rectal 5 BIV reduced the high dose region in the rectal DVH. This result is consistent with Chapter 3 which demonstrated a strong correlation between minima in rectal 5 BIV and minima in rectal V 75 Gy and V 70 Gy. The simultaneous minimization of the rectal 5 BIV and 4 BIV reduced a larger portion of the high dose region in the rectal DVH while the simultaneous minimization of the rectal 5 BIV, 4 BIV, and 3 BIV reduced the entire high dose region as well as moderate dose regions in the rectal DVH. The improvement in rectal DVH by including successive BIV components in the optimization emphasizes that the dose distribution within a critical structure is the superposition of BIV components as was demonstrated in Chapter 3. It is interesting to observe that the optimal gantry angles produced by simultaneously minimizing the rectal 5 BIV and 4 BIV are very similar to the Zelefsky gantry angles except the Zelefsky gantry 105° is replaced by gantry 94°. The rectal DVH of the 5-opt-54BIV plan is superior to the Zelefsky plan in the high dose region which may be the result of this lateral beam. In fact, all the optimal plans (5-opt-5BIV, 5-opt-54BIV, 5-opt-543BIV) indicated that a lateral or near-lateral beam was highly important (optimal) for rectal sparing. Other studies using different BOO techniques [3, 31, 38], including Chapters 2 and 3, have also indicated that a lateral or near-lateral beam plays an important role in the optimization of prostate IMRT and this topic will be further discussed in Chapter 5. Although the complete gantry and couch angle space was available to the algorithm in the prostate case, no further minimization of the 5 BIV, 4 BIV, and 3 BIV was achieved using non-coplanar beams. This indicates that the 3D anatomic geometry of the rectum with respect to the PTV favors coplanar beam orientations. This result is consistent with

Pugachev *et al.* [31] which demonstrated that little benefit can be gained by optimizing non-coplanar beam orientations in prostate IMRT.

In both oropharyngeal cases, the 5 optimized beam orientations produced improved contralateral parotid sparing without compromising any RTOG H-0022 protocol metrics for target coverage and sparing of other critical structures. The most substantial sparing of the contralateral parotid gland was achieved using 5 optimized non-coplanar beam orientations. These non-coplanar beam orientations are non-intuitive and would be extremely difficult and time-consuming to manually determine. Both coplanar and non-coplanar optimized beam orientations resulted in superior contralateral parotid sparing compared to standard clinical beam arrangements of 5, 7, and 9 equiangular-spaced beams. The stage-III oropharyngeal case demonstrates the usefulness of this algorithm for optimizing beam orientations to produce a plan satisfying the RTOG H-0022 protocol when it is not possible to do so with standard beam arrangements. The H-0022 protocol specifies the mean dose to the contralateral parotid to be below 26 Gy since the mean dose is the best known predictor for the salivary function and severity of xerostomia in the parotid glands after radiotherapy [51, 52]. However, none of the standard 5, 7, and 9 equiangular-spaced beam arrangements in this case were able to satisfy this objective. With the use of 5 optimized non-coplanar beams, this objective was met, producing a mean dose in the contralateral parotid of 25.3 Gy. The stage-III oropharyngeal case also demonstrated an increase in the V 72.6 Gy of the PTV66 for the 5-opt-copl-543BIV plan, which indicated the presence of larger hotspots. This example illustrates the known difficulty in maintaining dose homogeneity in the target volume

when using a smaller number of beams [5], such as five. The stage-IV oropharyngeal case demonstrated the magnitude of contralateral parotid sparing that is possible by optimizing all BIV components using non-coplanar beams. The 5-opt-non-5432BIV plan substantially reduced the V 30 Gy and mean dose to the contralateral parotid by 11.2%, 11.2%, 10.8% and 7.8 Gy, 7.9 Gy, 8.0 Gy compared to the 5-equi, 7-equi, and 9-equi plans.

Despite constraining the increase of the geometric CI to deviate by less than 10% from the value obtained using 5 equiangular-spaced beams, this constraint was only required in the non-coplanar beam optimization for the stage-III oropharyngeal case. All coplanar beam optimizations for every case demonstrated little deviation of the geometric CI. The non-coplanar beam optimization for the stage-IV oropharyngeal case demonstrated larger increases of the geometric CI, however, all the trial beam orientation sets produced deviations of less than 10% and all target dose metrics in the 5-opt-non-5432BIV plan satisfied protocol requirements. It was observed (although data not presented here) that if the geometric CI constraint was not used for the optimization of non-coplanar beams in the stage-III oropharyngeal case, the 5-opt-non-543BIV plan would demonstrate substantially improved contralateral parotid sparing at the expense of poorer target coverage (target dose metrics not satisfying protocol requirements). A possible explanation for the larger deviations of the geometric CI in the non-coplanar beam optimization for the stage-III oropharyngeal case may be attributed to a more irregularly-shaped total PTV.

The current SA optimization algorithm has several deficiencies specific to the SA optimization method. Despite the ability to simultaneously optimize multiple BIV components within a critical structure, this SA method is not a multi-objective optimization. The ability to optimize multiple BIV components within several critical structures, and not become trapped in local minima in the search space, requires a true multi-objective stochastic optimization technique which will be discussed in Chapter 6. Also, SA is a very inefficient method to explore complex search spaces since only information from a single point in the search space is evaluated for each trial beam orientation set. Theoretically, for an infinite number of sampled beam orientation sets, SA can find the global minimum. However, SA may never find the optimal solution in a practical number of sampled beam orientation sets but only a 'good' solution which may or may not be near the optimal one. For example, in the 5-opt-copl-543BIV plan for the stage-III oropharyngeal case the SA optimization did not find a better solution than the 5-opt-5BIV and 5-opt-54BIV optimizations in the given number of sampled beam orientation sets. The optimal solution for minimizing the 5 BIV, 4 BIV, and 3 BIV in this case may have required sampling of more beam orientation sets (>5000).

In addition to applying the BIV minimization methodology as a standalone BOO technique, another potential use of this method could be to provide a pre-selection (or filter) of potentially optimal beam orientations for input into a dosimetric BOO algorithm. A BIV optimization algorithm could select beam orientations with potential to improve sparing of a number of different critical structures which would serve as a pool of candidate solutions for a dose-based BOO algorithm. Current dose-based algorithms

suffer from clinically infeasible computation times (0.5 to >200 hours) since the entire space of beam orientations is searched, a computationally intense method given the complexity of accurate dose calculations. As will be discussed in Chapter 6, optimizing a geometric parameter such as BIV could significantly reduce the search space by performing an intelligent pre-selection and, therefore, make dosimetric BOO clinically feasible. The current SA algorithm is written using the Interactive Data Language (IDL; RSI, Boulder, CO). With the use of this high-level programming language for developmental purposes, typical optimization times (using 5000 iterations) for the current algorithm are on the order of seven hours but can be reduced by a factor of 100 or more by using a lower level programming language such as C.

4.5 Conclusions

In this chapter, the concept of stochastic optimization of BIV components within a critical structure was applied to 4 clinical IMRT cases to demonstrate proof-of-concept. This method can identify optimal coplanar and non-coplanar beam orientations producing substantial improvements in critical structure sparing over conventional beam orientations. In the gastric case, the coplanar optimized plan reduced the right kidney V 20 Gy by 41.1%, compared to the 5-equi plan while, in the prostate case, the coplanar optimized plan reduced the rectal V 75 Gy, V 70 Gy, V 65 Gy, and V 60 Gy by 3.9%, 6.2%, 8.1%, and 10.6% compared to the 5-equi plan. In both oropharyngeal cases, the non-coplanar optimized plan substantially reduced the V 30 Gy and mean dose to the contralateral parotid compared to the 5-equi plan: (Stage-III) 8.9% and 4.1 Gy (Stage-IV)

11.2% and 7.8 Gy. A true multi-objective BIV optimization algorithm which can simultaneously optimize multiple BIV components in several critical structures is needed and will be discussed in Chapter 6. The BIV optimization approach presented in this chapter does not require time-consuming dose calculations and has the potential to facilitate the selection of beam orientations for IMRT in a clinical setting.

4.6 Bibliography

1. Bortfeld, T. and W. Schlegel, *Optimization of beam orientations in radiation therapy: some theoretical considerations.* Phys Med Biol, 1993. **38**(2): p. 291-304.
2. Soderstrom, S. and A. Brahme, *Which is the most suitable number of photon beam portals in coplanar radiation therapy?* Int J Radiat Oncol Biol Phys, 1995. **33**(1): p. 151-9.
3. Stein, J., R. Mohan, et al., *Number and orientations of beams in intensity-modulated radiation treatments.* Med Phys, 1997. **24**(2): p. 149-60.
4. van Asselen, B., H. Dehnad, et al., *Segmental IMRT for oropharyngeal cancer in a clinical setting.* Radiother Oncol, 2003. **69**(3): p. 259-66.
5. Zhu, X.R., C.J. Schultz, et al., *Planning quality and delivery efficiency of sMLC delivered IMRT treatment of oropharyngeal cancers evaluated by RTOG H-0022 dosimetric criteria.* J Appl Clin Med Phys, 2004. **5**(4): p. 80-95.

6. Liu, H.H., M. Jauregui, et al., *Beam angle optimization and reduction for intensity-modulated radiation therapy of non-small-cell lung cancers.* Int J Radiat Oncol Biol Phys, 2006. **65**(2): p. 561-72.

7. Wang, X., X. Zhang, et al., *Development of methods for beam angle optimization for IMRT using an accelerated exhaustive search strategy.* Int J Radiat Oncol Biol Phys, 2004. **60**(4): p. 1325-37.

8. Kim, S., H.C. Akpati, et al., *An immobilization system for claustrophobic patients in head-and-neck intensity-modulated radiation therapy.* Int J Radiat Oncol Biol Phys, 2004. **59**(5): p. 1531-9.

9. Ezzell, G.A., *Genetic and geometric optimization of three-dimensional radiation therapy treatment planning.* Med Phys, 1996. **23**(3): p. 293-305.

10. Haas, O.C., K.J. Burnham, et al., *Optimization of beam orientation in radiotherapy using planar geometry.* Phys Med Biol, 1998. **43**(8): p. 2179-93.

11. Meyer, J., S.M. Hummel, et al., *Automatic selection of non-coplanar beam directions for three-dimensional conformal radiotherapy.* Br J Radiol, 2005. **78**(928): p. 316-27.

12. Rowbottom, C.G., V.S. Khoo, et al., *Simultaneous optimization of beam orientations and beam weights in conformal radiotherapy.* Med Phys, 2001. **28**(8): p. 1696-702.

13. Rowbottom, C.G., M. Oldham, et al., *Constrained customization of non-coplanar beam orientations in radiotherapy of brain tumours.* Phys Med Biol, 1999. **44**(2): p. 383-99.

14. Rowbottom, C.G., S. Webb, et al., *Improvements in prostate radiotherapy from the customization of beam directions.* Med Phys, 1998. **25**(7 Pt 1): p. 1171-9.

15. Schreibmann, E., M. Lahanas, et al., *A geometry based optimization algorithm for conformal external beam radiotherapy.* Phys Med Biol, 2003. **48**(12): p. 1825-41.

16. Wang, C., J. Dai, et al., *Optimization of beam orientations and beam weights for conformal radiotherapy using mixed integer programming.* Phys Med Biol, 2003. **48**(24): p. 4065-76.

17. Wu, X. and Y. Zhu, *A mixed-encoding genetic algorithm with beam constraint for conformal radiotherapy treatment planning.* Med Phys, 2000. **27**(11): p. 2508-16.

18. Bedford, J.L. and S. Webb, *Elimination of importance factors for clinically accurate selection of beam orientations, beam weights and wedge angles in conformal radiation therapy.* Med Phys, 2003. **30**(7): p. 1788-804.

19. Gokhale, P., E.M. Hussein, et al., *Determination of beam orientation in radiotherapy planning.* Med Phys, 1994. **21**(3): p. 393-400.

20. Rowbottom, C.G., S. Webb, et al., *Beam-orientation customization using an artificial neural network.* Phys Med Biol, 1999. **44**(9): p. 2251-62.

21. Woudstra, E. and B.J. Heijmen, *Automated beam angle and weight selection in radiotherapy treatment planning applied to pancreas tumors.* Int J Radiat Oncol Biol Phys, 2003. **56**(3): p. 878-88.

22. Beaulieu, F., L. Beaulieu, et al., *Simultaneous optimization of beam orientations, wedge filters and field weights for inverse planning with anatomy-based MLC fields.* Med Phys, 2004. **31**(6): p. 1546-57.

23. Djajaputra, D., Q. Wu, et al., *Algorithm and performance of a clinical IMRT beam-angle optimization system.* Phys Med Biol, 2003. **48**(19): p. 3191-212.

24. D'Souza, W.D., R.R. Meyer, et al., *Selection of beam orientations in intensity-modulated radiation therapy using single-beam indices and integer programming.* Phys Med Biol, 2004. **49**(15): p. 3465-81.

25. Gaede, S. and E. Wong, *An algorithm for systematic selection of beam directions for IMRT.* Med Phys, 2004. **31**(2): p. 376-88.

26. Hou, Q., J. Wang, et al., *Beam orientation optimization for IMRT by a hybrid method of the genetic algorithm and the simulated dynamics.* Med Phys, 2003. **30**(9): p. 2360-7.

27. Lee, E.K., T. Fox, et al., *Simultaneous beam geometry and intensity map optimization in intensity-modulated radiation therapy.* Int J Radiat Oncol Biol Phys, 2006. **64**(1): p. 301-20.

28. Li, Y., D. Yao, et al., *A particle swarm optimization algorithm for beam angle selection in intensity-modulated radiotherapy planning.* Phys Med Biol, 2005. **50**(15): p. 3491-514.

29. Li, Y., J. Yao, et al., *Automatic beam angle selection in IMRT planning using genetic algorithm.* Phys Med Biol, 2004. **49**(10): p. 1915-32.

30. Meedt, G., M. Alber, et al., *Non-coplanar beam direction optimization for intensity-modulated radiotherapy.* Phys Med Biol, 2003. **48**(18): p. 2999-3019.

31. Pugachev, A., J.G. Li, et al., *Role of beam orientation optimization in intensity-modulated radiation therapy.* Int J Radiat Oncol Biol Phys, 2001. **50**(2): p. 551-60.

32. Pugachev, A. and L. Xing, *Pseudo beam's-eye-view as applied to beam orientation selection in intensity-modulated radiation therapy.* Int J Radiat Oncol Biol Phys, 2001. **51**(5): p. 1361-70.

33. Pugachev, A. and L. Xing, *Computer-assisted selection of coplanar beam orientations in intensity-modulated radiation therapy.* Phys Med Biol, 2001. **46**(9): p. 2467-76.

34. Pugachev, A. and L. Xing, *Incorporating prior knowledge into beam orientation optimization in IMRT.* Int J Radiat Oncol Biol Phys, 2002. **54**(5): p. 1565-74.

35. Pugachev, A.B., A.L. Boyer, et al., *Beam orientation optimization in intensity-modulated radiation treatment planning.* Med Phys, 2000. **27**(6): p. 1238-45.

36. Rowbottom, C.G., C.M. Nutting, et al., *Beam-orientation optimization of intensity-modulated radiotherapy: clinical application to parotid gland tumours.* Radiother Oncol, 2001. **59**(2): p. 169-77.

37. Schreibmann, E., M. Lahanas, et al., *Multiobjective evolutionary optimization of the number of beams, their orientations and weights for intensity-modulated radiation therapy.* Phys Med Biol, 2004. **49**(5): p. 747-70.

38. Schreibmann, E. and L. Xing, *Feasibility study of beam orientation class-solutions for prostate IMRT.* Med Phys, 2004. **31**(10): p. 2863-70.

39. Schreibmann, E. and L. Xing, *Dose-volume based ranking of incident beam direction and its utility in facilitating IMRT beam placement.* Int J Radiat Oncol Biol Phys, 2005. **63**(2): p. 584-93.

40. Wang, X., X. Zhang, et al., *Effectiveness of noncoplanar IMRT planning using a parallelized multiresolution beam angle optimization method for paranasal sinus carcinoma.* Int J Radiat Oncol Biol Phys, 2005. **63**(2): p. 594-601.

41. Yang, R., J. Dai, et al., *Beam orientation optimization for intensity-modulated radiation therapy using mixed integer programming.* Phys Med Biol, 2006. **51**(15): p. 3653-66.

42. Das, S., T. Cullip, et al., *Beam orientation selection for intensity-modulated radiation therapy based on target equivalent uniform dose maximization.* Int J Radiat Oncol Biol Phys, 2003. **55**(1): p. 215-24.

43. Woudstra, E., B.J. Heijmen, et al., *Automated selection of beam orientations and segmented intensity-modulated radiotherapy (IMRT) for treatment of oesophagus tumors.* Radiother Oncol, 2005. **77**(3): p. 254-61.

44. Deasy, J.O., *Multiple local minima in radiotherapy optimization problems with dose-volume constraints.* Med Phys, 1997. **24**(7): p. 1157-61.

45. Kirkpatrick, S., C.D. Gelatt, Jr., et al., *Optimization by Simulated Annealing.* Science, 1983. **220**(4598): p. 671-680.

46. Metropolis, N., A.W. Rosenbluth, et al., *Equation of State Calculations by Fast Computing Machines.* The Journal of Chemical Physics, 1953. **21**(6): p. 1087.

47. Knoos, T., I. Kristensen, et al., *Volumetric and dosimetric evaluation of radiation treatment plans: radiation conformity index.* Int J Radiat Oncol Biol Phys, 1998. **42**(5): p. 1169-76.

48. Zelefsky, M.J., Z. Fuks, et al., *High-dose intensity modulated radiation therapy for prostate cancer: early toxicity and biochemical outcome in 772 patients.* Int J Radiat Oncol Biol Phys, 2002. **53**(5): p. 1111-6.

49. Shepard, D.M., M.A. Earl, et al., *Direct aperture optimization: a turnkey solution for step-and-shoot IMRT.* Med Phys, 2002. **29**(6): p. 1007-18.

50. Siebers, J.V., M. Lauterbach, et al., *Incorporating multi-leaf collimator leaf sequencing into iterative IMRT optimization.* Med Phys, 2002. **29**(6): p. 952-9.

51. Chao, K.S., J.O. Deasy, et al., *A prospective study of salivary function sparing in patients with head-and-neck cancers receiving intensity-modulated or three-dimensional radiation therapy: initial results.* Int J Radiat Oncol Biol Phys, 2001. **49**(4): p. 907-16.

52. Eisbruch, A., H.M. Kim, et al., *Xerostomia and its predictors following parotid-sparing irradiation of head-and-neck cancer.* Int J Radiat Oncol Biol Phys, 2001. **50**(3): p. 695-704.

CHAPTER FIVE: IMPROVING INTENSITY MODULATED RADIATION THERAPY USING THE ANATOMIC BEAM ORIENTATION OPTIMIZATION ALGORITHM

This chapter is adapted from a manuscript entitled "Improving Intensity Modulated Radiation Therapy Using the Anatomic Beam Orientation Optimization Algorithm" by Peter Potrebko, Boyd McCurdy, James Butler, and Adel El-Gubtan accepted for publication in *Medical Physics* in 2008.

5.1 Introduction

The selection of beam orientations for intensity-modulated radiation therapy (IMRT) requires the experience and intuition of the dosimetrist or a trial-and-error approach. Alternatively, several studies [1-3] have provided a strategy to avoid the suboptimal placement of beams by employing a relatively large number of beams, such as nine coplanar equiangular-spaced beams, so that the IMRT plan may not be sensitive to the choice of individual beam angles. However, the spread of low doses to larger volumes of normal tissues [4, 5], increased treatment delivery time, quality assurance efforts, and the probability of patient movement during delivery [6] may negate the benefits of using a larger number of beams. Therefore, the selection of *the fewest number of optimal beams possible* is still the subject of active research. Many beam orientation optimization (BOO) methods have been proposed in both three-dimensional conformal radiation therapy (3D-CRT) [1, 7-19] and IMRT [1-5, 20-41]. An exhaustive search [4, 5,

19, 23, 28, 38, 41], simulated annealing optimization [10, 11, 16, 20, 21, 29, 32-34], genetic algorithms [7, 15, 24, 27, 35, 36], and integer programming [14, 22, 25, 39] have been studied. However, given the computationally intensive nature of accurate dose calculations in IMRT, current dose-based BOO approaches have clinically infeasible computation times (0.5 to >200 hours).

While geometric methods have the potential to greatly reduce optimization time, only a few studies limited to 3D-CRT, have been published [7-9, 13]. The idea of using geometrical considerations to optimize an objective function (OF) was first proposed by Haas *et al.* [8]. The author's used an OF that aimed at geometrically conforming the 2D beam's intersection with the planning-target-volume (PTV) surface while minimizing the intersection area between beams and Organs-At-Risk (OARs). A multi-objective genetic algorithm was employed to minimize the geometrical OF. However, the method was restricted to using only the most representative 2D computed tomographic (CT) slice, and many simplifications were used, such as assuming that the fields have no divergence. Schreibmann *et al.* [13] improved on previous geometric methods by using a true, 3D-volume computation which took into account beam divergence, concave shapes, as well as treatment settings such as individual beam shaping by blocks or multi-leaf collimators. The method used geometric derived quantities which consider the intersection volume between OARs and the beam shape. The geometrical OF was optimized using an adaptive simulated annealing algorithm that used a re-annealing and adapted the cooling for each individual decision variable by analyzing its sensitivity to temperature changes.

However, the 3D-CRT solutions obtained by their geometrical model did not consider dose 'hot spots' caused by beam overlaps.

In this chapter, an anatomy-based BOO algorithm for IMRT is proposed. The algorithm is applied to select 5 optimal beam orientations which produce improved OAR sparing compared to standard equiangular-spaced beam arrangements. Three different disease sites, gastric, prostate, and oropharynx (two examples) have been investigated. This study also emphasizes the usefulness of non-coplanar beam orientations to substantially improve OAR sparing. It will be demonstrated that anatomy-based BOO is a clinically practical tool to facilitate the selection of beam orientations in IMRT.

5.2 Methods and Materials

The Anatomic-BOO (A-BOO) algorithm for IMRT is presented here. The premise of the algorithm is two-fold: (1) Locate beams which bisect the target and adjacent OARs. These beam orientations should have a greater opportunity to produce sharp dose gradients with more rapid dose fall-off away from the target and improved sparing of adjacent critical structures especially those in close proximity. (2) Preferentially locate beams parallel to 3D flat surface features of the PTV. These beam orientations should facilitate conformity of target coverage. The components of the algorithm are discussed below.

5.2.1 Interface to Treatment Planning System

The algorithm interfaces to the Pinnacle^3 research version 8.1r (Philips Radiation Oncology Systems, Milpitas, CA, USA) treatment planning system to obtain region-of-interest (ROI) information from patient treatment plans. Based on contours in the plan, triangular polygonal surface mesh's of all ROIs are generated in Pinnacle^3 and the Cartesian coordinates of all polygon vertices and vertex indices are extracted by the algorithm. The physical size of the ROI determines the number of mesh polygons ranging from about 1,000-10,000.

5.2.2 ROI Surface Mesh Analysis

A sphere of all possible beam source orientations (gantry°, couch°) pairs is pre-computed in 1° increments. For each triangular polygon (i) in the PTV, the area of the polygon (Δ_i), the Cartesian coordinates of the surface normal unit vector ($\hat{N}_i$), and the angle (θ_i) between the surface normal unit vector and all beam source orientation unit vectors ($\hat{S}$) are computed (Figure 5.1):

$$\Delta_i = \frac{1}{2}\sqrt{\begin{vmatrix} y_1 & z_1 & 1 \\ y_2 & z_2 & 1 \\ y_3 & z_3 & 1 \end{vmatrix}^2 + \begin{vmatrix} z_1 & x_1 & 1 \\ z_2 & x_2 & 1 \\ z_3 & x_3 & 1 \end{vmatrix}^2 + \begin{vmatrix} x_1 & y_1 & 1 \\ x_2 & y_2 & 1 \\ x_3 & y_3 & 1 \end{vmatrix}^2} \tag{5.1}$$

where (x_1, y_1, z_1), (x_2, y_2, z_2), (x_3, y_3, z_3) are the coordinates of the vertices

$$\hat{N}_i = \frac{\overrightarrow{L_1} \times \overrightarrow{L_2}}{\left|\overrightarrow{L_1} \times \overrightarrow{L_2}\right|} \tag{5.2}$$

where $\overrightarrow{L_1} = [x_2 - x_1, y_2 - y_1, z_2 - z_1]$, $\overrightarrow{L_2} = [x_3 - x_1, y_3 - y_1, z_3 - z_1]$

$$\theta_i = \cos^{-1}\left(\hat{S} \bullet \hat{N}_i\right) \tag{5.3}$$

The algorithm preferentially weights PTV polygons which are in close proximity to OARs. To achieve this, the minimum center-to-center distance (D_i) between each PTV polygon and all OAR polygons is computed (Figure 5.1). An inverse-distance weighting function (W_i) is used (although any decreasing function could be employed) to set a preferential importance to beam orientations in which the beams tangentially bisect the target and adjacent OARs and therefore produce a sharp dose gradient between them. Beam source orientation vectors that are perpendicular (or near-perpendicular) to the PTV polygonal surface normal vectors are also identified. In this way, beam orientations parallel to flat surface features of the PTV are selected. A phasespace image is generated as a function of gantry and couch angle where the PTV polygonal areas corresponding to source orientations which (1) tangentially bisect the target and adjacent OARs and/or (2) are parallel to flat surface features of the PTV are cumulated as a score (grayscale) value:

$$Score(gantry°, couch°) = \sum_{i=1}^{N} W_i * \Delta_i \tag{5.4}$$

where N = number of PTV polygons

$$W_i = \begin{cases} 1 & , \quad D_i < 1 \quad (cm) \\ 1/D_i & , \quad otherwise \end{cases} \tag{5.5}$$

Therefore, if D_i is less than 1 cm, a maximum weight of unity is assigned (avoiding an undefined W_i if the target and OAR are in direct contact) to beam orientations which tangentially bisect the target and OAR. The larger the score value, the more 'optimal' the

beam orientation for OAR sparing and/or conformal PTV coverage. The algorithm outputs the score value and corresponding (gantry°, couch°) pair in descending order for the user.

Figure 5.1: A sphere of all possible beam source orientations (gantry°, couch°) pairs is pre-computed by the algorithm (shown as points). For each polygon, i, in the PTV, the area of the polygon, the Cartesian coordinates of the surface normal unit vector ($\hat{N}_i$), and the angle (θ_i) between the surface normal unit vector and all beam source orientation unit vectors ($\hat{S}$) are computed. The minimum center-to-center distance (D_i) between each PTV polygon and all OAR polygons is also computed (only one pair of PTV and OAR polygons are illustrated).

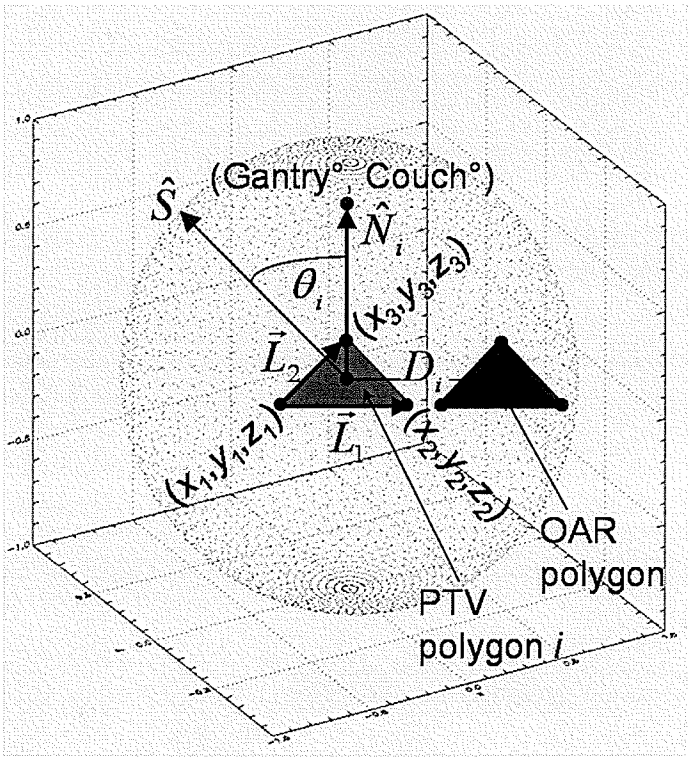

5.2.3 Elimination of Infeasible Beam Orientations

Divergent ray tracing is performed through the 3D patient structure matrix, and beam orientations entering through inferior or superior regions where computed tomographic (CT) data are not available are eliminated. Mechanically infeasible beam orientations leading to gantry/couch collisions are also eliminated. In addition, the algorithm excludes parallel-opposed beam orientations for IMRT and applies a minimum beam separation of 20°.

5.2.4 Implementation on Clinical Examples

The A-BOO algorithm was implemented on 3 treatment sites: (1) a gastric cancer patient with prescription dose of 50.4 Gy in 28 fractions and OARs included liver, spinal cord, and left and right kidneys, (2) a localized prostate cancer patient following the RTOG P-0126 protocol with prescription dose of 79.2 Gy in 44 fractions where the PTV included the proximal bilateral seminal vesicles and OARs included left and right femoral heads, bladder, and rectum. (3) two oropharyngeal cancer patients following the RTOG H-0022 protocol with prescription dose of 66 Gy in 30 fractions, where PTV66 included the gross tumour and lymph node metastasis, and PTV54 included the bilateral neck lymph nodes (receiving 54 Gy), and OARs included glottic larynx, brainstem, spinal cord, mandible, and left and right parotid glands. The first oropharyngeal cancer case is stage-III squamous cell carcinoma of the left tonsil. The second oropharyngeal cancer case is more complicated, presenting as a bulky stage-IV (upstaged by imaging)

squamous cell carcinoma of the left tonsil where the bulky primary is extending to the nasopharynx. These are the same four clinical examples studied in Chapter 4.

For each case, an IMRT treatment plan with 5 optimized beam orientations (5-opt) selected by the A-BOO algorithm was compared to IMRT plans with 5, 7, and 9 equiangular-spaced beam orientations (5-equi, 7-equi, 9-equi). For the prostate case, the treatment plan with 5 optimized beam orientations was also compared to plans with 5 optimal equiangular-spaced beam orientations (from Chapter 2) and with the Zelefsky 5 beam orientations [42]. All IMRT plans were generated in Pinnacle^3 using direct machine parameter optimization (DMPO) with 6 MV photon beams, static multileaf collimator (MLC) delivery, and with a supine treatment position. The DMPO method in Pinnacle^3, based upon direct aperture optimization [43], includes the MLC positions and segment weights as parameters of the optimization [44]. A maximum of 100 total segments were used for each plan, and the same set of inverse planning objectives was used between the 5-opt, 5-equi, 7-equi, and 9-equi plans for a particular treatment site. The clinical objectives for each treatment site are summarized in Table 5.1. Dose-volume histograms (DVHs) for the target(s) and the OARs as well as isodose distributions were used to evaluate the quality of the plans. In this chapter, the A-BOO algorithm was used as a treatment planning tool to automatically evaluate the complete space of beam orientations and systematically provide optimal beams. The algorithm provided the treatment planner with a list of ranked scores and beam orientations to facilitate sparing of a user-selected OAR. A similar list was also produced based on target conformity. Five top ranked beam orientations were chosen in this manner and used to generate the 5-opt plans. In the

clinical cases presented, A-BOO was used to provide a list of ranked scores for only the most important OAR in a particular treatment site (right kidney, rectum, parotid glands). In principle, the algorithm could be used to improve sparing of several OARs in a treatment plan by providing the treatment planner with top ranked beam orientations for each OAR. The algorithm can be applied for both IMRT and 3D-CRT, where in the latter parallel-opposed beam orientations are not restricted.

Table 5.1: Clinical objectives for each treatment site.

Tx Site	Structure	Objective
Gastric	PTV	V50.4 $\geq$ 95%
		V53.9 = 0%
	Rt Kidney	V20 < 60%
	Lt Kidney	V20 < 60%
	Liver	V30 < 60%
	Spinal Cord	D_{max} < 45 Gy
Prostate	PTV	V79.2 $\geq$ 98%
		V84.7 < 2%
	Rectum	V75 < 15%
		V70 < 25%
		V65 < 35%
		V60 < 50%
	Bladder	V80 < 15%
		V75 < 25%
		V70 < 35%
		V65 < 50%
	Lt Femur	D_{max} < 54 Gy
	Rt Femur	D_{max} < 54 Gy
Oropharynx	PTV66	V66 $\geq$ 95%
		V72.6 < 20%
	PTV54	V54 $\geq$ 95%
		V59.4 < 20%
	Glottic Larynx	V50 < 66%
	Brainstem	D_{max} < 54 Gy
	Spinal Cord	D_{max} < 45 Gy
	Mandible	D_{max} < 70 Gy
	Unspecified Tissue	V72.6 < 1%
	Lt Parotid	V30 < 50%
	Rt Parotid	V30 < 50%

5.2.5 Uncertainty Analysis

Uncertainties of the A-BOO algorithm were investigated using a geometric phantom. For any given axial CT slice, the phantom contained a right-triangle PTV (hypotenuse coincident with isocenter) and a circular OAR which was 0.7 cm away from the hypotenuse of the PTV at closest approach. Beams with parallel incidence to each face of the PTV were known to correspond to beam orientations (gantry°, couch°) of (0°, 0°), (90°, 0°) and (165°, 0°), or their parallel-opposed counterparts. The optimal beam orientations as identified by the algorithm were compared to the known PTV side orientations.

The A-BOO algorithm assumes that all PTV polygons are located at the isocenter. Therefore, the divergence of a beam to PTV polygons away from the isocenter is not explicitly modeled. The maximum effect of neglecting beam divergence was estimated by locating the right-triangle PTV approximately 17 cm (distance to hypotenuse) away from isocenter, a scenario that could occur in a patient if the PTV approaches the skin surface, and repeating the above analysis.

5.3 Results

5.3.1 Gastric Cancer

The algorithm provided the following 5 optimal beam orientations (gantry°, couch°) to facilitate conformal target coverage and spare the right kidney (the closest

OAR), which is in close proximity (approximately 0.7 cm at closest approach) to the PTV: (0°, 0°), (45°, 0°), (89°, 0°), (88°, 321°), (313°, 355°). All beam orientations except (45°, 0°) had the highest scores in the target conformity ranked score list as well as the right kidney sparing list. The beam orientation (45°, 0°) had the next highest score in the target conformity list. The isodose distributions for the plans with 5 optimized beams and 5 equiangular-spaced beams are shown in Figure 5.2. The non-coplanar 5-opt plan reduced the right kidney V 20 Gy by 32.2 %, 23.2 %, and 20.6 % compared to 5, 7, and 9 equiangular-spaced beam plans, respectively. The DVHs for the right kidney and PTV using 5 optimized beams compared to 5, 7, 9 equiangular-spaced beams are shown in Figure 5.3. The PTV metrics demonstrated little variation between all plans (V 50.4 Gy of 99.6 – 100.0 %, mean dose of 51.4 – 51.5 Gy ± 0.2 – 0.3 Gy, and V 53.9 Gy of 0 %). The liver, left kidney, and spinal cord metrics also demonstrated little variation between all plans.

Figure 5.2: The IMRT dose distributions for the gastric case using (a) 5 equiangular-spaced beams (b) 5 optimized non-coplanar beams which produce an improved sharpened dose gradient between the right kidney and the PTV due to the algorithms preference for placing beam edges between targets and OARs. The 47.9 Gy (95%), 45 Gy, 30 Gy, and 20 Gy isodose lines are displayed. OARs including liver, spinal cord, and left and right kidneys are shown.

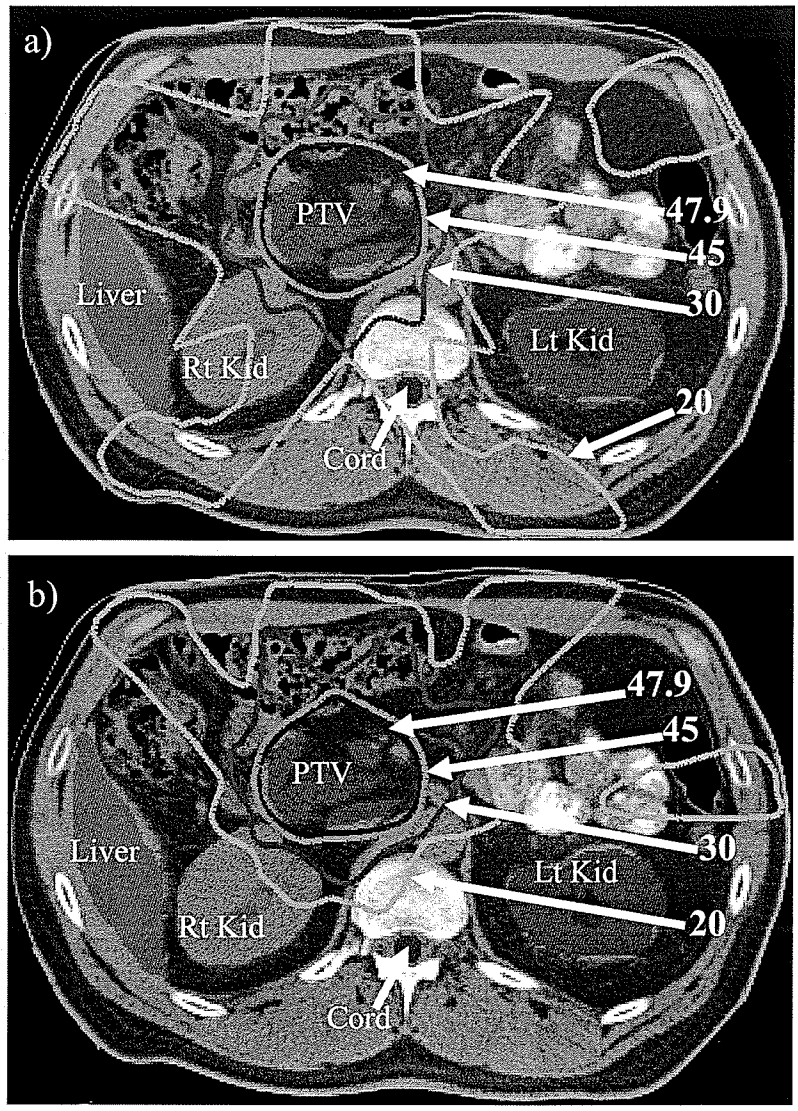

Figure 5.3: The gastric case dose-volume histograms of the right kidney and PTV using 5 optimized non-coplanar beams compared to 5, 7, and 9 equiangular-spaced beams.

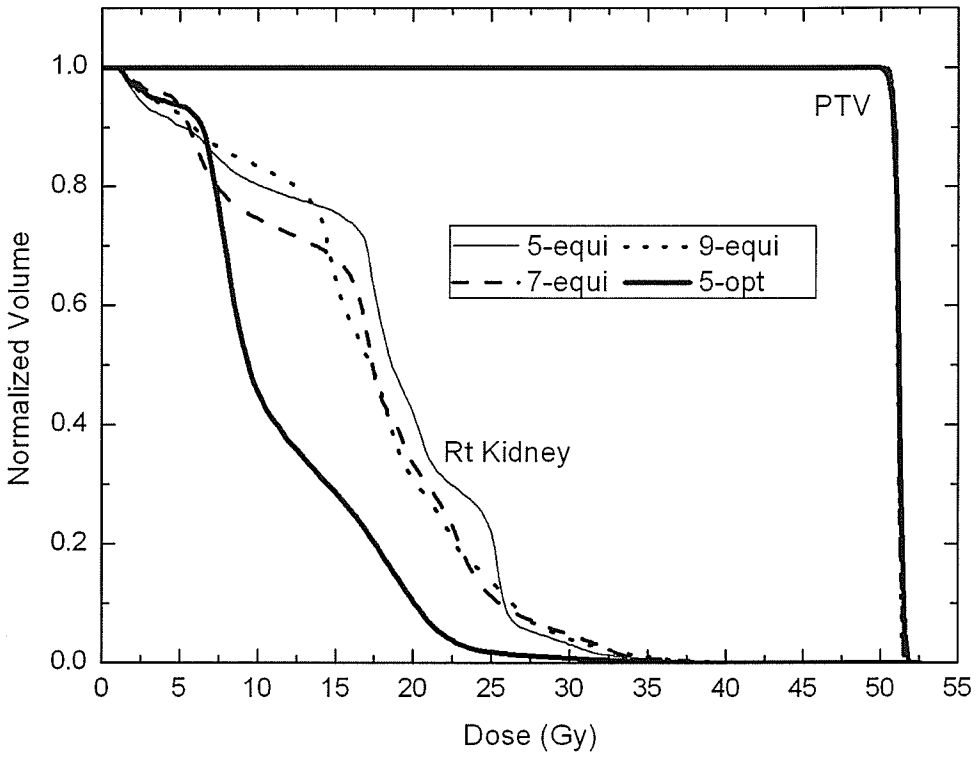

5.3.2 Prostate Cancer

IMRT:

The algorithm provided the following 5 optimal beam orientations (gantry°, couch°) to facilitate target conformity and spare the rectum: (0°, 0°), (24°, 0°), (91°, 0°), (111°, 0°), (246°, 0°). The (91°, 0°) beam orientation had the highest score in the rectal sparing list while all other beam orientations had the highest scores in the target conformity list. The rectal V 75 Gy, V 70 Gy, V 65 Gy, and V 60 Gy were reduced by 2.4 %, 5.3%, 7.0 %, and 9.5 %, respectively in the 5-opt plan compared to the 5-equi plan. The DVHs for the rectum and PTV using 5 optimized beams compared to 5, 7, 9

equiangular-spaced beams starting at 0°, 5 optimal equiangular-spaced beams starting at 20°, and the Zelefsky 5 beam orientations are shown in Figure 5.4. The PTV metrics demonstrated little variation between all plans (V 79.2 Gy of 99.0 - 99.8 %, mean dose of 80.5 - 81.0 Gy ± 0.3 - 0.4 Gy, and V 84.7 Gy of 0 %). The bladder and femoral head metrics also demonstrated little variation between all plans.

Figure 5.4: The prostate case dose-volume histograms of the rectum and PTV using 5 optimized coplanar beams compared to 5, 7, 9 equiangular-spaced beams starting at 0°, 5 optimal equiangular-spaced beams starting at 20°, and the Zelefsky 5 beam orientations.

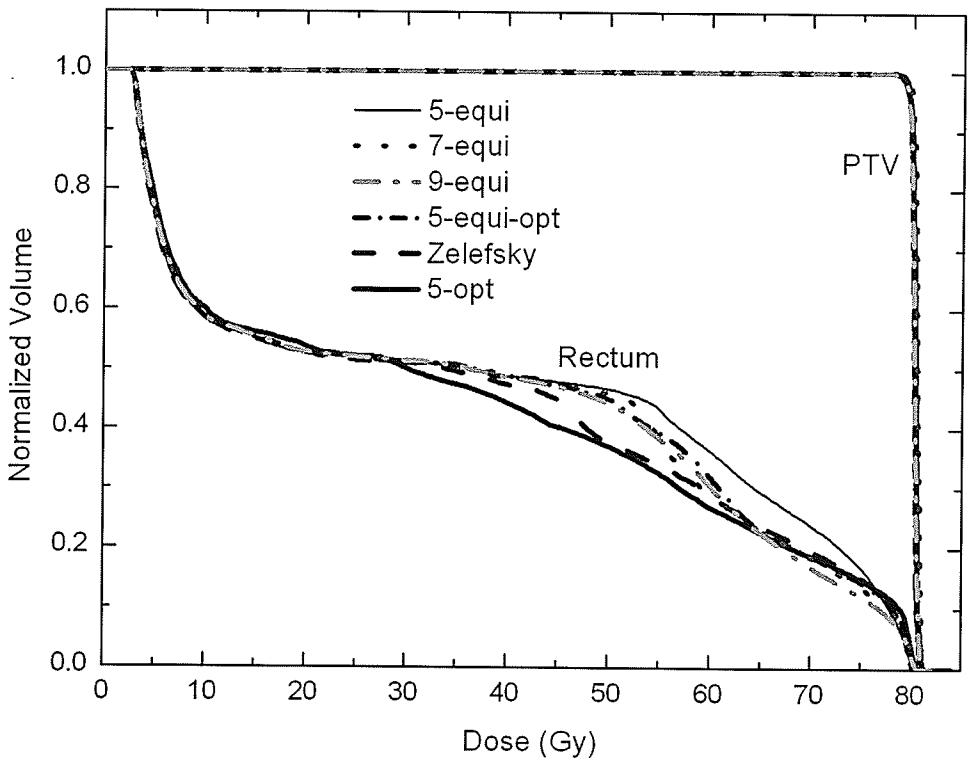

3D-CRT:

Removing the parallel-opposed restriction, the algorithm provided the following 4 optimal 3D-CRT beam orientations (gantry°, couch°) to facilitate target conformity and rectal sparing: (0°, 0°), (91°, 0°), (179°, 0°), (271°, 0°). The lateral beams (91°, 0°), (271°, 0°) had the highest scores in the rectal sparing list while the other beam orientations had the highest scores in the target conformity list. These 4 optimal beam orientations are commonly used in prostate 3D-CRT and are known as the '4-field box' technique.

5.3.3 Oropharyngeal Cancer

Stage-III:

The algorithm provided the following 5 optimal coplanar (5-opt-copl) beam orientations (gantry°, couch°) to facilitate target (PTV66+PTV54) conformity and spare the right (contralateral) parotid gland: (0°, 0°), (40°, 0°), (118°, 0°), (143°, 6°), (211°, 0°). The beam orientation (211°, 0°) had the highest coplanar score in the contralateral parotid sparing list and all other beam orientations had the highest scores in the target conformity list. The algorithm also identified the following 5 optimal non-coplanar (5-opt-non-copl) beam orientations (gantry°, couch°) to facilitate target conformity and spare the contralateral parotid gland: (0°, 0°), (40°, 0°), (143°, 6°), (211°, 0°), (213°, 333°). The beam orientation (213°, 333°) had the highest non-coplanar score in the contralateral parotid sparing list. The DVHs for the contralateral parotid gland, PTV54, and PTV66 using 5 optimized coplanar beams and 5 optimized non-coplanar beams, compared to 5,

7, and 9 equiangular-spaced beams are shown in Figure 5.5. Tables 5.2a and 5.2b summarize the clinical metrics of the targets and OARs for each treatment plan.

Figure 5.5: The stage-III oropharyngeal dose-volume histograms of the contralateral parotid gland, PTV54, and PTV66 using 5 optimized coplanar beams, 5 optimized non-coplanar beams compared to 5, 7, and 9 equiangular-spaced beams.

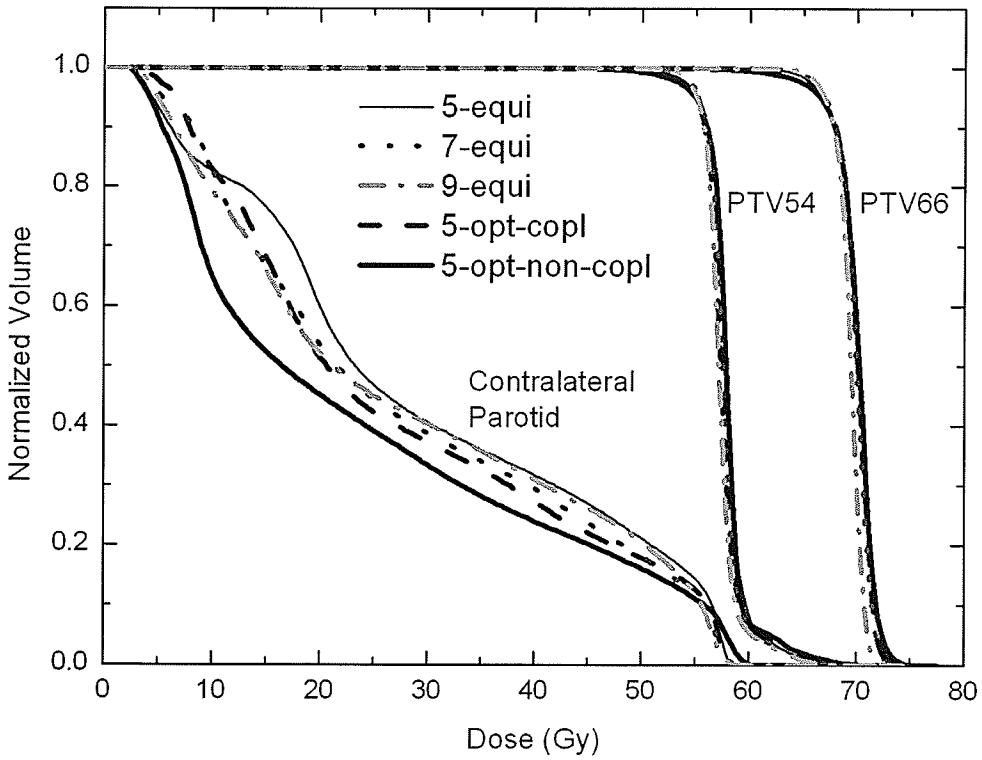

Table 5.2a: Clinical target metrics for each plan in the stage-III oropharyngeal case.

	PTV66 V66 (%)	PTV66 V72.6 (%)	PTV66 Mean (Gy)	PTV54 V54 (%)	PTV54 V59.4 (%)	PTV54 Mean (Gy)
5-equi	97.6	5.3	70.4 ± 1.8	98.1	17.0	58.3 ± 2.1
7-equi	98.2	2.5	70.2 ± 1.5	98.9	10.5	58.0 ± 1.8
9-equi	98.5	0.2	69.7 ± 1.3	98.8	8.3	57.7 ± 1.8
5-opt-copl	97.8	2.7	70.3 ± 1.6	97.6	11.2	57.9 ± 2.1
5-opt-non-copl	96.8	6.4	70.3 ± 2.0	97.3	14.2	58.3 ± 2.3

Table 5.2b: Clinical organ-at-risk metrics for each plan in the stage-III oropharyngeal case. Ipar (Ipsilateral parotid), Cpar (Contralateral parotid), Cord (Spinal cord+5mm).

	Larynx V50 (%)	Brainstem Max (Gy)	Cord Max (Gy)	Mandible Max (Gy)	Ipar V30 (%)	Ipar Mean (Gy)	Cpar V30 (%)	Cpar Mean (Gy)
5-equi	26.5	30.2	38.1	70.3	46.9	31.7	41.0	29.4
7-equi	30.0	20.7	36.2	70.4	46.2	31.6	39.1	27.8
9-equi	44.5	25.6	34.6	70.1	43.8	31.1	40.7	28.0
5-opt-copl	19.6	32.5	40.8	70.5	45.1	31.2	37.7	27.5
5-opt-non-copl	7.9	35.3	40.3	70.7	48.5	31.8	33.9	24.3

Stage-IV bulky primary extending to nasopharynx:

The algorithm provided the following 5 optimal coplanar (5-opt-copl) beam orientations (gantry°, couch°) to facilitate target (PTV66+PTV54) conformity and spare the left (ipsilateral) and right (contralateral) parotid glands: (0°, 0°), (45°, 0°), (121°, 0°), (151°, 0°), (215°, 0°). The beam orientations (0°, 0°) and (151°, 0°) had the highest coplanar scores in the target conformity list and ipsilateral parotid sparing list. The beam orientation (215°, 0°) had the highest coplanar score in the contralateral parotid sparing list. The beam orientations (45°, 0°) and (121°, 0°) had the highest scores in the target conformity list. The algorithm also identified the following 5 optimal non-coplanar (5-opt-non-copl) beam orientations (gantry°, couch°) to facilitate target conformity and spare the ipsilateral and contralateral parotid glands: (0°, 0°), (137°, 0°), (131°, 311°), (215°, 0°), (228°, 40°). The beam orientations (0°, 0°), (137°, 0°), (131°, 311°) had the highest non-coplanar scores in the target conformity list and the ipsilateral parotid sparing list. The beam orientations (215°, 0°), (228°, 40°) had the highest non-coplanar scores in the contralateral parotid sparing list. The isodose distributions for the plans with 5 optimized non-coplanar beams and 5 equiangular-spaced beams are shown in Figure 5.6. The DVHs for the contralateral parotid gland, PTV54, and PTV66 using 5 optimized coplanar beams, 5 optimized non-coplanar beams, compared to 5, 7, and 9 equiangular-spaced beams are shown in Figure 5.7. Tables 5.3a and 5.3b summarize the clinical metrics of the targets and OARs for each treatment plan.

Figure 5.6: The IMRT dose distributions for the stage-IV oropharyngeal case using (a) 5 equiangular-spaced beams (b) 5 optimized non-coplanar beams which produce an improved sharpened dose gradient between the parotids and the PTV due to the algorithms preference for placing beam edges between targets and OARs. The 62.7 Gy (95% of PTV66), 51.3 Gy (95% of PTV54), 45 Gy, and 30 Gy isodose lines are displayed. OARs including mandible, spinal cord +5mm, and left (ipsilateral) and right (contralateral) parotid glands are shown.

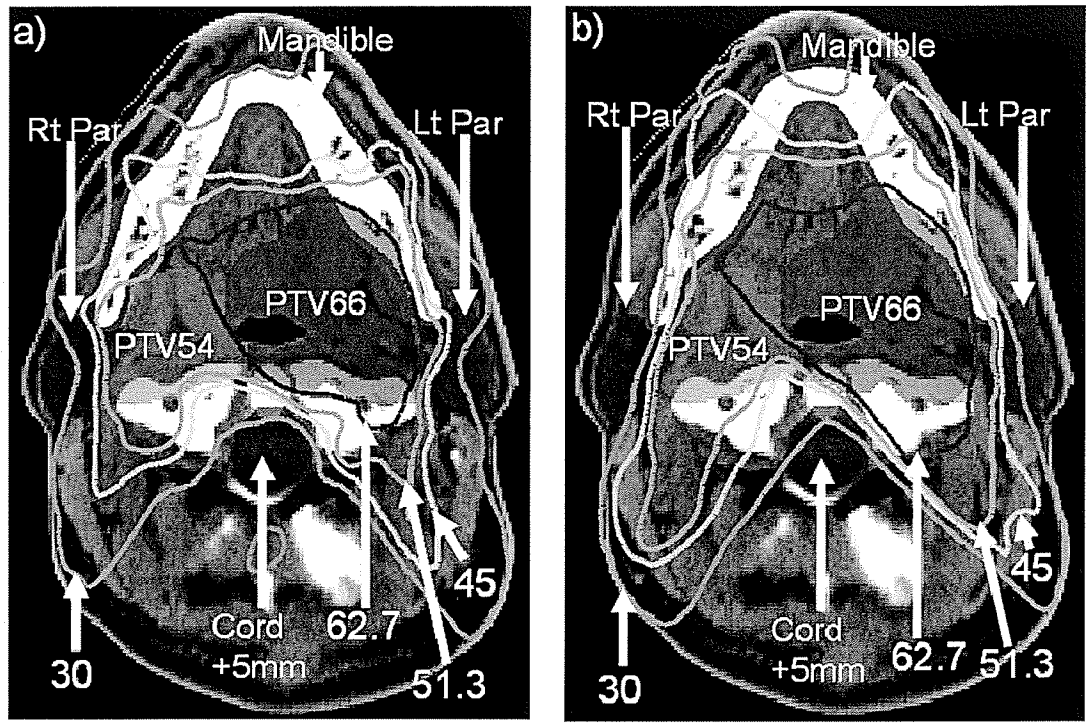

Figure 5.7: The stage-IV oropharyngeal dose-volume histograms of the contralateral parotid gland, PTV54, and PTV66 using 5 optimized coplanar beams, 5 optimized non-coplanar beams compared to 5, 7, and 9 equiangular-spaced beams.

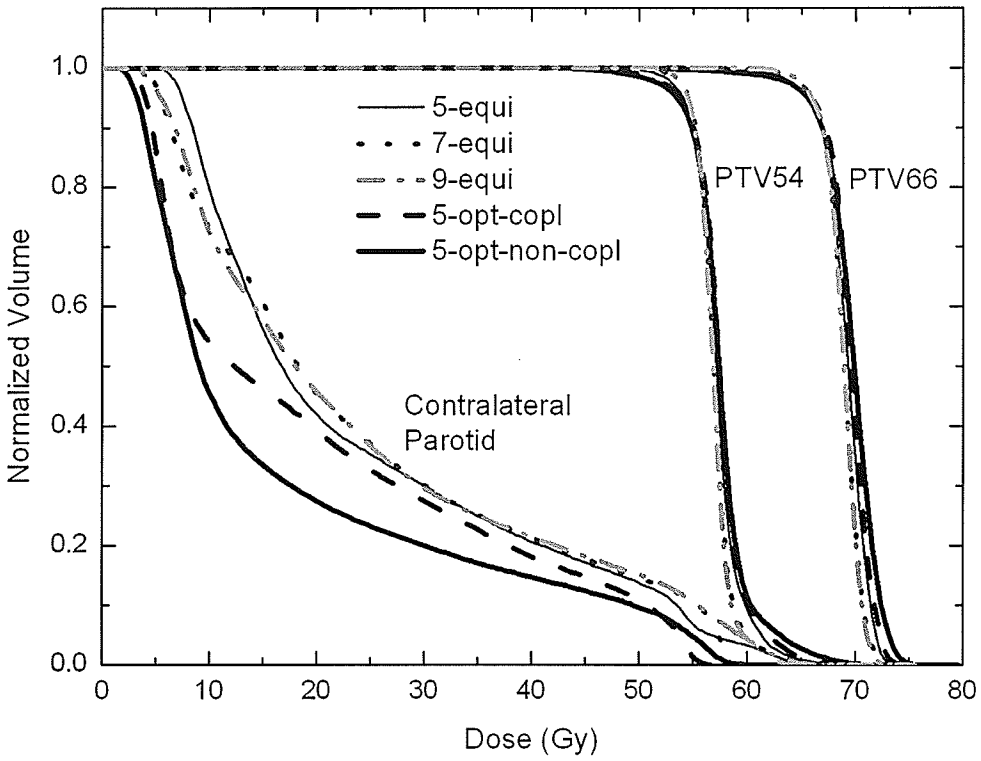

Table 5.3a: Clinical target metrics for each plan in the stage-IV oropharyngeal case.

	PTV66 V66 (%)	PTV66 V72.6 (%)	PTV66 Mean (Gy)	PTV54 V54 (%)	PTV54 V59.4 (%)	PTV54 Mean (Gy)
5-equi	95.3	5.3	69.8 ± 2.1	96.7	16.9	57.9 ± 2.3
7-equi	95.8	1.0	69.2 ± 1.7	98.0	8.4	57.4 ± 1.8
9-equi	95.9	0.4	69.2 ± 1.6	98.0	7.0	57.3 ± 1.7
5-opt-copl	95.6	5.9	69.8 ± 2.1	95.4	17.0	57.9 ± 2.5
5-opt-non-copl	95.4	14.7	70.2 ± 2.6	95.1	19.2	57.9 ± 3.0

Table 5.3b: Clinical organ-at-risk metrics for each plan in the stage-IV oropharyngeal case. Ipar (Ipsilateral parotid), Cpar (Contralateral parotid), Cord (Spinal cord+5mm).

	Larynx V50 (%)	Brainstem Max (Gy)	Cord Max (Gy)	Mandible Max (Gy)	Ipar V30 (%)	Ipar Mean (Gy)	Cpar V30 (%)	Cpar Mean (Gy)
5-equi	0.6	50.4	40.1	70.5	44.1	32.4	30.5	24.4
7-equi	8.9	49.6	37.6	69.6	44.3	32.2	30.5	24.5
9-equi	7.1	47.7	37.4	69.7	41.5	31.7	30.1	24.6
5-opt-copl	7.6	50.6	40.0	71.8	43.6	32.2	27.8	20.6
5-opt-non-copl	7.1	53.9	42.8	71.1	41.2	31.2	20.3	17.4

5.3.4 Uncertainty Results

The algorithm produced a beam orientation of (162°, 1°) for optimal geometric target conformity and optimal geometric sparing of the OAR (tangential orientation bisecting the target and OAR) compared to the expected beam orientation of (165°, 0°). Two additional beam orientations of (0°, 2°) and (89°, 5°) were selected by the algorithm for optimal target conformity compared to the expected beam orientations of (0°, 0°) and (90°, 0°). This demonstrated that uncertainties of up to 5° in the gantry or couch angle may be associated with the optimal beam orientations. This uncertainty arises from image processing performed to detect local maxima (optimal beam orientations) in the phasespace image containing the PTV polygonal areas that have been cumulated as a grayscale value.

In the beam divergence analysis, the algorithm produced similar beam orientations of (0°, 2°), (89°, 5°), and (162°, 2°) for optimal target conformity, compared to the expected beam orientations of (0°, 0°), (90°, 0°) and (165°, 0°), which indicated that any error associated with neglecting beam divergence was very small. In fact, since the algorithm identifies beam source orientation vectors that are near-perpendicular (within a window of ± 5°) to the PTV polygonal surface normal vectors, any beam angle identification uncertainty is most likely within this ± 5° window.

5.4 Discussion

The premise of locating tangential beams which bisect the target volume and adjacent critical structures (thereby allowing for a steep dose gradient between them) and aligning beams parallel to 3D flat surface features of the target volume (to facilitate target conformity) intuitively makes sense. This method selects beam orientations which have the potential to assist the IMRT optimization in finding more optimal solutions, especially if additional critical structure sparing is necessary. In this chapter, the A-BOO algorithm was implemented on four successively more complicated clinical cases (gastric, prostate, oropharyngeal stage-III and -IV) to clearly demonstrate its usefulness.

In the gastric case, with the use of 5 optimized non-coplanar beam orientations, substantial sparing of the right kidney (compared to the plan with 5 equiangular-spaced beams) was demonstrated. In fact, the 5-opt plan produced far superior right kidney sparing than plans using standard clinical beam arrangements (5, 7, and 9 equiangular-

spaced beams) without compromising any plan metrics for target coverage and sparing of other critical structures or changing any dose objectives in the plans.

In the prostate case, the use of 5 optimized beam orientations produced considerable rectal sparing in the moderate and high dose regions with no compromise in target coverage compared to the plan with 5 equiangular-spaced beams. The anatomy-based algorithm indicated that a lateral beam was highly important (optimal) for rectal sparing in both 3D-CRT and IMRT. In Chapter 2, Potrebko *et al.* provided statistical and dosimetric data for a 10 prostate patient cohort following the RTOG P-0126 protocol to demonstrate that the optimal 5 equiangular-spaced coplanar IMRT beam arrangement for rectal sparing had a starting gantry angle of near 20° or 50° and thus included a lateral or near-lateral beam. This result was later shown to have strong correlation to minima in 5 beam intersection volume within the rectum in Chapter 3. Pugachev *et al.* [29] used a simulated annealing BOO algorithm to find the optimal set of 9 beam orientations for a prostate IMRT case. Lateral beams or near-lateral beams were included in the Pugachev *et al.* sets of 9 optimized coplanar beams and 9 optimized non-coplanar beams. Schreibmann *et al.* [36] investigated beam orientation class solutions in prostate IMRT. A genetic algorithm was used to optimize the beam orientations and a gradient-based method to optimize the intensity profiles of the beams. They concluded that the optimized 5 beam configurations in all 15 patient cases they examined had a similar beam setup, with nearly equiangular-spaced beams starting at the beam position of 20°- 45°. Notably, the Schreibmann *et al.* optimal 5 beam configurations contained a lateral or near-lateral beam. Stein *et al.* [3] employed a simulated annealing search technique to find the

optimal set of 3, 5, and 7 beam orientations for prostate IMRT. Each of the optimal beam configurations derived by Stein *et al.* included a lateral or near-lateral beam. The anatomy-based optimization results presented in this chapter are consistent with previous studies which indicate that a lateral or near-lateral beam plays an important role in the optimization of prostate IMRT.

The 5 optimal prostate beam orientations derived from the anatomy-based optimization produced similar rectal sparing in the high dose region but superior rectal sparing in the moderate dose region compared to all other examined plans. This may indicate that improvements in rectal sparing from optimization of beam orientations may be restricted to moderate dose regions. This finding is consistent with the previous studies by Stein *et al.* [3] and Pugachev *et al.* [29]. Although the complete couch angle space was available to the A-BOO algorithm in the prostate case, the highest ranked beam orientations for target conformity and rectal sparing were all coplanar beam orientations for both 3D-CRT and IMRT. This indicates that the 3D anatomic geometry of the rectum with respect to the PTV favors coplanar beam orientations. This is also the first work to use anatomy-based analysis (albeit on a single patient) to demonstrate the 4-field box beam orientations as 4 optimal beam orientations for 3D-CRT. The optimal 9 non-coplanar beam orientations derived by Pugachev *et al.* [29] had small couch angles ranging from -10° to +10°, and the addition of non-coplanar beam orientations to the search space resulted only in a marginal improvement of the final dose distribution for the rectum. The anatomy-based optimization results in this chapter are consistent with

Pugachev *et al.* since they also indicate that little benefit can be gained by using non-coplanar beam orientations in prostate IMRT.

In both oropharyngeal cases, the 5 optimized beam orientations produced improved parotid sparing without compromising any RTOG H-0022 protocol metrics for target coverage and sparing of other critical structures. The most substantial sparing of the contralateral parotid gland occurred using 5 optimized non-coplanar beam orientations instead of 5 optimized coplanar or near-coplanar beam orientations. These non-coplanar beam orientations are non-intuitive and would be difficult and time-consuming to manually determine in the BEV. Both coplanar and non-coplanar optimized beam orientations resulted in superior contralateral sparing compared to standard clinical beam arrangements of 5, 7, and 9 equiangular-spaced beams. In particular, the non-coplanar optimized beam orientations produced substantially better contralateral parotid sparing compared to plans using as many as 9 equiangular-spaced beams. This finding supports previous studies [45, 46] which have shown that increasing the number of equiangular-spaced beams will not necessarily result in significant improvements in parotid sparing. The results in this chapter and Chapter 4 demonstrate that substantial additional sparing of the parotid glands can be achieved by optimizing beam orientations and not necessarily by increasing the number of equiangular-spaced beams beyond 5. Figure 5.6 illustrates the improved sharpened dose gradient between the parotids and the targets due to the algorithms preference for placing beam edges between targets and OARs. In the stage-IV oropharyngeal case, 4 out of 5 non-coplanar optimal beam orientations were selected solely for parotid sparing. Nevertheless, the PTV66 and

PTV54 coverage satisfied protocol requirements in the 5-opt-non-copl plan. This may indicate a new methodology in IMRT treatment planning: the selection of optimal beam orientations does not have to be primarily based on target coverage but instead beams may be selected primarily for OAR sparing while allowing the large number of degrees of freedom through intensity modulation to ensure adequate target coverage. This chapter indicates that the use of equiangular-spaced beams and the dependence on intensity modulation to reduce dose to OARs does not produce optimal OAR sparing. Instead, this anatomy-based optimization approach can locate tangential beams bisecting the target and adjacent OARs and take advantage of the sharp beam penumbras in IMRT at the beam edge to improve OAR sparing over conventional IMRT plans.

The stage-III oropharyngeal case demonstrates the usefulness of this algorithm for optimizing beam orientations to produce a plan satisfying the RTOG H-0022 protocol when it is not possible to do so with standard beam arrangements. The H-0022 protocol specifies the mean dose to the contralateral parotid to be below 26 Gy since the mean dose is the best known predictor for the salivary function and severity of xerostomia in the parotid glands after radiotherapy [47, 48]. However, none of the standard 5, 7, and 9 equiangular-spaced beam arrangements in this case were able to satisfy this objective. With the use of 5 optimized non-coplanar beams, this objective was met, producing a mean dose in the contralateral parotid of 24.3 Gy.

For every clinical case examined in Chapter 4, all plans with 5 optimized beam orientations contained one or more beams that were the same or near beam orientations

produced by the A-BOO algorithm. For instance, the stage-IV oropharyngeal case contained a coplanar beam (gantry 37°) in the 5-opt-copl-5432BIV plan which was the parallel-opposed counterpart of a beam (gantry 215°) ranked by the A-BOO algorithm to have the highest coplanar score for contralateral parotid sparing. Likewise, the 5-opt-non-5432BIV plan for this case contained a non-coplanar beam (gantry 226°, couch 40°) which the A-BOO algorithm ranked to have the highest non-coplanar score for contralateral parotid sparing. In Table 4.5 of Chapter 4, reproduced below as Table 5.4, each of the ten sets of optimal beam orientations (gantry°, couch°) for the Stage-III oropharyngeal case contained one beam (marked in bold in Table 5.4) that was the same or near (within 20°) a beam orientation (or it's parallel-opposed counterpart) produced by the A-BOO algorithm for contralateral parotid sparing; identified in this chapter as a coplanar beam of (211°, 0°) or a non-coplanar beam of (213°, 333°).

Table 5.4: Ten sets of optimal beam orientations (gantry°, couch°), from Chapter 4, for the Stage-III oropharyngeal case obtained by performing BIV optimizations with ten different seeds of the random number generator. Beams that are the same or near (within 20°) a beam orientation (or it's parallel-opposed counterpart) identified by the A-BOO algorithm for contralateral parotid sparing are marked in bold.

Run	Optimal Beam Orientations (gantry°, couch°)
1	(15, 340),(112, 340),(211, 25),**(219, 315)**,(233, 20)
2	(17, 10),(144, 45),**(211, 330)**,(238, 40),(325, 330)
3	(3, 275),(45, 45),(132, 350),(149, 5),**(211, 345)**
4	(8, 310),**(25, 345)**,(149, 45),(227, 45),(231, 10)
5	(122, 15),**(211, 330)**,(233, 35),(234, 0),(325, 265)
6	(20, 5),(33, 30),**(37, 340)**,(164, 340),(226, 305)
7	(20, 340),(22, 65),(136, 330),**(214, 0)**,(228, 330)
8	(30, 15),(72, 30),(179, 350),**(211, 340)**,(308, 340)
9	(38, 50),(60, 0),(147, 25),**(211, 325)**,(234, 25)
10	(140, 5),**(212, 355)**,(234, 25),(328, 95),(341, 300)

The relationship between beam orientations that produce minima in BIV (from Chapter 4) and tangential beam orientations which bisect the target and adjacent critical structures (thereby allowing for a steep dose gradient between them) can be understood from geometrical principles. In Figure 5.8a, two beams ($B_1(\theta_1)$, $B_2(\theta_2)$) are illustrated to geometrically cover the target area from angles of incidence θ_1, and θ_2. These beam angles are not geometrically optimal since a non-zero 2 BIV exists in the adjacent OAR. However, if a beam angle ($\theta_2 = \theta_{edge}$) tangentially bisects the target and OAR, then the 2 BIV is a minimum (Figure 5.8b). Dosimetrically, the optimal beam angle (θ_{edge}) will facilitate the IMRT optimization in producing a steep dose gradient between the target

and OAR and, therefore, improve the sparing of this critical structure. This example can be generalized to N beams covering a target volume with adjacent critical structures in 3D.

Figure 5.8: The geometrical relationship between beam orientations that produce minima in BIV (from Chapter 4) and tangential beam orientations which bisect the target and adjacent critical structures. (a) Two beams ($B_1(\theta_1)$, $B_2(\theta_2)$) geometrically cover the target area from angles of incidence θ_1, and θ_2. These beam angles are not geometrically optimal since a non-zero 2 BIV exists in the adjacent OAR. (b) If a beam angle ($\theta_2 = \theta_{edge}$) tangentially bisects the target and OAR, then the 2 BIV is a minimum.

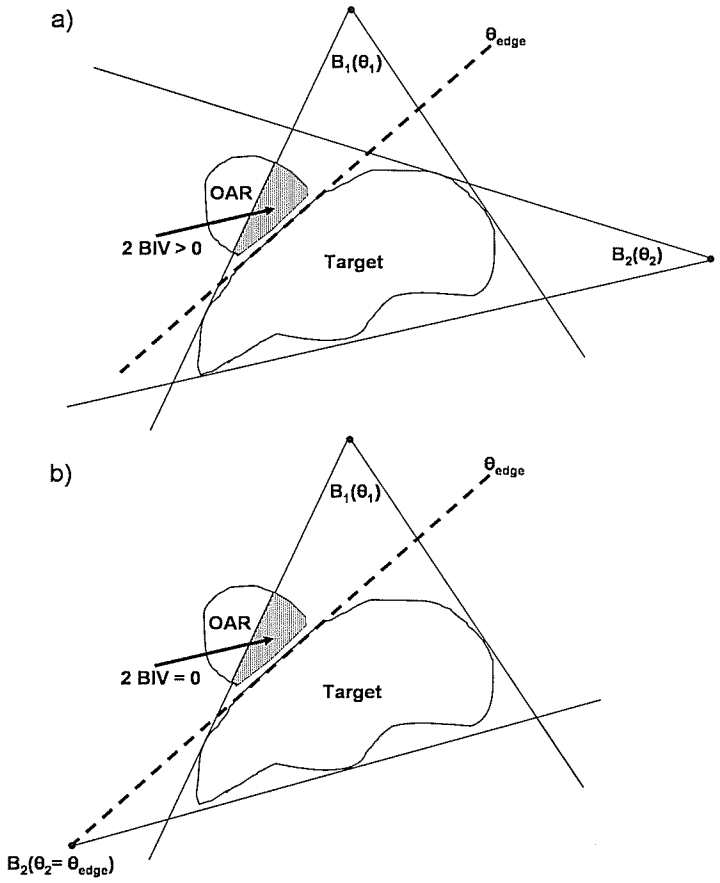

The A-BOO algorithm may be implemented in the clinic in a variety of ways. In this chapter, it was used as a tool for IMRT or 3D-CRT treatment planning to assist a treatment planner in selecting beam orientations that have the potential to improve sparing of critical structures in close proximity to the target. If integrated into a treatment planning system, the A-BOO algorithm could facilitate an intelligent choice of beam orientations in a similar manner as the BEV currently assists dosimetrists in evaluating beam orientations. The second use of this algorithm could be to provide a pre-ranking (or filter) of potentially optimal beam orientations to increase the computational efficiency of a dosimetric BOO algorithm. Pugachev *et al.* [32] computed a beam's-eye-view dosimetrics (BEVD) score to rank the quality of each possible beam orientation prior to a simulated annealing (SA) BOO algorithm. The sampling of gantry angles was then weighted according to the BEVD score during the BOO. A gantry angle with a higher BEVD score had a higher probability of being selected for beam intensity profile optimization. By taking into account the BEVD weighting in the SA sampling, the BOO avoided wasting computing time at sub-optimal beam orientations. Consequently, the BEVD-guided sampling improved both the optimization speed and convergence, however, average optimization times were still on the order of 2 hours. In a similar manner as Pugachev *et al.*, the geometric scores of beam orientations provided by the A-BOO algorithm could serve as an evaluation of the potential of beams to improve sparing of a number of different critical structures prior to dose-based BOO. Sampling of beam orientations in a stochastic framework could then be weighted by the A-BOO scores to improve optimization speed. All published dose-based BOO algorithms (that we are aware of) suffer from clinically infeasible computation times (0.5 to >200 hours) since

beam intensity profile optimization is typically performed on the entire space of possible beam orientations, a computationally inefficient method given the complexity of accurate dose calculations. The A-BOO algorithm could significantly reduce optimization time by performing an intelligent pre-ranking and, therefore, has the potential to make dosimetric BOO clinically feasible. This topic is the subject of future investigation for both 3D-CRT and IMRT. The current A-BOO algorithm is written using the Interactive Data Language (IDL, RSI, Boulder, CO). With the use of this high-level programming language for developmental purposes, typical computation times on a PC with a Pentium IV 2.0 GHz processor are 5-9 minutes but can be reduced by a factor of 100 or more by using a lower level programming language such as C.

5.5 Conclusions

The A-BOO algorithm presented in this chapter has been demonstrated to be robust for application to a variety of IMRT treatment sites. Beam orientations producing substantial improvements in critical structure sparing over conventional beam orientations can be produced in minutes compared to hours with existing dose-based methods. Furthermore, the algorithms identification of non-coplanar beams with optimized orientations brings additional substantial improvement in OAR sparing, especially for complicated head-and-neck treatment sites. Hence, for some complicated IMRT cases, the effectiveness of non-coplanar beam orientations should not be underestimated. In this chapter, the A-BOO algorithm was applied to four progressively complex patient cases to demonstrate the usefulness of the method. Given the clinically

infeasible computation times of many dosimetric BOO methods, the A-BOO algorithm is a clinically practical tool to facilitate the selection of beam orientations in IMRT.

5.6 Bibliography

1. Bortfeld, T. and W. Schlegel, *Optimization of beam orientations in radiation therapy: some theoretical considerations.* Phys Med Biol, 1993. **38**(2): p. 291-304.
2. Soderstrom, S. and A. Brahme, *Which is the most suitable number of photon beam portals in coplanar radiation therapy?* Int J Radiat Oncol Biol Phys, 1995. **33**(1): p. 151-9.
3. Stein, J., R. Mohan, et al., *Number and orientations of beams in intensity-modulated radiation treatments.* Med Phys, 1997. **24**(2): p. 149-60.
4. Liu, H.H., M. Jauregui, et al., *Beam angle optimization and reduction for intensity-modulated radiation therapy of non-small-cell lung cancers.* Int J Radiat Oncol Biol Phys, 2006. **65**(2): p. 561-72.
5. Wang, X., X. Zhang, et al., *Development of methods for beam angle optimization for IMRT using an accelerated exhaustive search strategy.* Int J Radiat Oncol Biol Phys, 2004. **60**(4): p. 1325-37.
6. Kim, S., H.C. Akpati, et al., *An immobilization system for claustrophobic patients in head-and-neck intensity-modulated radiation therapy.* Int J Radiat Oncol Biol Phys, 2004. **59**(5): p. 1531-9.

7. Ezzell, G.A., *Genetic and geometric optimization of three-dimensional radiation therapy treatment planning.* Med Phys, 1996. **23**(3): p. 293-305.

8. Haas, O.C., K.J. Burnham, et al., *Optimization of beam orientation in radiotherapy using planar geometry.* Phys Med Biol, 1998. **43**(8): p. 2179-93.

9. Meyer, J., S.M. Hummel, et al., *Automatic selection of non-coplanar beam directions for three-dimensional conformal radiotherapy.* Br J Radiol, 2005. **78**(928): p. 316-27.

10. Rowbottom, C.G., V.S. Khoo, et al., *Simultaneous optimization of beam orientations and beam weights in conformal radiotherapy.* Med Phys, 2001. **28**(8): p. 1696-702.

11. Rowbottom, C.G., M. Oldham, et al., *Constrained customization of non-coplanar beam orientations in radiotherapy of brain tumours.* Phys Med Biol, 1999. **44**(2): p. 383-99.

12. Rowbottom, C.G., S. Webb, et al., *Improvements in prostate radiotherapy from the customization of beam directions.* Med Phys, 1998. **25**(7 Pt 1): p. 1171-9.

13. Schreibmann, E., M. Lahanas, et al., *A geometry based optimization algorithm for conformal external beam radiotherapy.* Phys Med Biol, 2003. **48**(12): p. 1825-41.

14. Wang, C., J. Dai, et al., *Optimization of beam orientations and beam weights for conformal radiotherapy using mixed integer programming.* Phys Med Biol, 2003. **48**(24): p. 4065-76.

15. Wu, X. and Y. Zhu, *A mixed-encoding genetic algorithm with beam constraint for conformal radiotherapy treatment planning.* Med Phys, 2000. **27**(11): p. 2508-16.

16. Bedford, J.L. and S. Webb, *Elimination of importance factors for clinically accurate selection of beam orientations, beam weights and wedge angles in conformal radiation therapy.* Med Phys, 2003. **30**(7): p. 1788-804.

17. Gokhale, P., E.M. Hussein, et al., *Determination of beam orientation in radiotherapy planning.* Med Phys, 1994. **21**(3): p. 393-400.

18. Rowbottom, C.G., S. Webb, et al., *Beam-orientation customization using an artificial neural network.* Phys Med Biol, 1999. **44**(9): p. 2251-62.

19. Woudstra, E. and B.J. Heijmen, *Automated beam angle and weight selection in radiotherapy treatment planning applied to pancreas tumors.* Int J Radiat Oncol Biol Phys, 2003. **56**(3): p. 878-88.

20. Beaulieu, F., L. Beaulieu, et al., *Simultaneous optimization of beam orientations, wedge filters and field weights for inverse planning with anatomy-based MLC fields.* Med Phys, 2004. **31**(6): p. 1546-57.

21. Djajaputra, D., Q. Wu, et al., *Algorithm and performance of a clinical IMRT beam-angle optimization system.* Phys Med Biol, 2003. **48**(19): p. 3191-212.

22. D'Souza, W.D., R.R. Meyer, et al., *Selection of beam orientations in intensity-modulated radiation therapy using single-beam indices and integer programming.* Phys Med Biol, 2004. **49**(15): p. 3465-81.

23. Gaede, S. and E. Wong, *An algorithm for systematic selection of beam directions for IMRT.* Med Phys, 2004. **31**(2): p. 376-88.

24. Hou, Q., J. Wang, et al., *Beam orientation optimization for IMRT by a hybrid method of the genetic algorithm and the simulated dynamics.* Med Phys, 2003. **30**(9): p. 2360-7.

25. Lee, E.K., T. Fox, et al., *Simultaneous beam geometry and intensity map optimization in intensity-modulated radiation therapy.* Int J Radiat Oncol Biol Phys, 2006. **64**(1): p. 301-20.

26. Li, Y., D. Yao, et al., *A particle swarm optimization algorithm for beam angle selection in intensity-modulated radiotherapy planning.* Phys Med Biol, 2005. **50**(15): p. 3491-514.

27. Li, Y., J. Yao, et al., *Automatic beam angle selection in IMRT planning using genetic algorithm.* Phys Med Biol, 2004. **49**(10): p. 1915-32.

28. Meedt, G., M. Alber, et al., *Non-coplanar beam direction optimization for intensity-modulated radiotherapy.* Phys Med Biol, 2003. **48**(18): p. 2999-3019.

29. Pugachev, A., J.G. Li, et al., *Role of beam orientation optimization in intensity-modulated radiation therapy.* Int J Radiat Oncol Biol Phys, 2001. **50**(2): p. 551-60.

30. Pugachev, A. and L. Xing, *Pseudo beam's-eye-view as applied to beam orientation selection in intensity-modulated radiation therapy.* Int J Radiat Oncol Biol Phys, 2001. **51**(5): p. 1361-70.

31. Pugachev, A. and L. Xing, *Computer-assisted selection of coplanar beam orientations in intensity-modulated radiation therapy.* Phys Med Biol, 2001. **46**(9): p. 2467-76.

32. Pugachev, A. and L. Xing, *Incorporating prior knowledge into beam orientation optimization in IMRT.* Int J Radiat Oncol Biol Phys, 2002. **54**(5): p. 1565-74.

33. Pugachev, A.B., A.L. Boyer, et al., *Beam orientation optimization in intensity-modulated radiation treatment planning.* Med Phys, 2000. **27**(6): p. 1238-45.

34. Rowbottom, C.G., C.M. Nutting, et al., *Beam-orientation optimization of intensity-modulated radiotherapy: clinical application to parotid gland tumours.* Radiother Oncol, 2001. **59**(2): p. 169-77.

35. Schreibmann, E., M. Lahanas, et al., *Multiobjective evolutionary optimization of the number of beams, their orientations and weights for intensity-modulated radiation therapy.* Phys Med Biol, 2004. **49**(5): p. 747-70.

36. Schreibmann, E. and L. Xing, *Feasibility study of beam orientation class-solutions for prostate IMRT.* Med Phys, 2004. **31**(10): p. 2863-70.

37. Schreibmann, E. and L. Xing, *Dose-volume based ranking of incident beam direction and its utility in facilitating IMRT beam placement.* Int J Radiat Oncol Biol Phys, 2005. **63**(2): p. 584-93.

38. Wang, X., X. Zhang, et al., *Effectiveness of noncoplanar IMRT planning using a parallelized multiresolution beam angle optimization method for paranasal sinus carcinoma.* Int J Radiat Oncol Biol Phys, 2005. **63**(2): p. 594-601.

39. Yang, R., J. Dai, et al., *Beam orientation optimization for intensity-modulated radiation therapy using mixed integer programming.* Phys Med Biol, 2006. **51**(15): p. 3653-66.

40. Das, S., T. Cullip, et al., *Beam orientation selection for intensity-modulated radiation therapy based on target equivalent uniform dose maximization.* Int J Radiat Oncol Biol Phys, 2003. **55**(1): p. 215-24.

41. Woudstra, E., B.J. Heijmen, et al., *Automated selection of beam orientations and segmented intensity-modulated radiotherapy (IMRT) for treatment of oesophagus tumors.* Radiother Oncol, 2005. **77**(3): p. 254-61.

42. Zelefsky, M.J., Z. Fuks, et al., *High-dose intensity modulated radiation therapy for prostate cancer: early toxicity and biochemical outcome in 772 patients.* Int J Radiat Oncol Biol Phys, 2002. **53**(5): p. 1111-6.

43. Shepard, D.M., M.A. Earl, et al., *Direct aperture optimization: a turnkey solution for step-and-shoot IMRT.* Med Phys, 2002. **29**(6): p. 1007-18.

44. Siebers, J.V., M. Lauterbach, et al., *Incorporating multi-leaf collimator leaf sequencing into iterative IMRT optimization.* Med Phys, 2002. **29**(6): p. 952-9.

45. van Asselen, B., H. Dehnad, et al., *Segmental IMRT for oropharyngeal cancer in a clinical setting.* Radiother Oncol, 2003. **69**(3): p. 259-66.

46. Zhu, X.R., C.J. Schultz, et al., *Planning quality and delivery efficiency of sMLC delivered IMRT treatment of oropharyngeal cancers evaluated by RTOG H-0022 dosimetric criteria.* J Appl Clin Med Phys, 2004. **5**(4): p. 80-95.

47. Chao, K.S., J.O. Deasy, et al., *A prospective study of salivary function sparing in patients with head-and-neck cancers receiving intensity-modulated or three-dimensional radiation therapy: initial results.* Int J Radiat Oncol Biol Phys, 2001. **49**(4): p. 907-16.

48. Eisbruch, A., H.M. Kim, et al., *Xerostomia and its predictors following parotid-sparing irradiation of head-and-neck cancer.* Int J Radiat Oncol Biol Phys, 2001. **50**(3): p. 695-704.

CHAPTER SIX: SUMMARY

6.1 Conclusions

For tens of thousands of Canadians diagnosed with cancer every year, the use of radiation therapy will be a crucial component of their treatment. The recent advent of intensity-modulated radiation therapy (IMRT) has improved the conformity of the dose distribution to the tumour and improved the sparing of critical structures to an extent that was not possible with previous techniques. Increased probability for local control of the tumour and reduced radiation complications are exciting clinical implications of IMRT.

Sophisticated as it is, IMRT is not yet optimized to produce the best possible dose distribution within the patient. Beam orientations selected manually (by the treatment planner) or equiangular-spaced beams may be far from optimal. As discussed in Chapter 1, the literature has attempted to address the fundamental problem of optimizing beam orientations for IMRT. However, the proposed methods cannot be routinely used in a clinical setting due to long computation times when implemented on clinical cases [1-5]. The inherent disadvantage of these methods is that they involve a time-consuming computation of complex dose distributions and fluence maps for each trial set of beam orientations.

Geometry is a fundamental element in the optimization of radiation therapy treatments. The goal of treatment planning is to maximize the irradiation of the target and minimize irradiation of normal tissue. The first step in this optimization process is to

position the treatment beams. The dosimetric quality of a treatment plan is ultimately determined by the geometry (3D shape, size, and position) of the patient's anatomy. Due to computational simplicity, geometry-based beam orientation optimization (BOO) algorithms have strong potential to perform BOO for IMRT in a clinically reasonable timeframe, unlike current more complicated dose-based BOO methods. However, as discussed in Chapter 1, only a few geometry-based BOO methods for 3D-CRT have been published and no geometry-based BOO method has been applied to select beam orientations in IMRT. The ability of IMRT to produce complex fluence distributions for each beam may have distracted researchers away from simple, fast geometric BOO methods for use in IMRT. Therefore, the objective of this thesis was to demonstrate several fast, geometry-based (instead of dose-based) BOO methods which can produce improved IMRT dose distributions compared to conventional IMRT plans in a clinically realistic time frame. This objective was achieved by performing four distinct investigations (Chapters 2 through 5) resulting in the development of two different geometry-based BOO algorithms.

Chapter 2 investigated the effect of beam orientation on the dose distribution in a treatment plan by performing an exhaustive treatment planning study of a commonly used solution space, coplanar equiangular beams, on a cohort of prostate IMRT patients. This study, published in *Radiotherapy and Oncology*, was the first study of its kind to investigate the variation of critical structure dose metrics in a treatment plan, while holding target coverage constant, as a function of the systematic and exhaustive selection of beam orientations through this entire solution space. Statistically significant variations

(which demonstrated a characteristic 'W' pattern), with dosimetric importance, were observed in the rectal high dose metrics as a function of beam orientation using five equiangular-spaced beams. Optimal sets of five equiangular-spaced beams, corresponding to local minima in the 'W' pattern of the rectal high dose metrics, were proven to exist. The similarity in the location of minima in the rectal high dose metrics for the patient cohort also indicated an optimal beam orientation class solution in prostate IMRT. It was demonstrated that five optimal, equiangular-spaced beams could produce nearly equivalent rectal sparing and maintain target coverage as seven equiangular-spaced beams. Since only small variations of the dose metrics were observed using seven beams, this implied that the effect of beam orientation was less important when a larger (>5) number of beams were used. However, it should be noted that this result is strictly valid for coplanar, equiangular-beam space in prostate IMRT and may not be generalized to other treatment sites without performing analogous studies.

To achieve improved rectal sparing in prostate IMRT using 5 equiangular-spaced beams, the optimal beam orientation class solution presented in Chapter 2 ultimately has the distinct advantage of being simple for clinics to implement. However, as with any class solution approach, the solution is not customized for any particular patient. It was observed that patient geometric variability produced a $\pm 5°$ variation in the location of the minima in the rectal high dose metrics. Therefore, the use of a class solution may not produce the full dosimetric advantage in rectal sparing for all patients. To customize optimal equiangular-spaced beam orientations for a particular patient, a BOO algorithm was required.

Chapter 3 presented a fast, geometry-based BOO algorithm, published in *Medical Physics*, which reproduced the optimal sets of 5 equiangular-spaced beams observed in Chapter 2 and explained the origin of the characteristic 'W' pattern in the rectal high dose metrics for each prostate patient. Based on a theoretical derivation, the algorithm exploited a strong correlation between the beam intersection volume (BIV) and the subsequent IMRT dose distribution. By computing the 5 BIV within the rectum, the algorithm reproduced the class solution 'W' pattern in the rectal high dose metrics and predicted the location of the two observed dosimetric minima to within 5° (the angular step size used). The algorithm also demonstrated that a dose-volume histogram (DVH) is the superposition of volume-weighted BIV components (by calculating BIV components in the rectum within several isodose volumes). This was the first work to correlate dose-volume metrics to geometry for IMRT and introduced several exciting questions: Can the optimization of a critical structure's DVH be achieved through optimization of multiple BIV components within that structure? Can the BIV optimization concept be useful for other IMRT treatment sites (besides prostate)? The answers to these questions required the development of a BOO algorithm that simultaneously optimized multiple BIV components in a critical structure for a variety of IMRT treatment sites.

Chapter 4 introduced a stochastic BOO algorithm, submitted to *Medical Physics*, which generalized the BIV concept to include the optimization of multiple BIV components within a critical structure using coplanar or non-coplanar beam orientations. In the clinical cases presented, the simulated annealing (SA) algorithm was used to simultaneously optimize several BIV components in the most important critical structure

(right kidney, rectum, and contralateral parotid gland) for a particular treatment site (gastric, prostate, and Stage-III and IV oropharynx). The BIV-optimized plans produced substantially improved critical structure sparing compared to conventional IMRT plans employing 5, 7, and 9 equiangular-spaced beams. Both the optimal coplanar and non-coplanar beam orientations would have been extremely difficult and time-consuming to manually determine. This novel work was the first geometry-based BOO algorithm applied to IMRT. The SA framework of the algorithm was useful to demonstrate the proof-of-concept of optimizing multiple BIV components within a critical structure for a variety of IMRT treatment sites. However, the ability to simultaneously optimize multiple BIV components within several critical structures, and not become trapped in local minima in the search space, requires a true multi-objective stochastic optimization technique. Unfortunately, all stochastic optimization methods have an inherent disadvantage of long execution times. The desire to reduce the time required for the selection of optimal beam orientations resulted in the investigation of whether any beams contribute more prominently to the optimization of BIV. It was observed that, even if different seeds of the random number generator were used in the SA optimization, similar dominant beam orientations would always manifest themselves in the optimal solution. Under further geometric analysis, it was discovered that these dominant beams result in the optimal geometric sparing of a critical structure and thus correspond to a minimum in BIV within that structure. Therefore, a subsequent BOO algorithm was required to exploit this information and, by doing so, select optimal beam orientations in a significantly faster time than the SA algorithm.

Chapter 5 introduced a fast, geometry-based BOO algorithm for IMRT, accepted in *Medical Physics*, which vectorially analyzed patient anatomy and produced optimal coplanar and non-coplanar beam orientations based on (1) tangential orientation bisecting the target and adjacent critical structures to produce precipitous dose gradients between them and (2) geometric target conformity. In this work, the anatomic beam orientation optimization (A-BOO) algorithm was used as a treatment planning tool to automatically evaluate the complete space of beam orientations and systematically provide optimal beams. The algorithm provided the treatment planner with a list of ranked scores and beam orientations to facilitate sparing of a user-selected critical structure. A similar list was also produced based on target conformity. Five top ranked beam orientations were chosen by the treatment planner from these lists and used to generate optimal IMRT plans for all the clinical cases presented in Chapter 4 (gastric, prostate, and Stage-III and IV oropharynx). Despite the A-BOO algorithm representing a different geometry-based approach to BOO than the BIV algorithm in Chapter 4, each optimal A-BOO plan contained one or more beams that were the same or near beam orientations produced by the BIV algorithm. This was because tangential beam orientations which bisected the target and adjacent critical structures also produced minima in BIV. As a result, both the A-BOO and BIV algorithms produced similar improvements in critical structure sparing compared to conventional IMRT plans employing 5, 7, and 9 equiangular-spaced beams for each clinical case. However, the A-BOO algorithm reduced the time required to produce optimal solutions by an order of magnitude compared to the BIV algorithm since a stochastic optimizer was not involved.

In conclusion, this thesis has developed and demonstrated the usefulness of two different geometry-based BOO algorithms for IMRT (Chapters 3 through 5). The development of these algorithms was motivated by a treatment planning study, presented in Chapter 2, demonstrating that beam orientation does indeed play an important role in the quality of an IMRT treatment plan. Each algorithm represents a novel and distinct contribution to the literature, representing the first geometry-based BOO algorithms to be applied for IMRT. The algorithms were implemented on clinical IMRT cases to demonstrate their potential use in the clinic. The current execution times of the algorithms presented in Chapters 3 and 5 are faster than any published dosimetric BOO algorithms. It is expected that when ported to a computer language which provides better optimization support, the execution time of each algorithm (including the SA algorithm in Chapter 4) will be significantly better than that of any existing BOO technique (less than 5 minutes on a PC with a Pentium IV 2.0 GHz processor). In addition to faster computation times, a geometry-based BOO method has the advantage over dosimetric methods of simplicity. Given the clinically infeasible computation times of many dosimetric BOO algorithms, the geometry-based algorithms presented in this thesis have a strong potential to be implemented into a commercial treatment planning system and thus facilitate beam angle selection for IMRT in clinical practice.

6.2 Future Research

The geometry-based BOO algorithms presented in this thesis have demonstrated that the computation of dose for the optimization of beam orientations in IMRT is not

necessary. However, a minor modification of both BIV algorithms may be made to improve the accuracy by including a primary dose calculation and thus predict the absolute variation of the dose distribution with beam orientation rather than the relative variation. This can be easily achieved by weighting the voxels in the BIV component calculation by an exponential attenuation factor (representing primary dose) which incorporates a fast calculation of the radiological depth [6, 7]. Further work is required to determine whether including a dose calculation in the BOO algorithms will produce a significant improvement in the results over pure geometry-based BOO algorithms.

The BIV optimization approach, presented in Chapter 4, may be modified by several improvements to enhance the overall applicability and clinical usefulness. Since the objective of any IMRT plan is to deliver the prescribed dose(s) to the target(s) while sparing multiple critical structures, a mechanism is required to select optimal beam orientations which minimize BIV in all the anatomic structures. The ultimate goal is to develop a BOO algorithm with the ability to simultaneously optimize multiple BIV components within several critical structures as well as optimize the geometric conformity index of the target(s). The algorithm must also have the ability to escape local minima in the search space. Therefore, a true multi-objective, stochastic optimization technique is required. An ideal candidate for such an optimization method is the genetic algorithm (GA), which has been incorporated into several BOO algorithms presented in the literature [8-13]. The GA is a global optimization technique that simulates the natural process of evolution in which the 'fittest' (optimal) solutions survive after numerous generations of genetic operations such as selection, crossover, and mutation [14]. An

advantage of the GA over other random search algorithms, such as simulated annealing, is that it is possible to search simultaneously for alternative solutions in different regions of the solution space. Therefore, the GA can perform multi-objective optimizations with the capability of locating the 'Pareto optimal' solutions where further improvement in the objective function associated with any one of the objectives considered cannot be achieved. The determination of 'Pareto optimal' solutions will allow for an analysis of the trade-offs between multiple BIV components within several critical structures and thus enable the clinician to choose between alternative solutions depending on the desired outcome (i.e. preferentially spare one or more particular critical structures over others).

Although all the optimized plans for the oropharyngeal cases presented in Chapters 4 and 5 satisfied the target coverage and critical structure metrics of the protocol, some dosimetric advantages in target coverage were observed with the use of more than five beams. Zhu *et al.* [15] also illustrated the known improvement of dose homogeneity in the target volume for complicated head-and-neck treatment sites when using a larger number of beams. To exploit any possible improvement in target coverage, it could be valuable to perform BIV optimizations within critical structures using more than five beams (i.e. seven). However, as demonstrated by Bortfeld and Schlegel [16], a point of diminishing returns will be reached as the number of beams is increased since the dose distribution becomes less dependent on beam orientation. Therefore, a future investigation could determine whether the optimization of BIV can be useful to improve critical structure sparing when employing a larger number of beams, or alternatively determine the optimal number of beams to use.

The BIV optimization concept also has potential to be utilized for the selection of optimal beams in other IMRT modalities such as intensity-modulated arc therapy (IMAT) [17-24]. Instead of delivering treatments at fixed beam angles, IMAT delivers optimized dose distributions by rotating the radiation beam around the patient while continuously changing the field shape (formed by the multileaf collimator). Intensity modulation at all angles around the patient is achieved through multiple overlapping gantry arcs (typically, three to five gantry arcs). The goal of the primary arc is to generate a uniform and high dose region in the target volume while additional arcs serve to shield different critical structures via intensity modulation. More recently, IMAT delivery in a single 360° gantry arc has been proposed [25, 26]. Preliminary results demonstrate that single arc IMAT can produce dose distributions that are equivalent or superior to fixed gantry IMRT with superior delivery efficiency. Based on the research in this thesis, it is hypothesized that the optimization of single or multiple arc IMAT may be achieved through the selection of optimal coplanar or non-coplanar 'avoidance arcs' which minimize BIV in critical structures, limiting the exposure of these structures within the beam, and thus improve the ability of the IMRT optimization to find better solutions. Furthermore, when couch motion is simultaneously enabled, optimal coplanar arcs could be converted into optimal, non-coplanar trajectories. It is anticipated that the improvement of IMAT through the optimization of geometric parameters will be an exciting research opportunity.

6.3 Bibliography

1. Djajaputra, D., Q. Wu, et al., *Algorithm and performance of a clinical IMRT beam-angle optimization system.* Phys Med Biol, 2003. **48**(19): p. 3191-212.
2. Liu, H.H., M. Jauregui, et al., *Beam angle optimization and reduction for intensity-modulated radiation therapy of non-small-cell lung cancers.* Int J Radiat Oncol Biol Phys, 2006. **65**(2): p. 561-72.
3. Pugachev, A., J.G. Li, et al., *Role of beam orientation optimization in intensity-modulated radiation therapy.* Int J Radiat Oncol Biol Phys, 2001. **50**(2): p. 551-60.
4. Pugachev, A. and L. Xing, *Pseudo beam's-eye-view as applied to beam orientation selection in intensity-modulated radiation therapy.* Int J Radiat Oncol Biol Phys, 2001. **51**(5): p. 1361-70.
5. Rowbottom, C.G., C.M. Nutting, et al., *Beam-orientation optimization of intensity-modulated radiotherapy: clinical application to parotid gland tumours.* Radiother Oncol, 2001. **59**(2): p. 169-77.
6. Siddon, R.L., *Calculation of the radiological depth.* Med Phys, 1985. **12**(1): p. 84-7.
7. Siddon, R.L., *Fast calculation of the exact radiological path for a three-dimensional CT array.* Med Phys, 1985. **12**(2): p. 252-5.
8. Ezzell, G.A., *Genetic and geometric optimization of three-dimensional radiation therapy treatment planning.* Med Phys, 1996. **23**(3): p. 293-305.

9. Hou, Q., J. Wang, et al., *Beam orientation optimization for IMRT by a hybrid method of the genetic algorithm and the simulated dynamics.* Med Phys, 2003. **30**(9): p. 2360-7.

10. Li, Y., J. Yao, et al., *Automatic beam angle selection in IMRT planning using genetic algorithm.* Phys Med Biol, 2004. **49**(10): p. 1915-32.

11. Schreibmann, E., M. Lahanas, et al., *Multiobjective evolutionary optimization of the number of beams, their orientations and weights for intensity-modulated radiation therapy.* Phys Med Biol, 2004. **49**(5): p. 747-70.

12. Schreibmann, E. and L. Xing, *Feasibility study of beam orientation class-solutions for prostate IMRT.* Med Phys, 2004. **31**(10): p. 2863-70.

13. Wu, X. and Y. Zhu, *A mixed-encoding genetic algorithm with beam constraint for conformal radiotherapy treatment planning.* Med Phys, 2000. **27**(11): p. 2508-16.

14. Goldberg, D.E., *Genetic Algorithms in Search, Optimization, and Machine Learning.* Addison-Wesley, Toronto, 1989.

15. Zhu, X.R., C.J. Schultz, et al., *Planning quality and delivery efficiency of sMLC delivered IMRT treatment of oropharyngeal cancers evaluated by RTOG H-0022 dosimetric criteria.* J Appl Clin Med Phys, 2004. **5**(4): p. 80-95.

16. Bortfeld, T. and W. Schlegel, *Optimization of beam orientations in radiation therapy: some theoretical considerations.* Phys Med Biol, 1993. **38**(2): p. 291-304.

17. Cameron, C., *Sweeping-window arc therapy: an implementation of rotational IMRT with automatic beam-weight calculation.* Phys Med Biol, 2005. **50**(18): p. 4317-36.

18. Earl, M.A., D.M. Shepard, et al., *Inverse planning for intensity-modulated arc therapy using direct aperture optimization.* Phys Med Biol, 2003. **48**(8): p. 1075-89.

19. Gladwish, A., M. Oliver, et al., *Segmentation and leaf sequencing for intensity modulated arc therapy.* Med Phys, 2007. **34**(5): p. 1779-88.

20. Krayenbuehl, J., J.B. Davis, et al., *Dynamic intensity-modulated non-coplanar arc radiotherapy (INCA) for head and neck cancer.* Radiother Oncol, 2006. **81**(2): p. 151-7.

21. Shepard, D.M., D. Cao, et al., *An arc-sequencing algorithm for intensity modulated arc therapy.* Med Phys, 2007. **34**(2): p. 464-70.

22. Wong, E., J.Z. Chen, et al., *Intensity-modulated arc therapy simplified.* Int J Radiat Oncol Biol Phys, 2002. **53**(1): p. 222-35.

23. Yu, C.X., X.A. Li, et al., *Clinical implementation of intensity-modulated arc therapy.* Int J Radiat Oncol Biol Phys, 2002. **53**(2): p. 453-63.

24. Yu, C.X., *Intensity-modulated arc therapy with dynamic multileaf collimation: an alternative to tomotherapy.* Phys Med Biol, 1995. **40**(9): p. 1435-49.

25. Ulrich, S., S. Nill, et al., *Development of an optimization concept for arc-modulated cone beam therapy.* Phys Med Biol, 2007. **52**(14): p. 4099-119.

26. Crooks, S.M., X. Wu, et al., *Aperture modulated arc therapy.* Phys Med Biol, 2003. **48**(10): p. 1333-44.